

2020

## Searches for Fast Radio Bursts using Machine Learning

Devansh Agarwal

West Virginia University, da0017@mix.wvu.edu

Follow this and additional works at: <https://researchrepository.wvu.edu/etd>



Part of the [Artificial Intelligence and Robotics Commons](#), and the [Other Astrophysics and Astronomy Commons](#)

---

### Recommended Citation

Agarwal, Devansh, "Searches for Fast Radio Bursts using Machine Learning" (2020). *Graduate Theses, Dissertations, and Problem Reports*. 7827.

<https://researchrepository.wvu.edu/etd/7827>


This Dissertation is protected by copyright and/or related rights. It has been brought to you by the The Research Repository @ WVU with permission from the rights-holder(s). You are free to use this Dissertation in any way that is permitted by the copyright and related rights legislation that applies to your use. For other uses you must obtain permission from the rights-holder(s) directly, unless additional rights are indicated by a Creative Commons license in the record and/ or on the work itself. This Dissertation has been accepted for inclusion in WVU Graduate Theses, Dissertations, and Problem Reports collection by an authorized administrator of The Research Repository @ WVU. For more information, please contact [researchrepository@mail.wvu.edu](mailto:researchrepository@mail.wvu.edu).

2020

## Searches for Fast Radio Bursts using Machine Learning

Devansh Agarwal

Follow this and additional works at: <https://researchrepository.wvu.edu/etd>

 Part of the [Artificial Intelligence and Robotics Commons](#), and the [Other Astrophysics and Astronomy Commons](#)

---

# Searches for Fast Radio Bursts using Machine Learning

Devansh Agarwal

Dissertation submitted  
to the Eberly College of Arts and Sciences  
at West Virginia University

in partial fulfillment of the requirements for the degree of

Doctor of Philosophy  
in  
Physics

Duncan Lorimer, Ph.D., Chair  
Maura McLaughlin, Ph.D.  
Sarah Burke-Spolaor, Ph.D.  
Keith Bannister, Ph.D.

Department of Physics and Astronomy

Morgantown, West Virginia, USA  
2020

Keywords: Radio Transients, FRBs, Machine Learning  
Copyright 2020 Devansh Agarwal

Abstract

## Searches for Fast Radio Bursts using Machine Learning

Devansh Agarwal

Fast Radio bursts (FRBs) are enigmatic astrophysical events with millisecond durations and flux densities in the range 0.1–100 Jy, with the prototype source discovered by Lorimer et al. (2007). Like pulsars, FRBs show the characteristic inverse square sweep in observing frequency due to propagation through an ionized medium. This effect is quantified by the dispersion measure (DM). Unlike pulsars, FRBs have anomalously high DMs, which are consistent with an extragalactic origin. Over 100 FRBs have been published at the time of writing, and 13 have been conclusively identified with host galaxies with spectroscopically determined redshifts in the range  $0.003 \lesssim z \lesssim 0.66$ .

Detection of FRBs requires data at radio frequencies to be de-dispersed at many trial DM values. Incoming radio telescope data are appropriately combined for each DM to form a time series that is then searched using matched filters to find events above a certain signal-to-noise threshold. In the past, diagnostic plots showing these events are most commonly inspected by humans to determine if they are of astrophysical origin. With ongoing FRB surveys producing millions of candidates, machine learning algorithms for candidate classification are now necessary. In this thesis, we present state-of-the-art deep neural networks to classify FRB candidates and events produced by radio frequency interference (RFI). We present 11 deep learning models named FETCH, each with accuracy and recall above 99.5% as determined using a dataset comprising real RFI and pulsar candidates. These algorithms are telescope and frequency agnostic and can correctly classify all FRBs with signal-to-noise ratios above 10 in datasets collected with the Parkes telescope and the Australian Square Kilometre Array Pathfinder (ASKAP).

We present the design, deployment, and initial results from the real-time commensal FRB search pipeline at the Robert C. Byrd Green Bank Telescope (GBT) named GREENBURST. The pipeline uses FETCH to winnow down the



vast number of false-positive single-pulse candidates that mostly result from RFI. In our observations totaling 276 days so far, we have detected individual pulses from 20 known radio pulsars, which provide excellent verification of the system performance. Although no FRBs have been detected to date, we have used our results to update the analysis of Lawrence et al. (2017) to constrain the FRB all-sky rate to be  $1140_{-180}^{+200}$  per day above a peak flux density of 1 Jy. We also constrain the source count index  $\alpha = 0.84 \pm 0.06$ , substantially flatter than expected from a Euclidean distribution of standard candles (where  $\alpha = 1.5$ ). We make predictions for detection rates with GREENBURST as well as other ongoing and planned FRB experiments.

Lastly, we present the discovery of FRB 180417 through a targeted search for faint FRBs near the core of the Virgo cluster using ASKAP. Several radio telescopes promptly followed up the FRB for a total of 27 h, but no repeat bursts were detected. An optical follow-up of FRB 180417 using the PROMPT5 telescope revealed no new sources down to an  $R$ -band magnitude of 20.1. We argue that FRB 180417 is likely behind the Virgo cluster as the Galactic and intracluster DM contributions are small compared to the DM of the FRB, and there are no galaxies in the line of sight. Adopting an FRB rate of  $10^3$  FRBs  $\text{sky}^{-1} \text{day}^{-1}$  with flux above 1 Jy out to  $z = 1$ , our non-detection of FRBs from Virgo constrains (at 68% confidence limit) the faint-end slope of the luminosity function  $\alpha < 1.6$ , and the minimum luminosity,  $L_{\min} \gtrsim 6.5 \times 10^{39} \text{ erg s}^{-1}$ .

To my beloved Megha

## Acknowledgments

No one achieves anything alone; this work results from support from many people I would like to thank. I am indebted to my supervisor, Duncan Lorimer, for his patience and guidance throughout my grad school. I want to thank my committee members, Maura McLaughlin and Sarah Burke-Spolaor, for guiding me on various stages in the last four years.

I want to pay my special regards to Keith Bannister for serving as the external committee member, putting up with odd hours for my oral and Ph.D. exams. I learned about FRB surveys by discussions with Keith while working on the Virgo project, which resulted in one of the chapters of this thesis.

I wish to thank Aris Karastergiou and Ben Stappers. They gave me the opportunity to visit the University of Oxford and the University of Manchester, respectively. I also wish to thank Pavlos Protopapas for inviting me to Harvard University and work with him on several machine learning problems. All the valuable discussions and the projects I worked on with them will benefit me throughout my career.

I would like to recognize the invaluable assistance that Nate provided throughout my grad school. My love for GPU-accelerated computing, big data, and machine learning were all enabled by Nate's constant support. The department office staff, especially Viola Bryant, are appreciated for their assistance with paperwork.

I am very grateful to my fellow graduate students and office mates, Brent, Amber, Belinda, Joseph, and Nihan, for their great company, useful conversations on research projects. I wish to express my deepest gratitude to Kshitij for the food, research projects, conference trips, and countless other things. I want to extend my thanks to Harsha, Nipuni, Sarang, and Deepak, who always helped raise my spirits.

I want to thank Nandivada Rathnashree of Nehru Planetarium for introducing me to the field of pulsars and Yashwant Gupta of NCRA for providing me the opportunity to work in radio astronomy. I would like to pay my special regards to Archana and Shanki of IIT-B for their support and encouragement during and after my undergrad.

Finally, I am indebted to Megha Rajoria for being a source of inspiration. Without her love, care, and support, I wouldn't be where I am today, and I dedicate this thesis to her. I want to thank my uncle Sushant and my aunt Rashmi for making me feel at home in a new country and for all the festival celebrations. I also would like to thank my parents, who always nourished my love for science since childhood.

# Table of Contents

List of Tables	ix
List of Figures	x
1 Introduction	1
1.1 Fast Radio Transients . . . . .	1
1.2 Interstellar Medium . . . . .	3
1.2.1 Dispersion . . . . .	3
1.2.2 Scattering . . . . .	6
1.3 Fast Radio Bursts . . . . .	8
1.3.1 Repeating FRBs . . . . .	8
1.3.1.1 Periodic Repeaters . . . . .	10
1.3.2 Observables . . . . .	11
1.3.2.1 Dispersion and Scattering . . . . .	13
1.3.2.2 Dynamic Spectrum . . . . .	13
1.3.2.3 Polarization . . . . .	16
1.3.2.4 Localization . . . . .	17
1.3.2.5 The Macquart Relation . . . . .	18
1.3.2.6 All-Sky FRB Rates . . . . .	20
1.4 Detection of FRBs . . . . .	22
1.4.1 Data Collection . . . . .	22
1.4.2 RFI Mitigation . . . . .	22
1.4.2.1 Thresholding . . . . .	24
1.4.2.2 Zero-DM Subtraction . . . . .	24
1.4.3 Dedispersion . . . . .	24
1.4.4 Smoothing and Normalization . . . . .	25
1.4.5 Matched Filtering . . . . .	25
1.4.6 Clustering . . . . .	26
1.5 Theoretical Models for FRBs . . . . .	26
1.5.1 Neutron Star Models . . . . .	27
1.5.1.1 Magnetar Flares . . . . .	27
1.5.1.2 Giant Pulses . . . . .	29
1.5.1.3 Starquakes . . . . .	29
1.5.1.4 Merging and Colliding Neutron Star Models . . . . .	30
1.5.1.5 Collapsing Neutron Star Models . . . . .	31
1.5.1.6 Pulsar-orbiting Body Interactions . . . . .	31
1.5.1.7 Cosmic Combs . . . . .	32
1.5.2 Other Models . . . . .	32
1.5.2.1 Compact Object Binary Systems . . . . .	32
1.5.2.2 Neutron Star–Black Hole Mergers . . . . .	33
1.5.2.3 Black Hole–Black Hole Mergers . . . . .	34
1.5.2.4 Exotic Models . . . . .	34

1.5.3	Final Thoughts . . . . .	35
1.6	Thesis Outline . . . . .	35
2	A Deep-Learning Based Classifier For Fast Transient Classification . . . . .	37
2.1	Introduction . . . . .	37
2.1.1	Training . . . . .	39
2.1.1.1	Loss Function . . . . .	40
2.1.1.2	Gradient Descent . . . . .	40
2.1.1.3	Data Splitting . . . . .	42
2.1.1.4	Bias and Variance . . . . .	43
2.1.2	Convolutional Neural Networks . . . . .	45
2.1.3	Transfer Learning . . . . .	46
2.2	Datasets . . . . .	47
2.2.1	Surveys . . . . .	47
2.2.2	Simulating and Injecting FRBs . . . . .	50
2.2.3	Train and Test Datasets . . . . .	51
2.2.4	Data Augmentation . . . . .	53
2.2.4.1	Frequency-Time Flip . . . . .	53
2.2.4.2	DM-Time Flip . . . . .	53
2.3	Methods . . . . .	55
2.3.1	Input Data Standardization . . . . .	55
2.3.2	Network Architecture . . . . .	56
2.3.2.1	Training . . . . .	57
2.3.2.2	Network Fusion . . . . .	59
2.3.3	Metrics . . . . .	60
2.4	Results . . . . .	61
2.4.1	Model Selection . . . . .	61
2.4.1.1	Two-Phase Training Approach . . . . .	61
2.4.2	Evaluating Performance on Independent Data (and Actual FRB Detections) . . . . .	64
2.4.2.1	Data . . . . .	64
2.4.2.2	Model Performance . . . . .	65
2.5	Discussion . . . . .	67
2.5.1	Inference Speeds and Size . . . . .	67
2.5.2	Input Shapes . . . . .	67
2.5.3	Sensitivity Analysis . . . . .	69
2.5.4	Fine Tuning . . . . .	71
2.5.5	Comparison to Previous Work . . . . .	71
2.5.6	FETCH . . . . .	72
2.6	Conclusions . . . . .	73
3	Initial Results From a Realtime FRB Search With the GBT . . . . .	74
3.1	Introduction . . . . .	74
3.2	Search Pipeline . . . . .	75
3.3	Pipeline Benchmarks . . . . .	80

3.3.1	Blind FRB injections . . . . .	80
3.3.2	Evaluation Metrics . . . . .	81
3.4	Results . . . . .	83
3.5	Discussion . . . . .	86
3.5.1	Time to first GREENBURST detection . . . . .	86
3.5.2	The all-sky FRB rate . . . . .	86
3.5.3	Detection rate forecasts for other surveys . . . . .	90
3.5.4	Source Count Index . . . . .	91
3.6	Conclusions . . . . .	93
4	A Fast Radio Burst in the Direction of the Virgo Cluster . . . . .	94
4.1	Introduction . . . . .	94
4.2	Observations . . . . .	96
4.3	Results . . . . .	96
4.3.1	FRB 180417 . . . . .	96
4.3.2	Radio Follow-up Observations . . . . .	100
4.3.3	Optical Follow-up . . . . .	100
4.4	Implications of FRB 180417 . . . . .	103
4.4.1	Is FRB 180417 in the Virgo cluster? . . . . .	103
4.4.2	Probing the Virgo Intra-cluster Medium . . . . .	104
4.4.3	The FRB Luminosity Function . . . . .	105
4.5	Conclusions . . . . .	109
5	Conclusions . . . . .	110
5.1	FETCH . . . . .	110
5.2	GREENBURST . . . . .	112
5.3	A Fast Radio Burst in the Direction of Virgo . . . . .	116
5.4	Looking Ahead . . . . .	117

## List of Tables

1.1	Redshift measurements of localized FRBs . . . . .	17
1.2	FRB rates from three of the largest surveys . . . . .	21
2.1	Data sources for used for training the CNNs . . . . .	49
2.2	Parameter Distribution for Simulated FRBs . . . . .	50
2.3	Top-5 models for frequency-time and DM-time inputs . . . . .	60
2.4	Top-11 models with their corresponding metrics on test data. . . . .	63
2.5	Precision and recall values on real FRB data . . . . .	65
2.6	Results of model evaluation on Real FRB data . . . . .	66
3.1	Distributions of FRBs injected for benchmarking the pipeline . . . . .	80
3.2	GREENBURST observational summary to date . . . . .	84
3.3	Known pulsars detected by GREENBURST during commensal observations. . . . .	85
3.4	FRB detection rate predictions for various telescopes . . . . .	90
4.1	Detection S/N of FRB 180417 . . . . .	98
4.2	Observed properties of FRB 180417 . . . . .	98
4.3	Details of the radio follow-up of FRB 180417. Here $F_{\min}$ is the minimum fluence detectable by the telescope. . . . .	101



## List of Figures

1.1	A dynamic spectrum with a single-pulse from PSR B0329+54 . . . . .	4
1.2	Geometry of radio wave scattering in the ISM. . . . .	6
1.3	Dynamic spectrum and dedispersed profile showing the Lorimer Burst. . . . .	9
1.4	FRB 121102 157 day periodicity . . . . .	11
1.5	FRB DMs and Scattering Times vs Galactic Latitude . . . . .	12
1.6	Sample of FRBs from ASKAP fly’s eye survey . . . . .	14
1.7	FRB 121102 sad trombone effect . . . . .	15
1.8	The Macquart relation . . . . .	19
1.9	FRB Search Pipeline . . . . .	23
1.10	Flaring magnetar shell model . . . . .	28
2.1	Schematic diagram of a neuron . . . . .	38
2.2	Schematic of a DNN with $(L + 1)$ -layers of neurons. . . . .	39
2.3	Bias–Variance Trade-off . . . . .	44
2.4	VGG16 Convolutional Neural Network . . . . .	45
2.5	Sample images of high S/N candidates from the training and test dataset . . . . .	48
2.6	Distribution of S/N of the simulated FRBs. . . . .	50
2.7	FETCH network architecture . . . . .	54
2.8	Frequency-time and DM-time model training flowchart . . . . .	57
2.9	Fused model training flow chart. . . . .	58
2.10	Time taken for classifying one candidate by various models . . . . .	68
2.11	Heatmap for accuracies of differently sized frequency-time inputs . . . . .	68
2.12	Recall vs Signal to noise (S/N) for top-11 models. . . . .	70
3.1	Schematic depiction of the GREENBURST detection pipeline . . . . .	76
3.2	Radio frequency interference clipping using the Savitzky–Golay filter. . . . .	78
3.3	The parameteric recall curve for the GREENBURST search pipeline . . . . .	82
3.4	Sky coverage during GREENBURST commensal observations. . . . .	84
3.5	Brightest single pulses from various pulsars detected by GREENBURST . . . . .	87
3.6	Joint and marginalized probability density functions for the FRB rate, $\mathcal{R}$ , and source count index, $\alpha$ . . . . .	89
3.7	Model FRB source counts for various models . . . . .	92
4.1	The ASKAP footprint overlaid on the image of the Virgo cluster of galaxies. . . . .	95
4.2	The dedispersed profile and dynamic spectrum for FRB 180417 . . . . .	97
4.3	The auto-correlation function of the spectrum of FRB180417. . . . .	99
4.4	PROMPT5 image at the FRB 180417 position . . . . .	102
5.1	Performance for FETCH models on different GPUs. . . . .	111
5.2	Detection of a burst from FRB 190520D using GREENBURST . . . . .	113
5.3	Detection of the second burst from FRB 190520 using GREENBURST . . . . .	114
5.4	Updated FRB Rates and source count index . . . . .	115

# Chapter 1

## Introduction

### 1.1 Fast Radio Transients

The term fast radio transients is commonly used to describe millisecond-duration pulses that are produced by a coherent source of non-thermal radio emission. The field of fast radio transients began serendipitously in 1967 with the discovery of pulsars by Jocelyn Bell (Hewish et al., 1968). Pulsars are highly magnetized, rapidly rotating neutron stars that emit pulsed radio emission much like a lighthouse. Typical rotation periods are of a few hundred ms but span a wide range from 1.4 ms to 30 s. To date 2811 pulsars have been cataloged (Manchester et al., 2005) and the sample is readily available online<sup>1</sup>. Given their periodicity, typical pulsar searches make use of Fourier-domain techniques or brute-force folding. For the former, we take the Fourier transform of the signal and look for significant peaks in the frequency spectrum. In the latter case, we employ efficient folding algorithms like the Fast Folding Algorithm (FFA; Staelin, 1969). A review of both techniques can be found in Burns & Clark (1969). In both cases, as will be discussed in detail later, the effects of frequency dispersion due to ionized plasma along the line of sight need to be mitigated.

Using the FFA, Staelin & Reifenstein (1968) reported the detection of a pulsar from the Crab nebula and its extraordinarily bright individual pulses. These pulses are called Giant Pulses (GPs), and while there is no fixed definition, GPs are typically  $> 10 - -100$  times more intense than the average pulsar signal (Johnston & Romani, 2004). McLaughlin & Cordes (2003) describe the details for single-pulse searches in the context of giant pulses from extragalactic pulsars. Soon after, McLaughlin et al. (2006) reported the detection of 10 so-called “rotating radio transients” (RRATs) from a search of archival Parkes Multibeam Survey data (Manchester et al., 2001). RRATs are highly intermittent Galactic pulsars, which are detected through single-

---

<sup>1</sup><https://www.atnf.csiro.au/people/pulsar/psrcat>

pulse searches. Due to their intermittent nature, it is hard for them to be detected via regular periodicity searches. For some RRATs we have only detected a handful of pulses, making it difficult to determine their periods.

While in search of single-pulses from sources outside our Galaxy, Lorimer et al. (2007) analyzed archival data from the Magellanic Clouds and discovered a single-pulse with a frequency dispersion far higher than could be accounted by the Milky Way alone. This pulse, known colloquially as the *Lorimer Burst*, has an intrinsic pulse width of 5 ms. Substantial support in favor of this burst being an astrophysical phenomenon came from a single-pulse found by Keane et al. (2012), and four other sources discovered by Thornton et al. (2013). The latter authors dubbed these sources “Fast Radio Bursts” (hereafter FRBs) as a new population of cosmological origin. Like gamma-ray bursts, FRBs are named using the year, month and day of the observation. For example, the Lorimer burst, originally found in data collected on August 24, 2001, is known as FRB 010724. This discovery sparked an interest in searches with different telescopes leading to more FRBs being reported in subsequent years from the Arecibo Telescope (Spitler et al., 2014), the Green Bank Telescope (Masui et al., 2015) and so on. Since Thornton et al. (2013), the rate of FRB discovery has been growing every year, so much so that we now have  $\sim 150$  reported FRBs<sup>2</sup> (Petroff et al., 2016). Recently, Fonseca et al. (2020) have also hinted towards the release of a 700 FRB catalog from the CHIME telescope by the end of 2020.

In 2016, a major development in the field came from follow-up observations of FRB 121102, initially discovered by Spitler et al. (2014), when it was found to repeat (Spitler et al., 2016). FRB 121102 remained the only repeater for several years until the Canadian Hydrogen Intensity Mapping Experiment (CHIME) reported the discovery of another repeater in 2019 (The CHIME/FRB Collaboration et al., 2019a). The first repeating FRB also gave astronomers a unique opportunity to localize to it to sub-arcsecond precisions using interferometers. Chatterjee et al. (2017) localized FRB 121102 using the Very Large Array (VLA) and determined that it is located in a dwarf irregular galaxy with a redshift  $z = 0.19$ . Since the initial lo-

---

<sup>2</sup>[www.frbcatalog.org](http://www.frbcatalog.org)

calization, astronomers have localized 13 FRBs<sup>3</sup> using various interferometers and have seen that FRBs are hosted in a wide range of galaxies with redshifts in the range  $0.03 \lesssim z \lesssim 0.60$  (Bhandari et al., 2020; Heintz et al., 2020). Very recently, another flurry of excitement came during the summer of 2020 when both STARE2 and CHIME telescopes detected a bright millisecond-duration radio burst from the Galactic magnetar<sup>4</sup> SGR J1935+2154 (Bochenek et al., 2020; The CHIME/FRB Collaboration et al., 2020a). The fluence<sup>5</sup> was measured to be  $> 1.5$  MJy ms at 1.4 GHz and  $\sim 700$  kJy ms at 600 MHz. The burst is similar to that of FRBs, and the source is now dubbed FRB 200428.

This thesis aims to further our knowledge of the FRBs population by developing and deploying search pipelines along with state-of-the-art machine learning models. The rest of this chapter provides a short introduction to our current understanding of the FRB phenomena and its observables, search techniques, and progenitor models.

## 1.2 Interstellar Medium

The Interstellar Medium (ISM) consists of dust and gas in the Galaxy. The gas in the ISM exists in ionic, atomic, and molecular form. As radio waves travel through the ISM, they undergo several propagation effects which critically impact the signals we receive from pulsars and FRBs. We review these effects in the subsections below.

### 1.2.1 Dispersion

Propagating radio waves interact with the ionized plasma in the ISM. The plasma is dispersive in its nature, meaning its refractive index ( $\mu$ ) is frequency dependent. For a wave of frequency  $\nu$ , we have

$$\mu = \sqrt{1 - \frac{\nu_p^2}{\nu^2}}, \quad (1.1)$$

---

<sup>3</sup>[www.frbhosts.org](http://www.frbhosts.org)

<sup>4</sup>Magnetars represent another manifestation of neutron stars with magnetic fields in the range  $10^{13}$ – $10^{15}$  G.

<sup>5</sup>Integrated pulse energy given by the product of peak flux density and equivalent pulse width. A fluence of 1 MJy ms would correspond to a pulse of  $10^6$  Jy flux and 1 ms width.

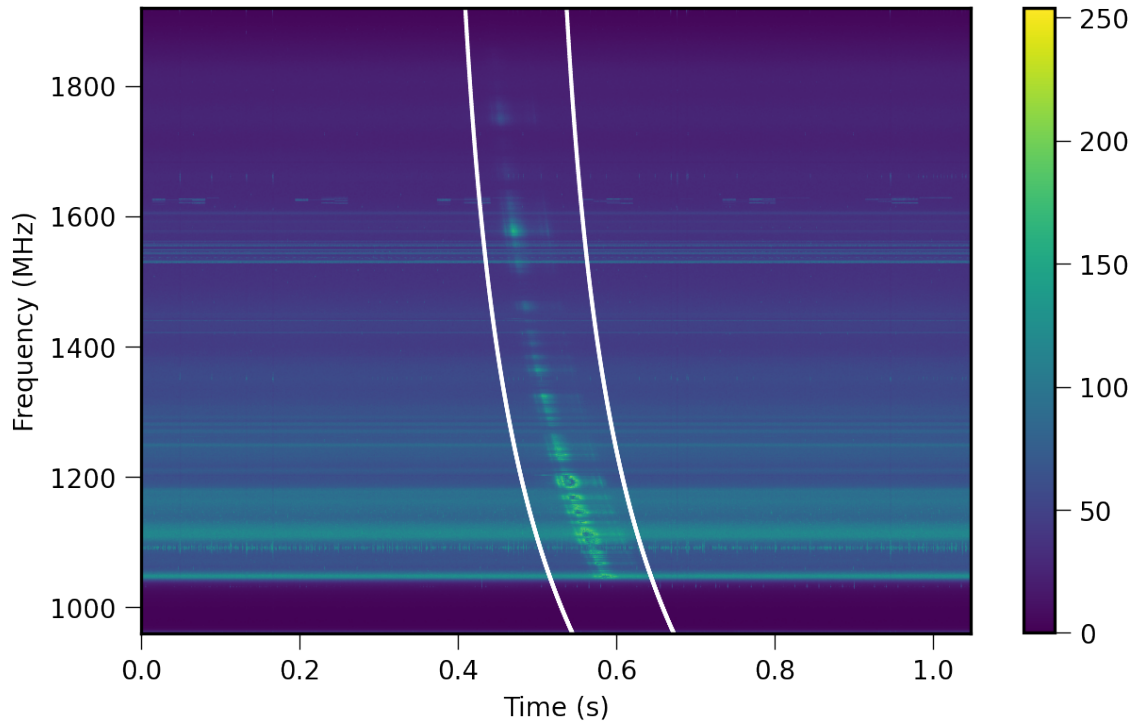


Figure 1.1: A dynamic spectrum with a single-pulse from PSR B0329+54. The x-axis shows the time, y-axis denotes the observed frequency and the color bar shows the flux in arbitrary units. The bright patch in the middle shows the quadratic frequency sweep with higher frequencies arriving first at the telescope than lower frequencies. The white lines denote the expected dispersion curve computed using the DM of the pulsar.

with the plasma frequency

$$\nu_p = \sqrt{\frac{n_e e^2}{\pi m_e}}. \quad (1.2)$$

Here  $n_e$ ,  $m_e$  and  $e$  are electron density, mass and charge respectively. The group velocity of radio waves ( $v_g$ ) is less than the speed of light ( $c$ ) as  $v_g = c\mu$ . Due to this, higher frequency waves travel faster than the lower frequency waves. We can derive the time delay due to dispersion,

$$t = \left( \int_0^d \frac{dl}{v_g} \right) - \frac{d}{c}, \quad (1.3)$$

where  $d$  is the distance to the source from Earth. This yields,

$$t = \left( \frac{e^2}{2\pi m_e c} \frac{1}{\nu^2} \int_0^d n_e dl \right) - \frac{d}{c}. \quad (1.4)$$

We term the integral of the electron density over the distance to the source as the dispersion measure (DM) and is measured in the units of  $\text{pc cm}^{-3}$ . As can be seen, the arrival time has an inverse square dependence on the frequency often referred to as the frequency sweep. This can be observed in Figure 1.1 where we can see the higher frequencies arriving first and the inverse square dependence of time on the frequency. We can use the above expression to compute the dispersion delay ( $\Delta t$ ) between two observed frequencies ( $\nu_1$  and  $\nu_2$ , measured in MHz) as follows:

$$\Delta t = 4.15 \times 10^6 \text{ DM} \left( \frac{1}{\nu_1^2} - \frac{1}{\nu_2^2} \right) \text{ ms}. \quad (1.5)$$

The DM is used as a proxy for distance as one needs to integrate the electron density along the observing line of sight out to the source. For Galactic sources, two commonly used models for the electron density are known as NE2001 (Cordes & Lazio, 2002) and YMW16 (Yao et al., 2017). For extragalactic sources, the DM includes several other contributions which are discussed in subsection 1.3.2.1.

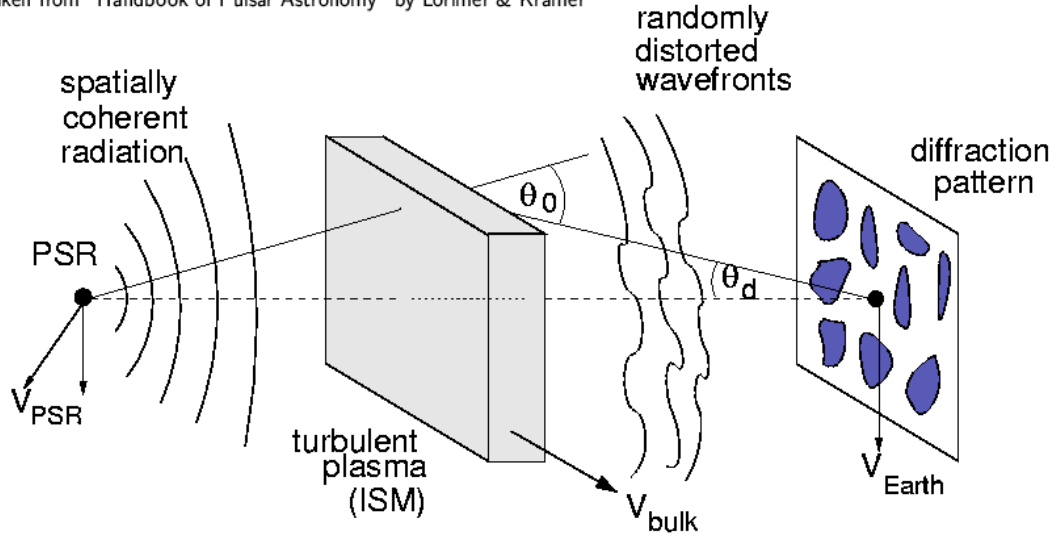


Figure 1.2: The geometry of the scattering of radio waves in the ISM. The pulsar is denoted by PSR on the left side of the figure, emitting spatially coherent radiation. The turbulence in the plasma is modeled by a screen halfway between the observer and the pulsar. The block distorts the wavefronts leading to scattering of waves. The figure is taken from Lorimer & Kramer (2004).

### 1.2.2 Scattering

Due to the fluctuations in the electron density in the ISM, the radio waves also get deflected. Thus, some waves take longer paths to reach the observer on Earth and can be seen as exponential tails to the pulse profiles. To discuss the effects of Galactic scattering, we make a simplifying assumption that the effects of scattering medium can be described by a thin screen that concentrates all the ISM inhomogeneities (Scheuer, 1968). This can be easily visualized with the help of Figure 1.2 (Cordes, 2002).

The distortions in the inhomogeneous ISM distort the wave fronts which are quantified as the phase shifts ( $\delta\Phi$ ). After propagating through a turbulent thin ISM screen of thickness  $a$ , the phase shifts are given by  $\delta\Phi = \Delta ka$ , where  $k = (2\pi/c)\mu\nu$ ,  $\mu$  is the refractive index and  $\nu$  is the wave frequency. Using Equation 1.1 and Equation 1.2 and substituting for  $\mu$  and  $\nu_p$ , we obtain

$$\delta\Phi = \frac{2e^2}{cm_e} \frac{a\Delta n_e}{\nu}. \quad (1.6)$$

The root mean square (rms) variation in phase due to encountering  $d/a$  such irregularities for a distance of  $d$  between the source and the observer, and electron density variations  $\Delta n_e$ ,

$$\Delta\Phi \simeq \sqrt{\frac{d}{a}}\delta\phi = \frac{2e^2}{cm_e} \frac{\sqrt{ad}\Delta n_e}{\nu}. \quad (1.7)$$

This can be viewed as the bending of a wavefront by an angle  $\theta_0$  at the screen. The result of this bending is observed as a diffuse disk centered around the point source with an angular radius

$$\theta_d = \frac{\theta_0}{2} = \frac{\Delta\Phi}{2ka} \simeq \frac{e^2}{2\pi m_e} \frac{\Delta n_e}{\sqrt{a}} \frac{\sqrt{d}}{\nu^2}. \quad (1.8)$$

The angular intensity distribution for a Gaussian scattering screen,

$$I(\theta)d\theta \propto \exp\left(-\frac{\theta^2}{\theta_d^2}\right)2\pi\theta d\theta. \quad (1.9)$$

The waves observed at an angle  $\theta$  arrive later than the undeflected waves and the time delay is given by  $\Delta t = \theta^2 d/c$ . The intensity as a function of time,

$$I(t) \propto \exp(-c\Delta t/\theta_d^2 d) = e^{-\Delta t/\tau_s}, \quad (1.10)$$

where the scattering time scale

$$\tau_s = \frac{e^4}{4\pi^2 m_e^2} \frac{\Delta n_e^2}{a} d^2 \nu^{-4}. \quad (1.11)$$

As a result, a emitted pulse, is observed as a the intrinsic pulse shape convolved with an exponential with scattering time scale  $\tau_s$ .

It should be noted that these are the same electrons that lead to the dispersion of radio waves. As a result, one would expect larger DM values corresponding to larger scattering time scales. This DM–scattering time scale relation is clearly visible for pulsars (see e.g., Bhat et al., 2004); on the other hand, FRBs, have much larger DMs, their extragalactic contributions seem to lack any such relationship (Qiu et al., 2020).



## 1.3 Fast Radio Bursts

As introduced above, fast radio bursts (FRBs) are enigmatic astrophysical objects that burst for millisecond durations with flux densities of the order of a few Janskys, with the prototype source discovered by Lorimer et al. (2007). FRBs show the characteristic inverse frequency-squared sweep in observing frequency, described above, quantified by the DM. Their DMs are substantially larger than those expected from the Milky Way in the direction of detection, indicating their extragalactic nature.

The *Lorimer Burst*, FRB 010724, was found during a single-pulse search of archival data from Parkes Radio Telescope observing the Small Magellanic Cloud (SMC). Figure 1.3 shows the dynamic spectra and pulse profile. The pulse is estimated to have a peak flux density greater than 30 Jy and was so bright that it saturated the receiver. This can be seen as the change in the baseline right after the burst in Figure 1.3. The observed DM of the burst is  $375 \text{ pc cm}^{-3}$ , while the total Galactic contribution to the DM along the line of sight is predicted to be  $\sim 25 \text{ pc cm}^{-3}$  and  $\sim 30 \text{ pc cm}^{-3}$  for the Galactic halo. Thornton et al. (2013) later added four more sources from the Parkes High Time Resolution Survey (Keith et al., 2010), which confirmed the existence of an all-sky population of radio transients that are extragalactic in nature. Together with these sources, the Lorimer burst, and another highly dispersed transient found by Keane et al. (2012), the sample of six sources were dubbed FRBs.

### 1.3.1 Repeating FRBs

Up until 2016, due to follow-up observations of the Lorimer burst and other FRBs not resulting the detection of additional bursts, FRBs were thought of as one-off events. Spitler et al. (2014) reported the discovery of FRB 121102 from the PALFA survey using the Arecibo Telescope. This was the first FRB found from a telescope other than Parkes Radio Telescope. During a follow-up observation of FRB 121102, Spitler et al. (2016) found additional bursts at the same DM confirming that there is

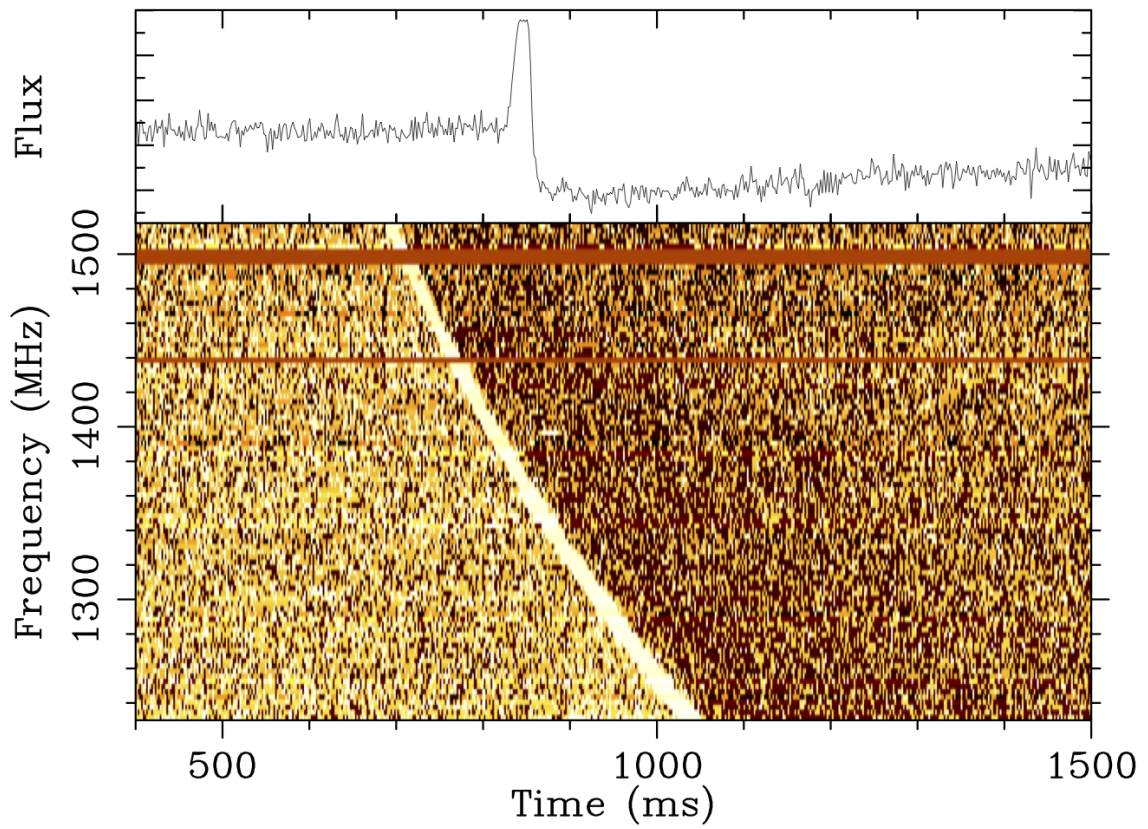


Figure 1.3: Dynamic spectrum (bottom) and dedispersed profile (top) showing the Lorimer burst, FRB 010724. Figure taken from Cordes & Chatterjee (2019).

a repeating FRB. The first repeater also provided many opportunities that were not possible with the one-off FRBs, namely studying them at multiple wavelengths and affording a means of precision sky localization.

Scholz et al. (2016), Hardy et al. (2017), and Zhang et al. (2018) studied FRB 121102 on frequencies from 800 MHz to 5 GHz while also sometimes shadowing with X-ray, optical, and  $\gamma$ -ray telescopes. Several bursts in the radio band were detected, but no emission at other wavelengths was found. Using the Very Large Array interferometer Chatterjee et al. (2017) localized the FRB and found a coincident persistent radio source. Tendulkar et al. (2017) used optical observations to detect the corresponding optical source leading to a low-metallicity, irregular dwarf galaxy located at a redshift of  $z = 0.19$ . This was the first direct confirmation of FRBs' extragalactic nature and the first identification of a host galaxy.

In 2019, The CHIME/FRB Collaboration et al. (2019a) reported the detection of a second repeater, FRB 180814.J0422+73, indicating a substantial population of repeating FRBs. Later that year, The CHIME/FRB Collaboration et al. (2019b) reported the discovery of eight new repeaters, and Kumar et al. (2019) reported faint repetitions from an FRB discovered by ASKAP.

Recently, Fonseca et al. (2020) have reported the discovery of nine new repeaters from the CHIME telescope, bringing the total repeater count to 19. Also, Marcote et al. (2020) localized FRB 180916 to a spiral galaxy at a redshift of  $z = 0.03$ , indicating that repeaters can originate from a diverse range of host galaxies.

### 1.3.1.1 Periodic Repeaters

With the detection of repeat bursts from at least some FRBs, the natural next step is to look for a pattern of repeatability. With a densely sampled<sup>6</sup> set of FRB 121102 bursts, many attempts towards finding an underlying periodicity were made. A detailed discussion on placing the constraints of such searches can found in Zhang et al. (2018).

While no periodicity has been found within the bursts, Rajwade et al. (2020) and

---

<sup>6</sup>Here by dense, we mean several bursts in a contiguous observation.

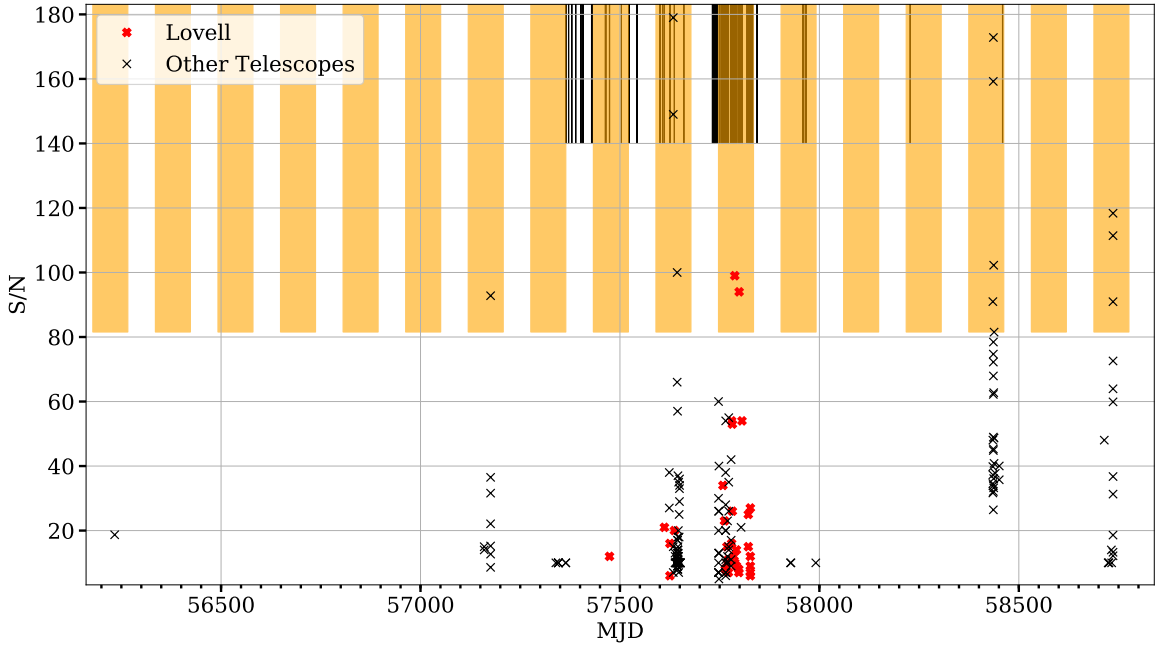


Figure 1.4: S/N vs. Detection MJD for FRB 121102 Bursts. Vertical black lines represent the observations, and red squares represent the bursts detected from the Lovell Telescope. The black cross represents the detections from other telescopes. The orange regions show the periodic active period for the FRB. Figure from Rajwade et al. (2020).

The CHIME/FRB Collaboration et al. (2020b), reported the periodicity inactivity windows of FRB 121102 and FRB 180916, respectively. The sources go into ‘off’ and ‘on’ states, with FRB 121102 having a 157 days period with 57% duty cycle and FRB 180916 having a 16 days period with 31% duty cycle, respectively. Figure 1.4 shows the ‘off’ and ‘on’ windows along with the detected bursts from various telescopes for FRB 121102.

### 1.3.2 Observables

While the origins of FRBs are still uncertain, their observed properties have given us several important clues over the last decade. This section discusses these FRBs and their implications towards origin and emission mechanisms.

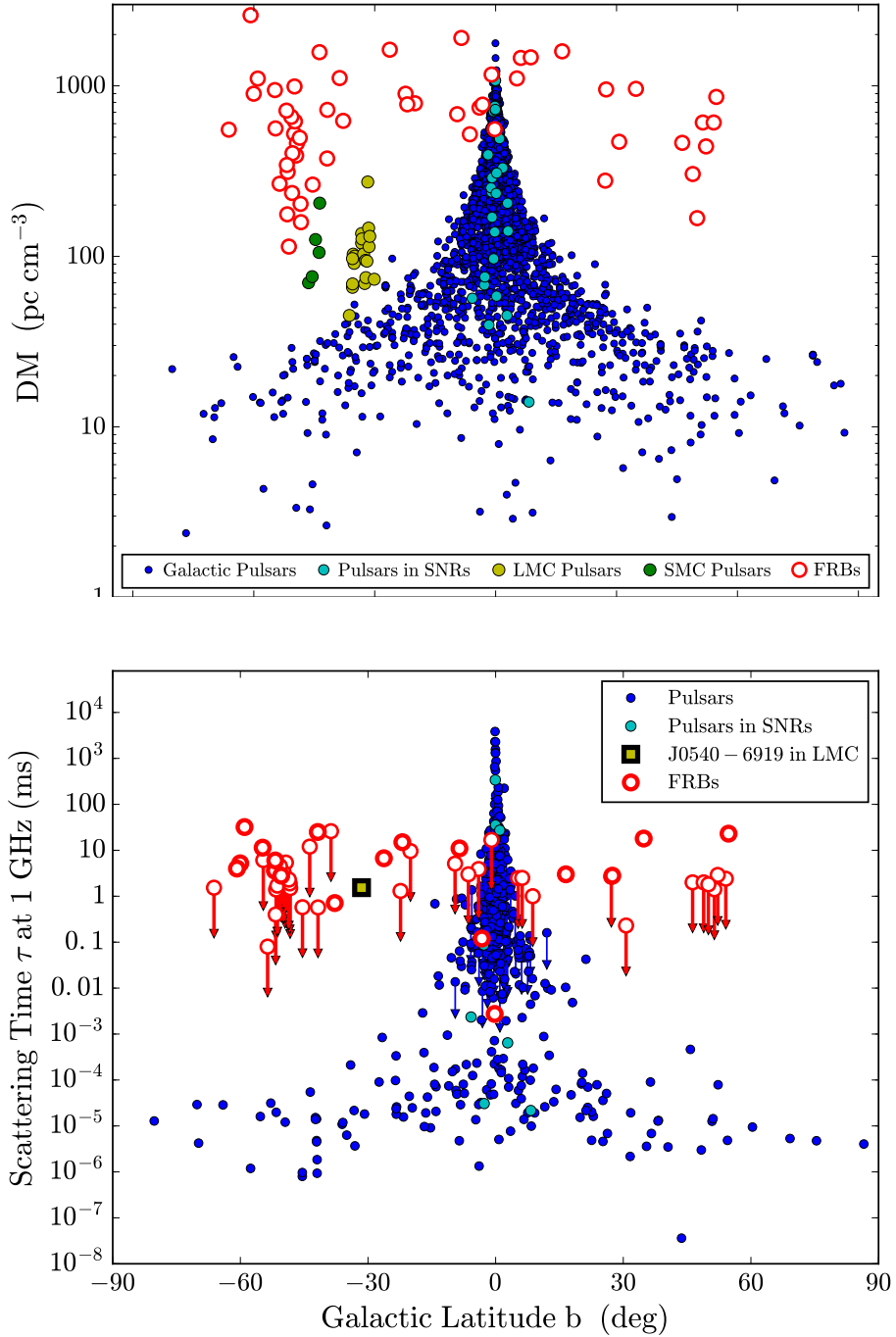


Figure 1.5: DM and scattering times for FRBs and pulsars as a function of Galactic latitude. Blue dots represent the pulsars, and red circles represent the FRBs. Yellow circles show pulsars in the Large Magellanic Cloud, and green circles show pulsars in Small Magellanic Cloud. Due to the added DM contribution from the Magellanic Clouds, these pulsars have higher DM and scattering values when compared to other pulsars are similar latitude. These values for FRBs are independent of the observed latitude. Figure taken from Cordes & Chatterjee (2019).

### 1.3.2.1 Dispersion and Scattering

The time of arrival of FRB pulses follows the inverse squared frequency dependence as derived in Equation 1.5 due to dispersion. The DM contributions of the FRB can be written as the following sum:

$$DM_{\text{FRB}} = DM_{\text{ISM}} + DM_{\text{IGM}} + DM_{\text{Host}}. \quad (1.12)$$

Here  $DM_{\text{ISM}}$  is the DM contribution from the interstellar medium and the halo of our Galaxy and is often estimated using electron density models like NE2001 (Cordes & Lazio, 2002)<sup>7</sup> and YMW16 (Yao et al., 2017).  $DM_{\text{IGM}}$  is the contribution from the intergalactic medium and  $DM_{\text{Host}}$  is the contribution from the host galaxy.

Figure 1.5 (left) shows the DM distribution of pulsars (blue circles) and FRBs (red circles) as a function of Galactic latitude. The apparent dichotomy between the two populations, in which we see that the FRB distribution shows no correlation with Galactic latitude, highlights FRBs’ extragalactic nature and that most of the contribution is from outside our Galaxy (i.e., via the ISM and the host galaxy).

Figure 1.5 (right) shows the measured scattering time-scaled to 1 GHz and highlights another critical difference between pulsars and FRBs. Here it is seen that: (i) scattering timescales are independent of Galactic latitude; (ii) scattering is large but lower than that of pulsars close to the Galactic plane. Further to the latter point, given that FRBs generally have DMs comparable to the highest DMs seen for pulsars, the scattering is typically lower than would be expected for such high DM sources if they are Galactic in origin. This can be easily understood in terms of a lever-arm effect whereby most of the scattering contribution comes from a screen of material close to the source (see, e.g., Williamson, 1972).

### 1.3.2.2 Dynamic Spectrum

For pulsars, the single-pulse (or even folded pulse) dynamic spectra show simple temporal morphologies: single or multi-component Gaussian-like pulses and, in

---

<sup>7</sup>The halo contributions is modeled by the YWM16 model but not by the NE2001 model.

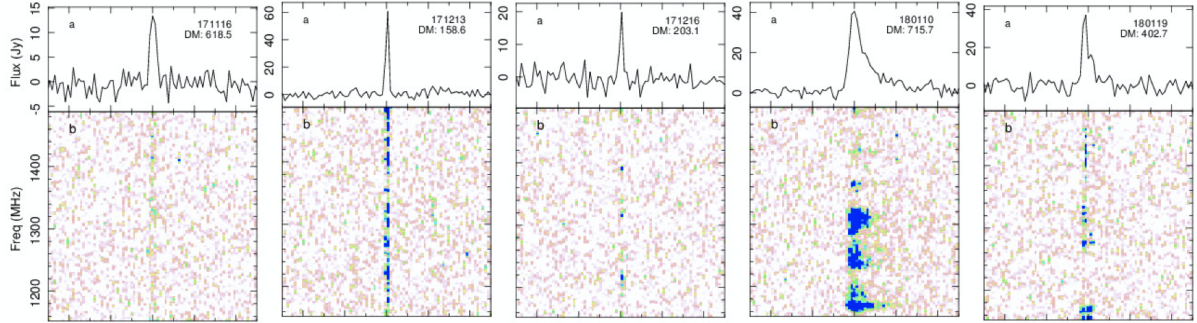


Figure 1.6: Sample of five FRBs from ASKAP fly’s eye survey. The bottom panels show the dedispersed frequency–time structure. The top profile shows the frequency integrate profile for the five FRBs. As can be seen here, these FRBs show variety of frequency–time structure with some showing flat spectral response while others are showing patchy and scattered structure. Figure from Shannon et al. (2018).

some cases, modified by scatter-broadening. When observed over a broad bandwidth (over several 100 MHz), the effects are intrinsic profile evolution, scintillation, and spectral index where the intensity increases or decreases as a power–law function of the observing frequency.

For FRBs, a wide range of time–frequency structure has been seen. Farah et al. (2018) used coherent dedispersion to show rich microstructure in FRB 170827. The dynamic spectrum displayed 100–200 kHz striations and spiky features brighter than 1 kJy. The temporal profile also showed three components, a sharp leading edge, a weak intermediate component, and a broad trailing edge. The effects of propagation through the ISM of the Milky Way cannot explain these spectral features as these are much narrower than expected from the NE2001 model. The authors described the complex frequency temporal structure with a two scattering screen model, where one screen is placed within our Galaxy and the second near the source. Shannon et al. (2018) released a sample of 20 bright FRBs discovered using the ASKAP telescope, where all of the FRBs showed strong spectral modulation. Figure 1.6 shows a sample of these ASKAP FRBs. Many FRBs out of the sample exhibit power concentrated in narrower few-MHz broad structures, with signals absent in large fractions of the band. Due to the telescope’s limited frequency and time resolution, it is hard to study these features in greater detail. Similar frequency and time structure have been studied using coherently dedispersed data by Cho et al. (2020) and Day et al. (2020) showing

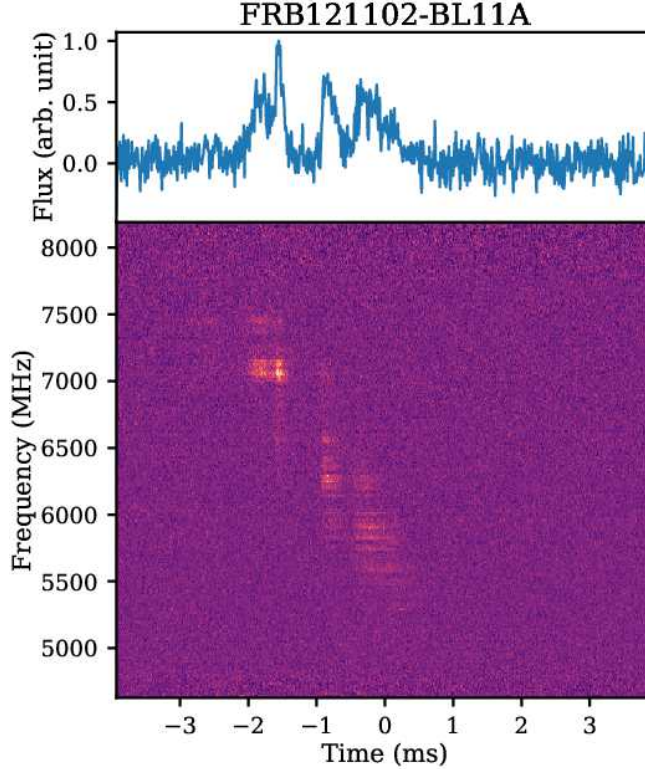


Figure 1.7: The “sad trombone” effect in FRB 121102. The bottom plot shows the frequency time structure of a burst observed by Gajjar et al. (2018). The top plot shows the frequency integrated profile. The frequency time structure shows a downward drift with three distinct peaks. Figure taken from Cordes & Chatterjee (2019).

several components within a burst and sometimes with slightly different DMs.

The dynamic spectrum has been studied in greater detail for the repeating FRBs, primarily FRB 121102. Frequency structure similar to the ASKAP FRBs can also be seen in different bursts of FRB 121102 independent of the observing frequency (Gajjar et al., 2018; Hessels et al., 2019). One peculiar feature which seems to be limited to repeaters only is the downward frequency drift of the pulse components. This is sometimes called the *sad trombone effect* and can be seen in Figure 1.7. This effect is also visible in several other repeaters, as reported by The CHIME/FRB Collaboration et al. (2019a,b), and remains an unresolved problem.



### 1.3.2.3 Polarization

Polarization properties have been studied for a tiny subset of  $< 20$  FRBs. This is because most of the FRBs are found in pulsar or commensal surveys where only total intensity is recorded instead of 4 Stokes parameters. From the subset of FRBs with available Stokes information, linear polarization ranges from 8.5% (FRB 150418, Keane et al., 2016) to 100% (FRB 121102, Michilli et al., 2018) and circular polarization from 3% (FRB 150215, Petroff et al., 2017) to 70% (FRB 180301, Luo et al., 2020). The repeating FRB 121102 shows 100% linear polarization while 0% circular polarization. Another repeating FRB, FRB 180301 showed 30% linear polarization and 70% circular polarization during its initial detection at the Parkes Radio Telescope (Price et al., 2019). However, during the follow-up observations with the FAST telescope, Luo et al. (2020) found up to 80% linear polarization. These variations in both linear and circular polarization are similar to that of single-pulses of pulsars.

On the other hand, pulsars also show a swing in the pulse profile polarization angle (PA). During the on-pulse phase of the pulsar, the PA shows an S-shaped curve, which is understood within the framework of the rotating vector model originally developed for pulsars by Radhakrishnan & Cooke (1969). According to this model, the PA is tied to the magnetic field lines and changes smoothly as the line of sight intersects different field lines at different angles. In the case of FRBs, there is a wide variety of PA variations. For some FRBs the PA rotates  $\sim 10$ s of degrees (FRB 150523, Masui et al., 2015), while some show no PA variation at all (FRB 121102, Michilli et al., 2018), (FRB 150215, Petroff et al., 2017) and (FRB 150807, Ravi et al., 2016). Recently, Luo et al. (2020) show all these variations in several repeat bursts detected by the FAST telescope for FRB 180301.

Lastly, similar to other polarization properties, the rotation measure (RM)<sup>8</sup> also show large variations. The FRB 121102 stands out with an exceptionally large RM value of  $10^5$  rad m<sup>-2</sup> indicating a strong magnetic field near the FRB engine (Michilli et al., 2018). Next is FRB 180301 with  $-3100$  rad m<sup>-2</sup>. For the rest of the FRBs, the

---

<sup>8</sup>Defined as  $RM = 0.86 \int_0^L n_e B_{\parallel} dl$  rad m<sup>-2</sup>, where  $B_{\parallel}$  is the parallel component of the magnetic field.

FRB	RA (hh:mm:ss.ss)	Dec (dd:mm:ss.ss)	Telescope	DM (pc cm <sup>-3</sup> )	$z$	Repeater
200430	15:18:49.52	12:22:35.8	ASKAP	380.0	0.1600	No
191001	21:33:24.44	-54:44:54.7	ASKAP	507.9	0.2340	No
190714	12:15:55.09	-13:01:16.0	ASKAP	504.1	0.2365	No
190711	21:57:40.63	-80:21:29.3	ASKAP	593.1	0.5220	Yes
190614	04:20:17.71	+73:42:22.9	VLA	959.2	0.60	No
190611	21:22:58.71	-79:23:49.6	ASKAP	321.4	0.3778	No
190608	22:16:04.90	-07:53:55.8	ASKAP	338.7	0.1178	No
190523	13:48:15.43	+72:28:14.4	DSA-10	760.8	0.6600	No
190102	21:29:39.72	-79:28:32.2	ASKAP	364.5	0.2913	No
181112	21:49:23.68	-52:58:15.4	ASKAP	589.0	0.4755	No
180924	21:44:25.25	-40:54:00.8	ASKAP	362.4	0.3212	No
180916	01:58:00.28	+65:42:53.0	CHIME	348.76	0.0337	Yes
121102	05:31:58.70	+33:08:52.7	Arecibo	557	0.1927	Yes

Table 1.1: Sky coordinates, discovery telescope, DM and redshift measurements of 13 localized FRBs.

RM values are significantly lower, between 0–100 rad m<sup>-2</sup> with the maximum being  $\sim 500$  rad m<sup>-2</sup> for FRB 191108 (Connor et al., 2020). For repeaters, small changes in RM between bursts have also been noted. For FRB 121102, the root means squared variation is about 50 rad m<sup>-2</sup>, while for FRB 180301, the variations are of the order 14 rad m<sup>-2</sup> (Luo et al., 2020).

### 1.3.2.4 Localization

Sub-arcsecond resolution localizations are required to pinpoint the FRB and associate it with a counterpart source. Rapid multiwavelength follow-ups to detect afterglow-like emissions have not yielded anything to date (Williams & Berger, 2016; Petroff et al., 2017). Hence the only reliable method for direct localization is to use radio interferometers. The first FRB to be localized was the repeating source FRB 121102. Chatterjee et al. (2017) used the REALFAST system (Law et al., 2015) on the Very Large Array. As described above, this was a significant breakthrough as it led to the first identification of a host galaxy and accompanying redshift measurement.

A significant hurdle to the above technique is that it requires many hours on

source waiting for a repeat burst. A more direct method is to use an interferometer to make the initial discovery so that localization can be made from a single-pulse, which might be the only time an FRB is seen. This technique has so far been implemented on the Australian Square Kilometer Array Pathfinder (ASKAP; Schinckel et al., 2012), the Deep Synoptic Array in the USA (DSA; Kocz et al., 2019) and at Westerbork in the Netherlands (Maan & van Leeuwen, 2017). This technique stores the voltage data for a small chunk lasting several seconds from all the telescopes in a small buffer in the system memory. The search for FRBs is done traditionally on time series data, and when an FRB is detected, the voltage buffers are dumped to disk. The localization is done by forming the image in a subsequent stage after the detection has been made. To associate the FRBs with host galaxies, optical and radio images are obtained (either from archival surveys or new observations), and redshifts to the galaxies are measured.

So far, 13 FRBs have been localized, out of which 3 are repeaters. An updated list of the localized FRBs can be found at <https://frbhosts.org>. The host galaxies associated with these localized FRBs show a diverse range of properties and are not confined to a particular class. A detailed discussion of host galaxy properties of the localized FRBs can be found in Heintz et al. (2020). The FRB host galaxies exhibit a broad range of stellar mass ( $10^8$ — $6 \times 10^{10} M_{\odot}$ ), and star-formation rate ( $0.05$ — $10 M_{\odot} \text{ yr}^{-1}$ ). Heintz et al. (2020) rule out the hypothesis that FRBs strictly track stellar mass in galaxies with 99% confidence. The list of localized FRBs can be found in Table 1.1.

### 1.3.2.5 The Macquart Relation

As can be seen from Equation 1.12, the DM of the FRB has three significant contributions: (i) from the Milky Way, (ii) from the host, and (iii) from the IGM. The Galactic contribution to the DM of the FRB comes from the interstellar medium and the Galactic halo. The host contribution is from the host galaxy, including its halo and any gas local to the event, while the IGM contribution is from all other extragalactic gas. For each FRB,  $DM_{\text{IGM}}$  can be estimated by subtracting off the ex-

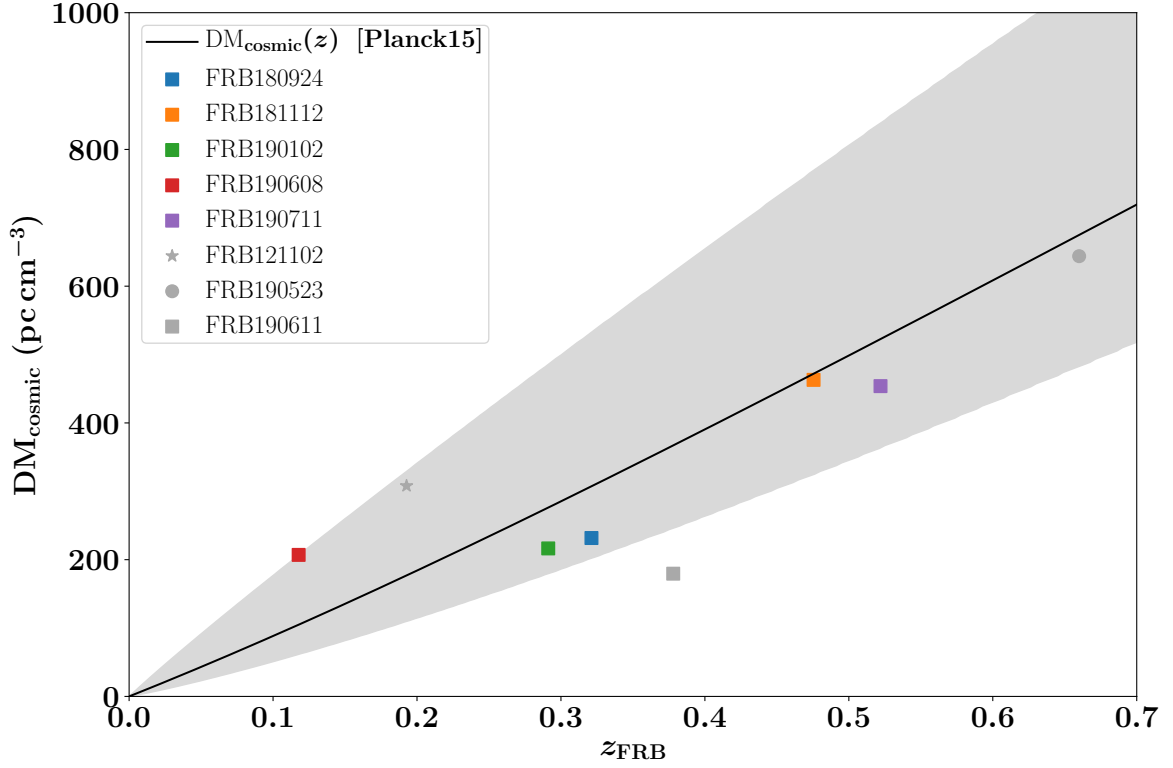


Figure 1.8: The Macquart relation showing how the  $\text{DM}_{\text{IGM}}$  (called  $\text{DM}_{\text{cosmic}}$  here) scales with the host galaxy redshift (shown as  $z_{\text{FRB}}$  here). Squares and stars denote various localized FRBs. The solid black line corresponds to the average  $\text{DM}_{\text{IGM}}$  vs. redshift while the gray shaded region is the scatter due to the large scale structure of the cosmic web. Figure taken from Macquart et al. (2020).

pected contribution from the Milky Way (including the halo) using either the NE2001 or YMW16 models mentioned above as well as a contribution from the host galaxy. The contribution from  $DM_{\text{IGM}}$  is expected to dominate and scale with redshift as it traces the ionized component of the cosmic web (Inoue, 2004). Thanks to a number of precision localizations made mostly with ASKAP over the past two years, this relationship has now been directly measured and is known as the Macquart Relation (Macquart et al., 2020) and can be seen in Figure 1.8.

FRB signals, while traveling through the IGM, probe the ionized extragalactic gas, which is part of the cosmic web. As a result, the measured  $DM_{\text{IGM}}$  values are like the average contribution from the cosmic web at the redshift of the FRB, which is inhomogeneous. The inhomogeneities lead to a scatter in the dispersion measure as a function of redshift and can be seen as the gray shaded region in Figure 1.8.

### 1.3.2.6 All-Sky FRB Rates

In an ideal case, a telescope that has an instantaneous field of view  $\Omega_s$  (sr), observes for a total time of  $T$  (days) and detects  $N_{\text{FRB}}$  sources, the implied all-sky rate

$$R_{\text{FRB}} = \frac{41253 N_{\text{FRB}}}{\Omega_s T} \text{ sky}^{-1} \text{ day}^{-1}. \quad (1.13)$$

The rates for different telescopes with different detection thresholds are then scaled to a common flux density using

$$R(> S) = R_0 \left( \frac{S}{S_0} \right)^{-\alpha}, \quad (1.14)$$

where  $R_0$  and  $S_0$  are the derived FRB rate and minimum detectable flux for a given telescope, respectively. Here  $\alpha$  is known as the source count index and has a value of  $3/2$  for a uniform distribution of standard candles in a Euclidean universe. When combining surveys carried out at different observing frequencies, it is commonly assumed (for simplicity) that FRBs spectra are flat, i.e., their flux densities are independent

Telescope/Survey	$S_0$ (Jy)	$R_0$ (sky <sup>-1</sup> day <sup>-1</sup> )	Reference
Parkes/HTRU	2	$17_{-9}^{+15} \times 10^2$	Bhandari et al. (2017)
Arecibo/PALFA	0.044	$78_{-76}^{+252} \times 10^3$	Patel et al. (2018)
ASKAP/CRAFT	29	$37 \pm 8$	Shannon et al. (2018)

Table 1.2: FRB rates from the three largest surveys.  $S_0$  represents the minimum detectable flux (in Jy), and  $R_0$  is the estimated FRB rate based on survey sensitivity, number of FRBs, and time of observations.

of observing frequency. As an example, Table 1.2 gives examples of FRB rates and thresholds from surveys carried out using three different telescopes.

For a more robust estimate of the FRB rate, in addition to considering different spectral dependencies, one needs to factor in the following elements. First, understanding the telescope’s systematic effects (sensitivity, beam pattern, bandpass, data flagged during interference mitigation) and the search techniques (number of DMs, pulse widths searched). Second, the intrinsic FRB population (source count index, spectral index of bursts, spatial distribution). A detailed treatment of selection effects and its implications for FRB rates is available in Keane & Petroff (2015).

Combining rates from different telescopes, including their selection effects, and non-detection is a difficult problem that was addressed using results from surveys completed a few years ago by Lawrence et al. (2017). Their estimates include information from 12 surveys including 15 detections and yields a rate

$$R(> S) = 578_{-306}^{+346} \text{sky}^{-1} \text{day}^{-1} \left( \frac{S}{1\text{Jy}} \right)^{-(0.91 \pm 0.34)}. \quad (1.15)$$

As can be seen, the source count index here of 0.91 is significantly smaller than the expected value assuming a Euclidean distribution of standard candles. This can be interpreted as evidence that such assumptions are not valid. We revisit this question in detail in our analysis of the FRB rate using the most recently completed surveys in chapter 3.

## 1.4 Detection of FRBs

In this section, we detail the inner workings of single-pulse search pipelines. The signals we are looking for are dispersed, faint, sometimes scattered, and often band limited<sup>9</sup>. The process of detection involves the following steps in order.

### 1.4.1 Data Collection

Radio telescopes output raw voltages, which are digitized using analog-to-digital converters. The digitized raw voltages are then channelized using a spectrometer (see, e.g., Roshi et al., 2011; Prestage et al., 2015). More details into spectrometers can be found in Burrows (2014). The channelized voltages are often converted to intensities by taking their norm, discarding the phase information. This channelized intensity time series is generally referred to as a filterbank.

### 1.4.2 RFI Mitigation

Human-made radio emissions such as radars, locationing systems like GPS, broadcasting systems, and wireless internet routers often pollute the radio band. This is undesirable since it limits radio telescopes' sensitivity and, if left unchecked, can make it virtually impossible to detect an astrophysical signal. This unwanted effect is termed Radio Frequency Interference (RFI). Most radio telescopes are located in relatively remote areas where it is possible to establish radio-quiet zones. Nevertheless, the RFI is inevitable and often stronger (sometimes by several orders of magnitude) than the astrophysical signals we are looking for and hence needs to be mitigated. RFI can be broadly classified into two categories: (1) broadband, which is spread over all the channels; (2) narrowband, which appears over a small fraction of the band. Two different kinds of techniques are used to mitigate these effects and are discussed as follows.

---

<sup>9</sup>Present in a small part of the band as compared to the whole observing bandwidth (see, e.g., Kumar et al., 2019).

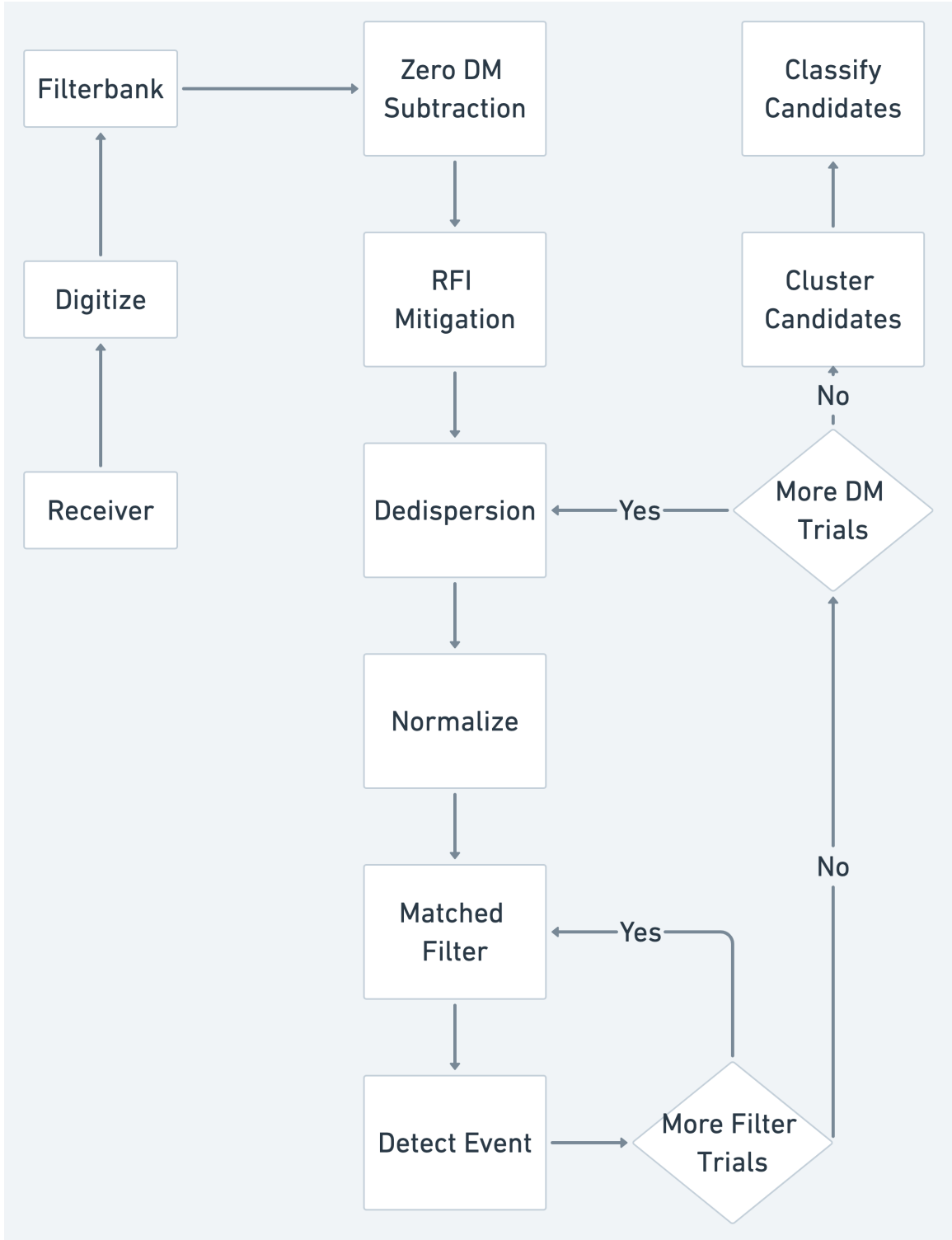


Figure 1.9: Schematic of single-pulse search pipelines. The data from the telescope receiver is digitized and recorded in a filterbank style format. The data are then zero-DM subtracted, and RFI mitigation is performed. The cleaned data are dedispersed for many trial DMs and normalized. The normalized dedispersed time series are then searched for several widths using matched filtering. The candidates are then clustered, and the best candidate for each cluster are verified either by machine learning algorithms or by humans.



### 1.4.2.1 Thresholding

Most narrowband RFI mitigation techniques work on the underlying assumption that the noise in the data follows Gaussian statistics. These techniques look for outliers and deviations from Gaussian statistics to flag the RFI. Once the RFI is flagged, it is often either replaced by zeros or the data’s median before any searching analysis is carried out. Thresholding is the most common technique used for RFI mitigation. Here the median and the median standard deviation ( $\sigma$ ) of a chunk of the data is computed, and data values above a certain threshold (for example,  $6\sigma$ ) are flagged as RFI.

### 1.4.2.2 Zero-DM Subtraction

Broadband RFI, appearing across all the channels, can easily be identified by the lack of dispersion and appears at a DM of zero. The mitigation technique first proposed by Eatough et al. (2009) is as follows. The filterbank data are averaged over the channels resulting in a time series with DM of zero. The resultant time series is subtracted from all the channels separately. In the modern-day pipelines, more sophisticated versions are used. For example, HEIMDALL (Barsdell, 2012) creates the zero DM time series and searches for peaks above  $5\sigma$ . These peaks are then flagged as RFI, and the data are replaced by randomly selecting values in time  $< \pm 0.25$  s.

### 1.4.3 Dedispersion

As discussed in subsection 1.2.1, the radio signals are dispersed due to free electrons in the ISM. In order to search for FRBs, we first need to remove the effect of dispersion. This step is at the core of every FRB search pipeline is often the most time consuming one. The DM of the FRB is not known *a-priori*, and therefore the data are dedispersed at many trial DMs, typically  $\mathcal{O}(10^2 - 10^4)$ . For each trial DM, the time delay for each channel is computed using Equation 1.5 for the higher or the lower edge of the observing band. The data in channels are then shifted accordingly and integrated to form a “dedispersed time series”.

Numerical implementations of the above come in several flavors. The most common is the brute force implementation of the above with computational complexity  $\mathcal{O}[N_T N_D N_F]$ . Here  $N_T$  is the number of time samples,  $N_F$  is the number of frequency channels, and  $N_D$  is the number of DM trials. In the so-called tree dedispersion scheme (Taylor, 1974), instead of summing over the inverse frequency squared curve, the summation is performed over a straight line. This method has the complexity of  $\mathcal{O}[N_T N_D \log_2 N_F]$  and is suitable for small bandwidths. With present-day receiver systems with bandwidths of several 100 MHz, tree dedispersion would lead to large losses in the signal. To avoid this, the algorithm is implemented over sub-bands, which are subsequently combined to form a time series. A newer method known as the Fast Dispersion Measure Transform (FDMT) implements the tree-style dedispersion method with the complexity of  $\mathcal{O}[\max\{2N_F N_T, N_T N_D \log_2 N_F\}]$  (Zackay & Ofek, 2017). Both CPU and GPU implementations of the above are now widely used for FRB searches.

#### 1.4.4 Smoothing and Normalization

The mean level of the signal varies over time during observations. This effect could be due to the nature of observations, RFI, or instrumental effects. Hence the time series data are often smoothed over a window (of few seconds) by subtracting its mean or median. The smoothed time series are often divided by the standard deviation. This is called normalization, and now the amplitude of each sample in the time series becomes the signal to noise ratio (S/N).

#### 1.4.5 Matched Filtering

Once the dedispersed time series are available, they are convolved with boxcar filters of variable widths (often upto  $\sim 100$  ms) to search for single-pulses. Pulses above a particular S/N threshold are then labeled as potential candidates.

### 1.4.6 Clustering

A single astrophysical pulse is often detected at multiple trial DMs and multiple trial filter widths. These events are clustered together using density-based clustering algorithms like “friends of friends” or DBSCAN (Huchra & Geller, 1982). The candidates are clustered in DM–time as follows. First, a radius in dimension is determined. In the time domain, the radius is often considered equal to the maximum pulse width one is searching for. For the radius in the DM domain, either absolute DM values or the trial DM index is used. The radius for the DM index is often determined empirically. All candidates within this radius would be considered as a single candidate. Now, starting with a candidate in the above described 2D space, all candidates within the radius are considered a cluster. Candidates at the edge of the cluster are determined, and the same procedure is repeated for all the edge points expanding the cluster until there are no more points to add. For each cluster, the candidate with the highest S/N is reported as the best candidate. More details and various implementation flavors can be found in Deneva et al. (2009) and Pang et al. (2018).

## 1.5 Theoretical Models for FRBs

Two areas require explanation with the limited number of FRBs discovered to date and their aggregate observed properties. First, an emission mechanism that can elucidate the millisecond burst durations, dynamic spectrum, and its structure, polarization, and energetics. Second, progenitor models explaining their population properties, sky rates, spatial and luminosity distribution. In the quest to find theories explaining the above, repeating FRBs pose additional open questions. First, do all FRBs repeat? Or are there two populations of FRBs: repeating and non-repeating FRBs? For repeating FRBs, we need mechanisms that explain  $\sim 16$  days and  $\sim 160$  day cycles seen in FRB 180916 and FRB 121102, respectively, and an evident lack of periodicity in bursts during these repeaters’ active phases.

Given the possibility that at least two types of FRBs were observed so far,

there could be different mechanisms explaining their origins and emission. Here we first discuss the emission properties and the clues they yield towards the emission mechanisms. We then detail the various proposed progenitor models for FRBs.

The high brightness temperatures ( $T_b > 10^{32}$  K) and short durations indicate coherent emission mechanisms and compact emission regions. Neutron star manifestations, like pulsars and magnetars, are coherent radio-emitters and provide an essential observational analogy. Individual shots (of widths  $\sim$ ns) bright polarized (giant) pulses can be seen from the Crab pulsar (Hankins & Eilek, 2007; Jessner et al., 2010). Such pulses will also display a multi-peaked structure and modulated dynamic spectrum similar to many observed FRBs due to the propagation effects.

Magnetars also emit radio pulses (Camilo et al., 2006); their emission can be highly energetic and erratic at various rotational phases. The radio detection of SGR 1935+2154 (Bochenek et al., 2020; The CHIME/FRB Collaboration et al., 2020a) showing MJy brightness bursts strongly indicate that magnetars are viable FRB engines.

We now discuss the various FRB progenitor models which can predict such emission properties. A catalog of FRB theories and multiple models can be found at <http://frbtheorycat.org> (Platts et al., 2019). The catalog comprises 55 different theories; the majority of them involve neutron stars due to the similarities between their observed properties and the potential to explain the involved energetics.

## 1.5.1 Neutron Star Models

### 1.5.1.1 Magnetar Flares

The central conjecture around the magnetar models is that FRBs arise from the magnetar flares. The magnetar based models themselves come in several flavors and are summarized below.

First is the so-called “low-twist” models, where magnetic field dislocations and oscillations in the neutron star surface can lead to pair cascades resulting in coherent radio emission (Wadiasingh & Timokhin, 2019; Wadiasingh et al., 2020). The model

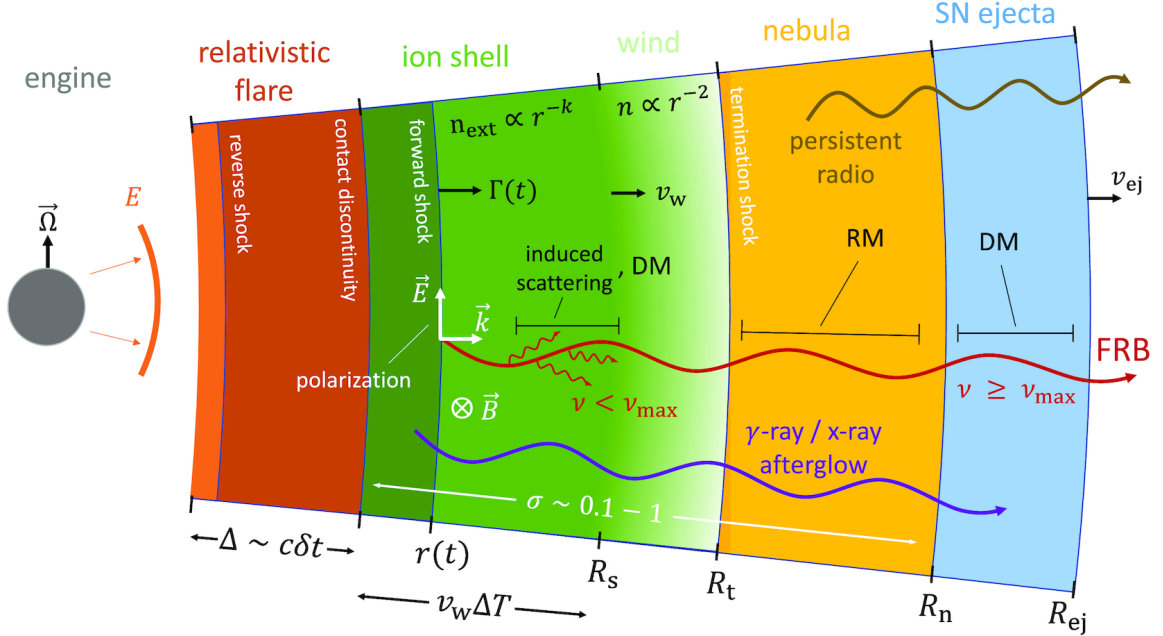


Figure 1.10: The baryonic shell model for FRBs. The FRB engines releases an ultra-relativistic shell of energy  $E$ , duration  $\delta t < 1$  ms, and radial width  $c\delta t$ . The shell collides with a mildly relativistic magnetized ion–electron shell of velocity  $v_w$ . This shell was released  $\Delta T$  ago and now has a width of  $v_w\Delta T$  and decelerates through reverse and forward shocks. The forward shocks produces the observed coherent radio emission (FRB). Figure taken from Metzger et al. (2019).

shows that the emission arrives from the magnetosphere and predicts a radius-to-frequency mapping kind of feature similar to pulsars (Cordes, 1978). For pulsars, emission takes place from a cone of magnetic field lines above the polar cap. The higher frequency emission happens closer to the neutron star surface than the lower frequency emission. The pulses emitted at a higher frequency are intrinsically narrower, and similarly, low-frequency pulses are wider.

Next are “synchrotron maser blastwave” models, first proposed by Lyubarsky (2014), where FRBs arise through coherent synchrotron maser process that is naturally produced as the ultra-relativistic flare ejecta collides with the pulsar wind nebula<sup>10</sup>. Here, the bursts are powered by tapping into a small fraction ( $\sim 1\%$ ) of the outflow’s kinetic energy.

Another variant of the same class of models is the “baryonic shell” model by

<sup>10</sup>A nebula found inside the shell of a supernova remnant, powered by winds generated by the central pulsar and usually emit in X-rays.

Beloborodov (2017); Metzger et al. (2019). Here the ultra-relativistic head of the magnetar flare collides not with the magnetar wind nebula (for more details of the magnetar wind nebula, see Lyubarsky, 2014), but instead with matter ejected from a recent, earlier flare. For more information on the same, see Figure 1.10.

Lastly, curvature radiation-based models, where the FRB is produced by curvature radiation from bunched electrons streaming along the magnetar’s magnetic field lines of the magnetar (Kumar et al., 2017).

### 1.5.1.2 Giant Pulses

Cordes & Wasserman (2016) hypothesize that fast radio bursts are associated with rare, bright pulses from extragalactic neutron stars. Neutron stars are already known to emit bright pulses with a wide range of durations, including the ms widths, as seen in FRBS. They show that the large number of NS that exist in a Hubble volume can quickly produce the inferred FRB rate even if only a single burst is produced in each neutron star’s lifetime. On the other hand, (Connor et al., 2016) presents a non-cosmological explanation for FRBs based on very young pulsars in supernova remnants. Their model predicts FRBs to have RM values between  $20\text{--}10^3 \text{ rad m}^{-2}$  and show a PA swing. As observed with FRB 121102 with its RM of  $10^5 \text{ rad m}^{-2}$  and a lack of PA swing in most FRBs with polarization information, this model now seems unlikely. Lyutikov et al. (2016) have suggested that young neutron stars of age 10–100 yrs as the sources of FRBs. Their model assumes that most of the observed DM contribution comes from the freshly ejected supernova remnant shell material. Their theory expects the distances to be  $\lesssim 300 \text{ Mpc}$  and FRBs to be mostly associated with star-forming galaxies. Recent localizations of FRBs up to  $z = 0.6$ , corresponding to a distance of 2.2 Gpc, and the large variety of star formation rates of the host galaxies for localized FRBs render this model unlikely.

### 1.5.1.3 Starquakes

Wang et al. (2018) have shown that the burst energy distribution of the repeater

FRB 121102 has a power-law form, which is similar to that of earthquakes. They fitted the energy distribution of bursts detected by Gajjar et al. (2018) with a power law of the form  $N(E) \propto E^{-\alpha}$  with  $\alpha = 2.16 \pm 0.24$ . This power law is very similar to the power-law energy distribution of earthquakes where  $N(E) \propto E^{-2}$ . Their findings suggest that the repeating FRB pulses may originate from the starquakes of a pulsar. They also show that SGRs also follow a similar distribution, and hence there may be a common connection between both of the sources.

#### 1.5.1.4 Merging and Colliding Neutron Star Models

Wang et al. (2016) propose that the magnetic interaction between double neutron stars can cause FRBs. They discuss if one neutron star is highly magnetized compared to the other, they can generate FRBs during their final inspiral. The less magnetized companion neutron star crosses the magnetosphere of the highly magnetized neutron star and produces an electromotive force. This force accelerates electrons to ultra-relativistic speeds leading to the FRB emission. They show that during the final inspiral phase, for neutron stars with magnetic field  $B \sim 10^{12}$  G, when the distance between them,  $a$  is  $28 \lesssim a \lesssim 60$  km, if the magnetic interaction extracts a small fraction ( $\lesssim 1\%$ ) of the binary orbital energy, FRBs with luminosity  $10^{40}$  ergs  $s^{-1}$  can be produced. Since this is a cataclysmic model, it does not explain the repeating FRB phenomenon.

Yamasaki et al. (2018) explain both repeating and non-repeating FRBs with general relativistic simulation showing binary neutron star mergers as a possible origin of FRBs. They simulate and show that the merger environment is polluted by dynamical ejecta, which stops the radio signal from propagating. The ejecta appears  $\sim 1$  ms after the merged star's rotation speed becomes the maximum, providing a short window for one-off FRBs. In some cases, a fraction of such mergers may leave a stable, rapidly rotating neutron star. Such objects will emit for a timescale of 1–10 yrs and may be the origin of repeating FRBs.

### 1.5.1.5 Collapsing Neutron Star Models

The so-called “blitzar” model is another example of a cataclysmic scenario that has been proposed to explain non-repeating FRBs. Blitzars (Falcke & Rezzolla, 2014) are neutron stars collapsing to form black holes and are hypothesized to produce FRB-like pulses due to the abrupt change in state when the neutron star, which was previously the source of a magnetosphere, disappears behind an event horizon. During this event, accelerated electrons from a traveling magnetic shock dissipate a significant fraction of the magnetospheric energy. Most et al. (2018) studied the gravitational collapse of a magnetized supermassive neutron star<sup>11</sup>. They found that the neutron star’s magnetic field lines will break and reconnect, leading to the propagation of waves outside the event horizon. These waves can lead to FRBs and have the energetics as that of the observed population.

### 1.5.1.6 Pulsar-orbiting Body Interactions

Mottez & Zarka (2014) argued that FRBs could originate from a pulsar-orbiting body like a planet, asteroid, or a white dwarf. In this scenario, the orbiting body is immersed in a pulsar wind, which is highly magnetized. When destabilized through plasma instabilities, these winds can be the source of strong radio sources like FRBs. The is are beamed along the pulsar-companion line. They argue that the companion’s orbital plane is likely to be very close to the pulsar’s equatorial plane. The companion’s radio emission is beamed nearly at a right angle from the rotation axis of the neutron star. For FRBs, only the companion’s emission would be seen as the pulsar’s emission is pointed orthogonal to the observer. Their theory predicts regular repeat bursts from known FRB sources with a period equal to pulsar–companion orbital period.

Geng & Huang (2015) shows that the collisions between neutron stars and asteroids/comets are a mechanism for FRBs. Their study suggests that a hot plasma fireball will form during the impact process, and coherent radiation from the thin top

---

<sup>11</sup>a neutron star with mass as the maximum mass for a non-rotating configuration



shell will lead to FRBs. Dai et al. (2016) propose a model in which highly magnetized pulsars traveling through asteroid belts of other stars. The pulsar encounters lots of asteroids in the belt, and each impact leads to electrons being torn off the asteroidal surface, accelerated to ultra-relativistic energies causing FRBs. This model seems extremely unlikely, given how little stars interact, in general.

#### 1.5.1.7 Cosmic Combs

Zhang (2017) details a unified scenario to interpret both repeating and non-repeating FRBs. The model suggests that FRBs can be produced by pulsars at cosmological distances when their magnetosphere is suddenly “combed” by a nearby, strong plasma stream. Such a plasma stream can originate from an explosion (a supernova, a gamma-ray burst, a neutron star merger event), an active galactic nucleus flare, a stellar flare from a binary companion of the pulsar, or even a tidal disruption event. This model provides a unified solution to many observed and puzzling FRB properties. For example, an AGN afterglow was detected soon after the detection of FRB 150418 (Keane et al., 2016; Williams & Berger, 2016). This model interprets the FRB emission as being combed by the AGN flare. The model also explains the repeating FRBs, such as FRB 121102, as a foreground pulsar being episodically combed by an unsteady flow from a young supernova remnant. The model predicts a detection of repeating bursts from FRB 150418 and the bursting source’s localization to the spatially coincident AGN and more detection of more detections of FRBs associated with afterglows.

### 1.5.2 Other Models

#### 1.5.2.1 Compact Object Binary Systems

Egorov & Postnov (2009) consider the impact of a supernova explosion on the magnetosphere of a neutron star in a massive binary system. The neutron star magnetosphere’s impact can give rise to a tail with a considerable store  $\sim 10^{35}$  erg of magnetic energy. The plasma instabilities can lead to the release of these energies

as coherent radiation, leading to FRBs. Kashiyama et al. (2013) proposes binary white-dwarf mergers as the source of FRBs. The proposed FRB emission would be coming from the polar region of a rapidly rotating magnetized massive white dwarf formed after the merger. Gu et al. (2016) proposes a compact system containing a magnetic white-dwarf and a neutron star with strong magnetic fields ( $B \sim 10^8$  G for the white dwarf and  $B \sim 10^{10}$  G for the neutron star) in circular orbits. When the white-dwarf fills its Roche lobe<sup>12</sup>, the mass transfer will occur from the white-dwarf to the neutron star. The accreted magnetized materials may trigger magnetic reconnection, leading to the accelerating of electrons resulting in an FRB. Their recent work has extended this theory for eccentric orbits to explain the 16 day periodicity in FRB 180916 (Gu et al., 2020). However, their model fails to explain the 160 day periodicity for FRB 121102.

### 1.5.2.2 Neutron Star–Black Hole Mergers

Mingarelli et al. (2015) suggests that in the inspiral phase of a neutron star–black hole merger, the magnetic field lines of the neutron star may thread around the black hole event horizon. Such a scenario can generate an electromagnetic pulse that would be observable as an FRB. They propose that an FRBs sub-population can be caused by this mechanism with the following distinct profile. The profile would have a double peak structure with a precursor, which can be resolved with a 0.5 ms resolution sampling interval. The precursor would be due to a rapid increase in luminosity milliseconds before coalescence. In the double peak structure, the first peak would correlate with the maximum luminosity at the merger, and the second peak from post-merger burst due to magnetic field shock. However, such a burst has not been observed yet.

---

<sup>12</sup>Roche lobe is the teardrop-shaped region near a star in which material inside the region is bound to the star by gravity.

### 1.5.2.3 Black Hole–Black Hole Mergers

Zhang (2016) postulate that during the black hole–black hole merger, if at least one of the two merging black holes carries a certain amount of charge, then their inspiral would drive a magnetic dipole. As the orbital separation decreases during the inspiral phase, the magnetic flux would increase. They derive that this charge to be of the order of  $(10^{-9} - 10^{-8}) \times \sqrt{GM}$ , where  $M$  is the mass for the black hole. An FRB can later then be produced during the final phase of the merger caused by a magnetospheric outflow.

A similar idea was proposed around the same time by Liu et al. (2016), who assumed the black hole to be a Kerr–Newman black hole (i.e., one with both spin and charge). The authors show that the closed orbits of charged particles in these objects’ magnetospheres are unstable, leading to violent reconnections. This triggers strong relativistic shock waves through the surrounding plasma to cause FRB like emission.

### 1.5.2.4 Exotic Models

Luan & Goldreich (2014) first discussed the details of advanced civilizations producing FRBs as beamed emission to communicate with us. Lingam & Loeb (2017) speculated that beams used for powering large light sails could yield FRBs. They postulate that the beam would sweep across the sail to power it. Observationally this would lead to diffraction, causing multiple peaks in the observed FRB profiles.

Cosmic strings are one-dimensional topological defects that may have been generated in the very early universe during a symmetry-breaking phase transition (Kibble, 1976). Cosmic strings generating FRBs were first postulated by Vachaspati (2008). Later, Ye et al. (2017) investigated the possibility of FRBs from superconducting cosmic strings. Given our recent associations with host galaxies for  $\sim 13$  FRBs this model seems to be ruled out.

### 1.5.3 Final Thoughts

We have outlined a range of models proposed so far that claim to explain the FRB sources. With the recent discovery of SGR 1935+2154, the flaring magnetar models seem to be a plausible explanation of the phenomena and the connection between Galactic and extragalactic FRBs. It must be noted that within the magnetar models, there are several distinct mechanisms proposed for generating the radio emission.

While the magnetar models explain FRBs' repeating nature, there are still many open questions in the field. Are there two populations of FRBs: repeating and non-repeating, or do all FRBs repeat and are limited by our telescopes' sensitivity? Kumar et al. (2019) have shown the flux distribution of repeating FRB 171019 spans two orders of magnitude; it might just be that most FRBs are repeaters. Ravi (2019) also indicates the same argument argues where they show that the cataclysmic progenitor event rate is much smaller than the number of non-repeating FRBs we have observed to date.

Localization of about a dozen FRBs has shown no preference towards a particular class of galaxies or their properties. Lastly, the discovery of periodicity in the two repeating FRBs activity windows with their periods of 16 and 160 days is yet to be explained based on a single theory. It might also be possible that there are multiple mechanisms through which FRBs (and the repeaters' periodicities) are produced. We believe that as we discover more FRBs in the future, some of these questions might be answered.

## 1.6 Thesis Outline

The thesis is organized as follows. We provide a brief introduction to deep learning in chapter 2, and develop a state-of-the-art neural network `FETCH` to automatically classify the candidates between FRBs and RFI from our searches. We discuss the details of developing and deploying a real-time FRB search pipeline along with `FETCH` to search for FRBs in a commensal fashion with the Green Bank Telescope

in chapter 3. In chapter 4, we turn the ASKAP telescope towards the Virgo cluster in search of FRBs. As we have seen, about a dozen FRBs have been localized to their host galaxies; we aim towards galaxy clusters in the hope of having an enhanced FRB rate. Lastly, we provide conclusions in chapter 5.

## Chapter 2

### A Deep-Learning Based Classifier For Fast Transient Classification

#### 2.1 Introduction

Typical FRB searches are done over thousands of DM trails and several tens of pulse width for each telescope beam. Even after clustering the events, due to the presence of RFI, the typical number of candidates range from  $10^3$  to  $10^5$  per day per beam. To parse through such a large number of candidates, astronomers use machine learning-based algorithms to reduce the number by several orders to a magnitude such that it is manageable. Deep learning has already been applied to pulsar searches (Zhu et al., 2014; Guo et al., 2017; Devine et al., 2016; Bethapudi & Desai, 2018; McFadden et al., 2018), yielding significant improvements, demonstrating their potential for use in transient searches. In this section, we discuss the details of deep learning algorithms and their implementations. A more detailed introduction for the same can be found in Goodfellow et al. (2016).

The field of machine learning encompasses algorithms where one teaches the machines to learn patterns in the data without being programmed explicitly. These algorithms then apply from what they have learned to make informed decisions or predictions. Deep Learning is a subset of machine learning, where we work with a specific set of algorithms (or models) called deep neural networks (DNNs). DNNs can be thought of as a non-linear mapping between some given input data and output data. The said non-linearity is at the core of DNNs, as it allows them to learn complex features in the input data and map it to the corresponding output. The fundamental

---

Published as Agarwal et al. (2020a)

The introduction section of this chapter is different from the published article and explains the concepts of deep learning in greater detail.

**Contributing authors:** Kshitij Aggarwal, Sarah Burke-Spolaor, Duncan R. Lorimer, Nathaniel Garver-Daniels.

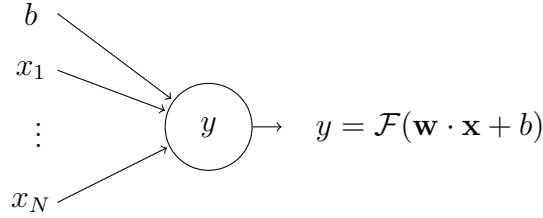


Figure 2.1: Schematic diagram of a neuron. The inputs  $x_i$  and the bias  $b$  are represented with the inward pointing arrow. Each input  $x_i$  is multiplied with a weight  $w_i$  and then passed as an argument to a non-linear activation function  $\mathcal{F}$  resulting in a single output,  $y$ , shown by the outward arrow.

unit of a DNN is called a neuron (or a perceptron). Inspired by the biological neuron cells, the DNN neuron has a set of  $N$  scalar inputs  $\mathbf{x} = (x_1, x_2, \dots, x_N)$ , and non-linear activation function ( $\mathcal{F}$ ) and maps it to a scalar output,

$$y = \mathcal{F}(\mathbf{w} \cdot \mathbf{x} + b). \quad (2.1)$$

Here,  $\mathbf{w}$  is a set of scalar weights for each input  $x_i$ , and  $b$  is a bias term. Figure 2.1 shows the schematic of a neuron used in DNNs. Some examples of non-linear activation functions, for an argument  $x$  are the hyperbolic tangent

$$\mathcal{F}(x) = \tanh x = \frac{e^x - e^{-x}}{e^x + e^{-x}}, \quad (2.2)$$

the sigmoid function (also called the logistic function),

$$\mathcal{F}(x) = \frac{e^x}{e^x + 1}, \quad (2.3)$$

and the Rectified Linear Unit (ReLU), where

$$\mathcal{F}(x) = \text{ReLU}(x) = \max\{0, x\}. \quad (2.4)$$

We then stack several neurons to form a layer. Each neuron takes the same number of inputs and produces the outputs. DNNs are composed of several such layers by connecting one layer's outputs as the input to the next layer. The layer

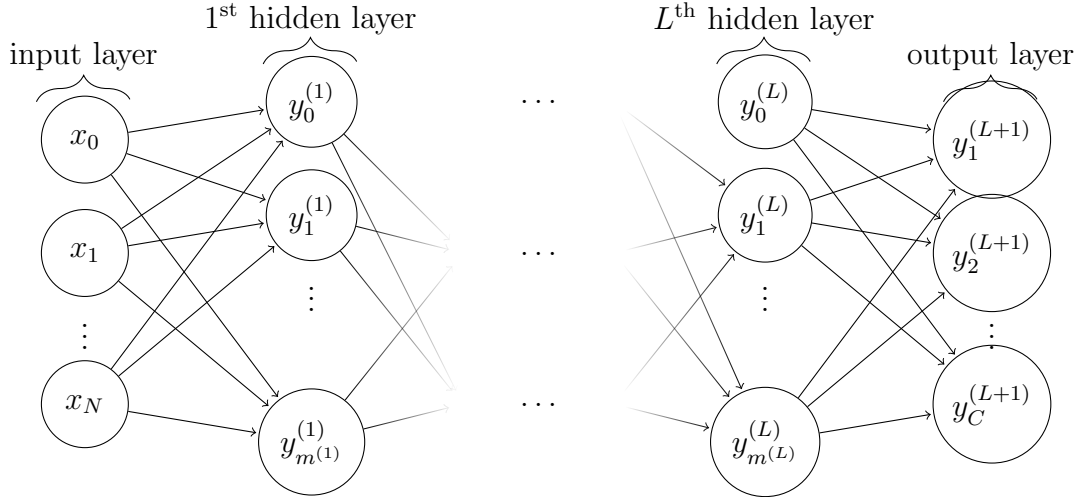


Figure 2.2: Network graph of a  $(L + 1)$ -layer perceptron with  $N$  input units and  $C$  output units. The  $l^{\text{th}}$  hidden layer contains  $m^{(l)}$  hidden units. The output of each neuron is connected to all the neurons of the following layer. The leftmost and rightmost layers are the input layer and output layers, respectively.

containing the neurons which take the data as input is called the input layer, and the last layer serving the output is termed as the output layer. All the in-between layers are termed as hidden layers. Figure 2.2 shows the schematic of such a neural network with  $L$  hidden layers. The layers where the inputs are connected to all the neurons in the layers are called fully connected layers or dense layers.

### 2.1.1 Training

Given enough labeled input data, DNNs learn model complex functions by finding the right set of weight and bias parameters for each neuron. This subsection will now discuss how we find this right set of weights for a DNN to create complex functions. This is called training a DNN where the idea is to *learn* these right set of weights such that our DNN becomes mapping between our input and output data.

The first step is to gather a large set of labeled data, i.e., some input data to know the output data. We assume that our input data  $X$  such that  $X \in \mathbb{R}^D$  is  $D$  dimensional and the output data  $Y$  such that  $Y \in \mathbb{R}^C$  is  $C$  dimensional, and we have  $N$  such examples. Here  $\mathbb{R}$  represents the set of all real numbers. The DNN is a



mapping between  $X$  and  $Y$  which is expressed in set notation as

$$\text{DNN} : \mathbb{R}^D \rightarrow \mathbb{R}^C. \quad (2.5)$$

Next we define the architecture of the DNN, i.e. we define the number of dense layers, number of neurons in each dense layer and the activation functions.

#### 2.1.1.1 Loss Function

We initiate our DNN by assigning random values of weights and biases for each neuron. We then pass the input data  $X$  and store the corresponding  $\hat{Y}$ . Given that our input data is labeled, i.e. we know the ground truth  $Y$  for each corresponding  $X$ , we now define a loss function (also called a cost function). This measures how far the output of our DNN  $\hat{Y}$  lies from the ground truth  $Y$ . The choice of cost function depends upon the task at hand, however for simplicity, here we use the mean squared error function as our loss function,

$$J(W, B) = \frac{1}{N} \sum_{i=0}^N (y_i - \hat{y}_i)^2. \quad (2.6)$$

Here,  $W$  and  $B$  correspond to the set of all weights and biases of the DNN and  $y_i, \hat{y}_i$  correspond to each example in the data set. The loss function,  $J$ , is a function of  $W$  and  $B$  as it depends on  $\hat{y}_i$  which is the output from the DNN with the corresponding weights and biases. To optimize the system, we aim to minimize the loss function by tweaking  $W$  and  $B$  for our DNN.

#### 2.1.1.2 Gradient Descent

The  $W$  and  $B$  take the form of matrices and vectors, but for simplicity we imagine them stored as a single vector that we call  $p$ . For a DNN with  $s$  such parameters, our cost function is a mapping defined by,

$$J : \mathbb{R}^s \rightarrow \mathbb{R}. \quad (2.7)$$

We now introduce a classic method in optimization called gradient descent; for more detailed treatment of the same we refer the reader to Bishop (2006). Through gradient descent we will minimize the cost function  $J$  and update the parameters  $p$ . We chose a small perturbation  $\Delta p$  and Taylor expand the cost function,

$$\begin{aligned} J(p + \Delta p) &\simeq J(p) + \sum_{i=0}^s \frac{\partial J}{\partial p_i} \Delta p_i \\ &= J(p) + \nabla J^T \Delta p. \end{aligned} \tag{2.8}$$

Here  $\nabla J$  is gradient of the loss function with respect to all the parameters  $p_i$  and  $T$  represents the transpose. Equation 2.8 motivates us to chose  $\Delta p$  such that  $\nabla J^T \Delta p$  is as negative as possible.

We now use the Cauchy–Schwarz inequality which states that for two vectors  $u, v \in \mathbb{R}^s$ ,

$$|u^T v| \leq \|u\|_2 \|v\|_2. \tag{2.9}$$

This states that the most negative value for  $\nabla J^T \Delta p$  could be  $-\nabla J^T \Delta p$  which happens when  $\Delta p = -\nabla J$ . As we used the Taylor approximation, which is only valid for small perturbations, we chose a small number  $\eta$  called the learning rate and update the parameters as,

$$p \leftarrow p - \eta \nabla J(p). \tag{2.10}$$

The method of gradient descent works iteratively by making small jumps towards the convergence.

In practice, we use stochastic gradient descent (SGD), where we shuffle the  $N$  input examples and select a small batch of  $n$  examples and perform the above. The primary reason for the above is that the input data size is usually so large that we cannot fit the whole dataset in the computer memory and compute  $J(p)$ . The method of passing a small batch of  $n$  examples forward and computing  $\hat{y}$  through

the DNN is called forward propagation. This computing gradient method for each of the parameters in the DNN and updating the weights is called backpropagation. Both of these processes are often repeated for all the examples in  $N/n$  batches. When the whole input data set is passed once, and the weights are updated for each batch, it is termed an epoch. Typically the neural networks are trained for hundreds of epochs to reach the desired level of convergence. Once the model is trained, forward propagation is used to compute outputs for a given input. This is called inference.

Gradient descent and SGD are often termed as optimizers, which compute the gradients of each parameter's cost function and update them using a learning rate. Other optimizers available use either higher-order derivatives or keep track of past derivatives for faster convergence. The choice of the number of hidden layers, number of neurons in each layer, the value of the learning rate, choice of activation function, and optimizers are often referred to as hyperparameters. These are parameters that are not learned by the neural networks and are often fixed manually. Choosing the right set of hyperparameters is driven by the task at hand is more of an art than science. Details regarding the choices of hyperparameters and its optimization are beyond the thesis's scope but can be found in Claesen & Moor (2015).

### 2.1.1.3 Data Splitting

The labeled data are divided into three sets: training, validation, and test data. The networks are trained as described above, using the training data. After each epoch, the DNNs are evaluated based on their performance on the validation data. This training process is repeated until its performance on the validation data is satisfactory. Once the DNN is trained, its performance is reported on the test data. Typically, these datasets consist of several thousand examples. Note that the validation and test datasets are never used to train the network.

#### 2.1.1.4 Bias and Variance

Let us assume we have some input data  $x$  and the corresponding output data  $y$  generated from some function  $y = f(x) + \epsilon$  and we approximate this function using a DNN. Here  $\epsilon$  is the noise with zero mean and  $\sigma^2$  variance. We can compute the expectation value ( $\mathbb{E}$ ) of the error,

$$\begin{aligned}\mathbb{E}[(y - \text{DNN}(x))^2] &= \left(\mathbb{E}[\text{DNN}(x)] - f(x)\right)^2 \\ &\quad + \mathbb{E}[(\mathbb{E}[\text{DNN}(x)] - \text{DNN}(x))^2] \\ &\quad + \sigma^2.\end{aligned}\tag{2.11}$$

Here the first term,  $\mathbb{E}[\text{DNN}(x)] - f(x)$ , is the bias in the model, this is the error in the estimation due to the assumptions in the model. The second term,  $\mathbb{E}[(\mathbb{E}[\text{DNN}(x)] - \text{DNN}(x))^2]$ , is the variance of the DNN. The last term,  $\sigma^2$ , is the noise variance as defined above.

In terms of DNNs, when the error on both the training and validation dataset is large, the DNN has high bias and low variance. This regime is called underfitting and can be corrected by making our model more complex (i.e., adding more parameters by increasing hidden layers or number of neurons in the layers). When the training error is small while the validation error is large, the DNN has memorized the training data and has failed to generalize on the validation dataset. This is where we have low bias and high variance. This regime is termed overfitting and can be corrected by either gathering more data or reducing the model complexity. There lies a sweet spot in between the two regimes, where with optimum model complexity we have a balance between trade-off of bias and variance. The trade-off implies that a model should be complex to express underlying structure in data and, at the same time, be simple enough to avoid fitting spurious patterns (Geman et al., 1992).

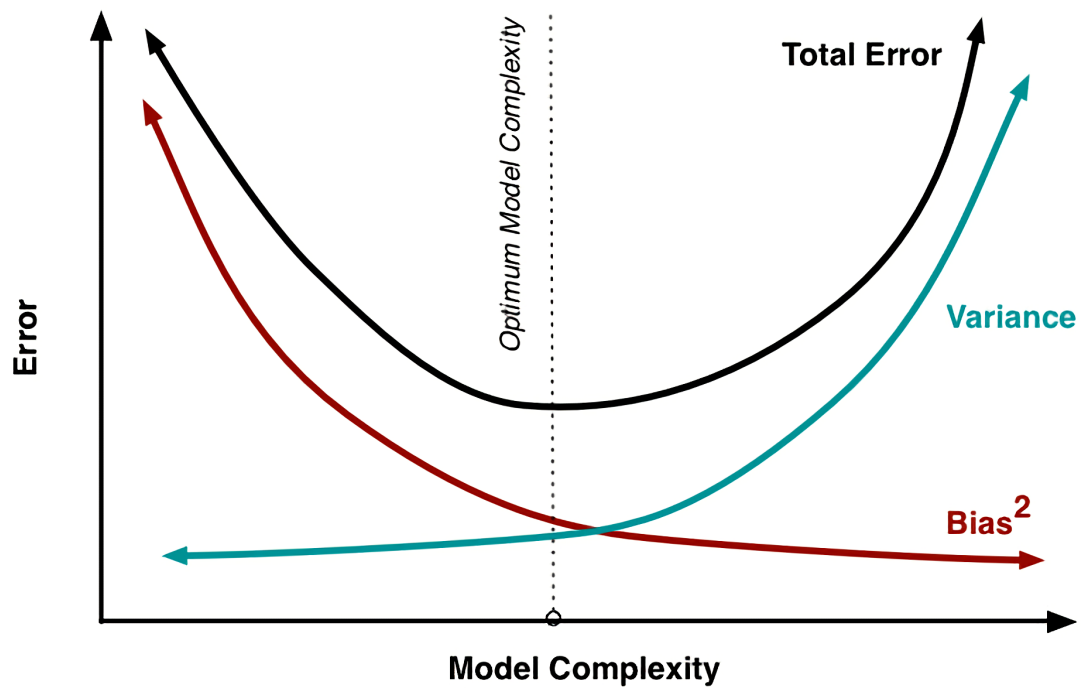


Figure 2.3: Bias–Variance Trade-off. The x-axis shows the error estimate from the DNN, and the y-axis represents the model complexity (given the number of parameters in the DNN). The brown curve shows the squared bias, the cyan curve shows the variance, and the total error is depicted using a black curve. The optimal model complexity for which there is a balance between bias vs. variance, and the total error is minimized is shown by the vertical dashed line. Figure from Fortmann-Roe (2012).

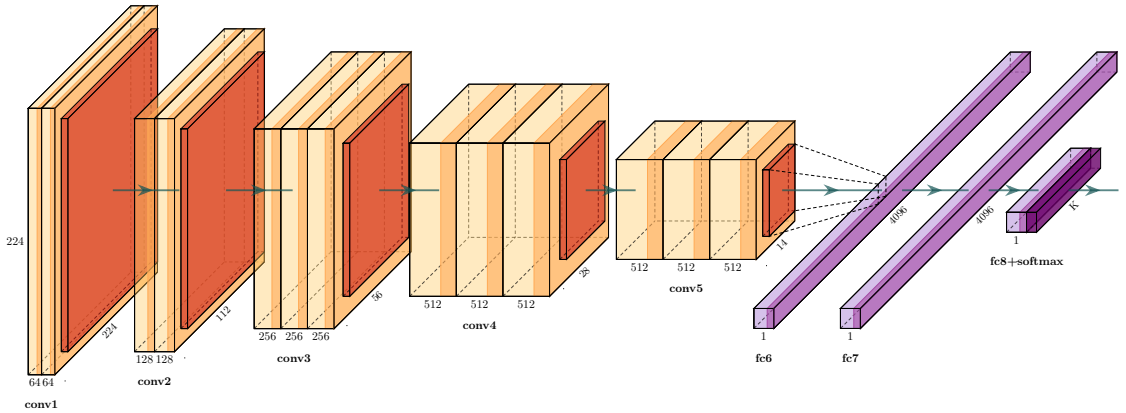


Figure 2.4: VGG16 Convolutional Neural Network. The yellow boxes represent the image sizes after the convolution with dimensions labeled on the sides. The red boxes denote the max-pooling layer, which reduces the output sizes by half in height and width. The depth of the boxes represents the number of convolutional filters. As the output image size decreases, we increase the number of convolutional filters to extract richer features. The last convolutional layer is connected to dense layers shown with purple boxes. Image generated using Iqbal (2018).

### 2.1.2 Convolutional Neural Networks

A class of DNNs used for working with images is called convolutional neural networks (CNNs). CNNs work in the same way as DNNs, but have few extra types of layers detailed below. First, the convolutional layer consists of a set of kernels which are convolved with the images to extract features out of it. Similar to DNNs, the kernel weights are learned while training. Second, the pooling layer downsamples the image by either averaging or taking maximum pixel value over the window size. The idea behind CNNs is to create convolutional kernels that extract features from images. Each convolved image is then passed through an activation function. Output images are often reduced in size by pooling operations. Repeated sets of convolutions and pooling extract meaningful features out of the images. These features are then connected to a (or several) dense layers to perform tasks like prediction or classification.

Figure 2.4 shows the VGG16 CNN (Simonyan & Zisserman, 2014). The input images are of size  $224 \times 224 \times 3$  corresponding to height, width, and color channels. The convolution kernels (brown boxes) extract features from the images, and these

are condensed using the pooling layers (red boxes). As the image size decreases, we increase the convolutional kernels' number to extract more features. Finally, the extracted features are connected to dense layers (purple boxes).

### 2.1.3 Transfer Learning

Traditionally deep learning involves building DNNs to create non-linear mappings between input and output and use large amounts of data. This paradigm breaks down when we do not have large amounts of data, as is the example of FRBs with slightly more than 100 of them discovered. In cases where the amount of data is not large enough to create models, we use transfer learning. Here, we discuss the details of this technique in the context of CNNs.

As can be seen from the Figure 2.4, we apply more and more convolutional filters as image size reduces. These convolutional filters learn to extract features, and the final dense layers map these features to the required output. The CNNs learn to extract features like simple and complex shapes and textures from the images and are often reasonably generic.

Transfer learning leverages the fact that trained networks are good at extracting features. A pre-trained CNN (a CNN trained on a different but large dataset) is taken, the top dense layers are removed, and the convolutional layers are frozen. By freezing, it means that while training, these parameters will not be updated. A new set of dense layers is attached and trained with the limited dataset. Hence the pre-trained convolutional layers extract features out of our limited dataset, and we use it only to learn a few parameters in the top dense layers.

Transfer learning has been successfully used in various domains of astronomy, e.g., identification of Supernovae Ia (Vilalta, 2018), detecting galaxy mergers (Ackermann et al., 2018) and galaxy classification schemes (Aniyan & Thorat, 2017; Pérez-Carrasco et al., 2019; Khan et al., 2019). In the upcoming sections, we will build upon the concepts of CNNs and transfer learning to build several state-of-the-art deep learning models to classify FRBs and RFI.

In this chapter, we present a set of deep neural networks developed using the

approach of transfer learning. We have utilised the state-of-the-art models trained for real-world object recognition in images to classify single pulses (eg: FRBs and pulsars) and RFI in fast-transient search data. In this work, single pulses from FRBs and pulsars are considered alike, and the models do not differentiate between the two. FRBs and pulsar single pulses can be differentiated in post processing based on their detection DM. If the DM of the pulse is greater than the Galactic DM in that line of sight, then the pulse could be of extragalactic origin (i.e. a FRB) else from a pulsar. Our networks use frequency-time and DM-time images as inputs. These networks are telescope and frequency agnostic in nature and can classify candidates in real time. We provide an open source package FETCH, which can easily be integrated into any FRB search pipeline with minimal effort. The rest of this chapter is organised in the following manner. In section 2.2 we detail the data used for training and testing the algorithms and in section 2.3 describe the methods. Results are detailed in section 2.4, followed by a discussion in section 2.5.

## 2.2 Datasets

### 2.2.1 Surveys

We used data from observations using Green Bank Telescope (GBT) and 20 m telescope both located at the Green Bank Observatory (GBO). The GBT data were recorded using commissioning test observations of GREENBURST (Surnis et al., 2019) and the pilot survey using the FLAG (Rajwade et al., 2019) instrument. The 20 m telescope data was observed using Skynet (Hosmer et al. (2013); Smith et al. (2016); Gregg et al. in prep) and GBTrans (Golpayegani et al., 2019) back-end. In order to create a uniform dataset we used HEIMDALL with the following parameters on all the above data:  $S/N \geq 8$ ,  $10 < DM < 10,000 \text{ pc cm}^{-3}$  and width  $\leq 32 \text{ ms}$ . It performs a brute force dedispersion to transform data from frequency-time to DM-time space. Each dedispersed time series is baselined to zero mean and then sliding boxcar filters of various widths are applied. The boxcar filtered time series is normalised to unit root mean squared deviation. Now, the peaks in the time series correspond



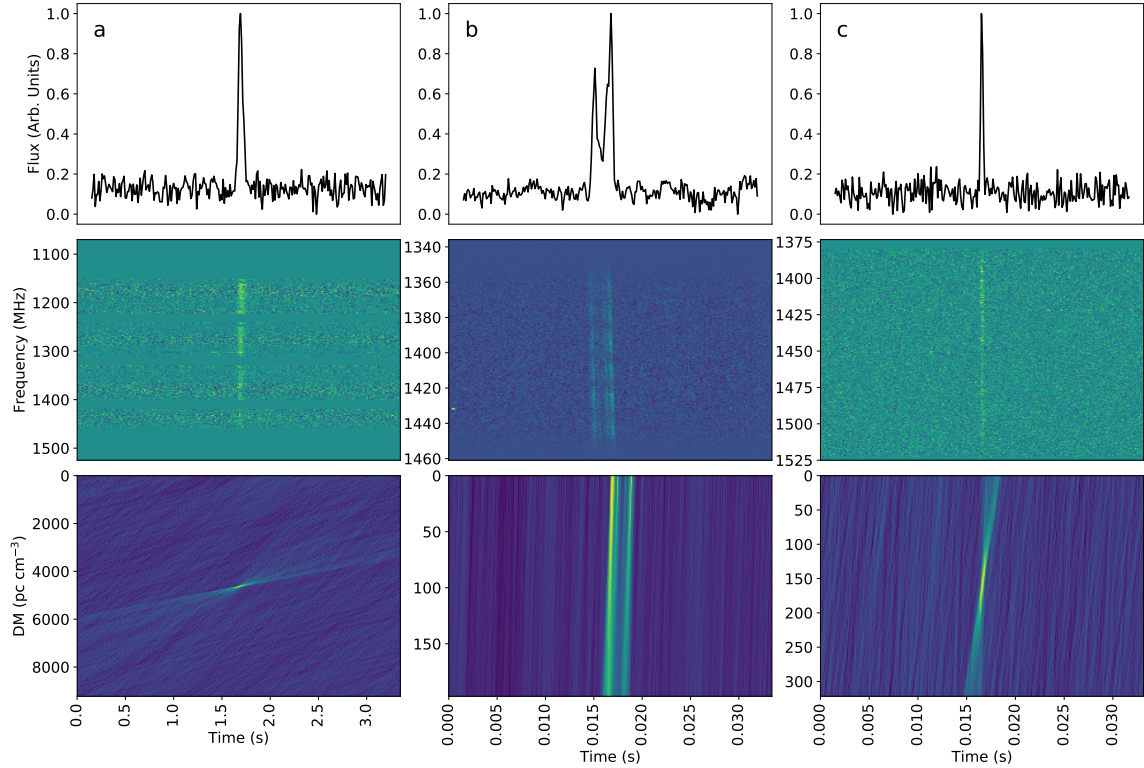


Figure 2.5: Sample images of high S/N candidates from the training and test dataset. The top row shows the time-series profile which is not included in our algorithms but is included for visual reference here. The middle row is the frequency-time image, while the bottom row is the DM-time image. Column (a) corresponds to a simulated FRB with background data from FLAG. The gaps in the frequency-time plots are due to instrumental effects. Column (b) is a real RFI candidate from the 20m telescope at the Green Bank Observatory. Column (c) is a pulsar observed using the FLAG system. Panels (a) and (c) represent the positive while panel (b) represents the negative examples in our case.

Table 2.1: Instrument (backends), sources and number of candidates (including the augmented candidates) used for training, validating and testing both frequency-time (FT) and DM-time (DMT) inputs. T+V refers to the training and the validation data, Sim FRB stands for simulated FRBs.

Instrument (back-end)	Source	T+V DMT	T+V FT	Test
<hr/>				
FLAG (FLAG)	RFI	32,720	6,000	2,790
	Sim FRB	20,000	8,500	-
	Pulsar	-	-	2,288
<hr/>				
GBT L-Band (GREENBURST)	RFI	-	6,000	2,170
	Sim FRB	20,000	8,500	-
	Pulsar	-	-	1,376
<hr/>				
Green Bank 20m (Skynet) (GBTrans)	RFI	9,854	8,000	2,359
	Pulsar	-	3,000	3,000
<hr/>				
Total	FRB	40,000	20,000	6,664
	RFI	42,574	20,000	7,319
<hr/>				

to S/N, and a threshold is used to select the candidates. The generated candidates were manually labelled. From the above, we used 24,947 RFI candidates, 6000 Crab giant pulses from GBTrans, 1,931 and 357 pulses from B1933+16 and B2011+32, respectively, observed using FLAG. We also used 1,376 pulses from PSR B0740–28, detected with GREENBURST (see subsection 2.2.3 for details).

While the above pulsar detections partly served as a training data set for astrophysical pulses, we also wished to train on signals that better represent FRBs: that is, typically isolated from other pulses in the data, and spanning a larger range in widths and DMs. Thus, to acquire a training data set that included such pulses, we injected simulated transients into around 2.4 h of data taken with GREENBURST (for MJD 58320) and 5.7 h from FLAG (between MJD 58146–58153). These data were selected randomly from various observations to ensure that they cover the broad variety of instrumental effects that typically impact observations. Examples of such effects are bandpass variations, nulling of part of the bandpass due to a malfunctioning subset of the telescope processing back-end, packet loss and low-level RFI.

Table 2.2: Parameter Distribution for Simulated FRBs

Parameter	Distribution	Range
Fluence (Jy ms)	Log-normal	$\mu = 3.5, \sigma = 1$
DM (pc cm <sup>-3</sup> )	Uniform	50, 5000
Width (ms)	Uniform	0.5, 50
Spectral Index	Uniform	-4, 4
Scattering Timescale	Uniform	0, Width

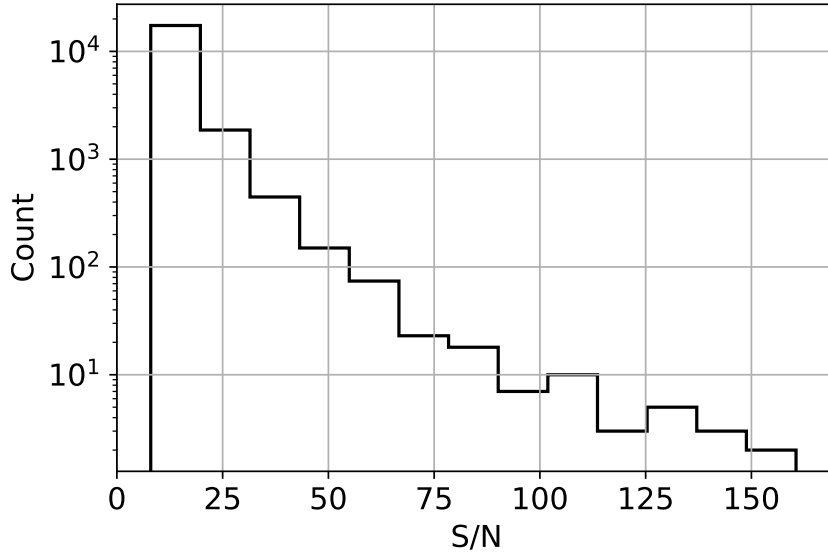


Figure 2.6: Distribution of S/N of the simulated FRBs.

### 2.2.2 Simulating and Injecting FRBs

We chose the parameters of simulated FRB candidates from a predefined distribution (see Table 2.2). Each pulse is then injected on randomly selected background data, as described above. After the injection, data were normalised to a median of zero and unit standard deviation. We then discard the candidates with an S/N less than 8. These codes to generate simulated FRBs were run on Super Computing System (Spruce Knob) at West Virginia University. Fig. 2.6 represents the S/N distribution of the injected candidates after discarding the low-S/N events.

### 2.2.3 Train and Test Datasets

Deep learning models, irrespective of their architecture, are heavily influenced by the size and quality of the dataset which is used to train them. For a binary classification application like ours (i.e. “RFI” vs. “FRB”), it is advisable to have balanced training dataset, i.e. nearly equal number of FRB and RFI candidates (Buda et al., 2018). Also, within each class, it is necessary to make sure that the features which are of interest (eg: vertical signal feature in the dedispersed frequency-time images, and bow-tie shape in DM-time images) are dominant in the images. We build upon the methods described in Zhang et al. (2018) and Connor & van Leeuwen (2018) where the authors create a balanced train and test datasets using real RFI and simulated FRBs for training and testing their networks.

Table 2.1 provides the details of the candidates (including the augmented ones) in the datasets used for the Frequency-time (FT) and DM-time (DMT) models. We used 32,720 RFI candidates from FLAG and 9,854 RFI candidates from the Skynet backend towards the RFI examples to train the DMT models. For the same models, we used 20,000 simulated FRBs generated from GREENBURST and FLAG backends each. For training the FT models, we used 6000 RFI candidates from FLAG backend (randomly chosen from the original 32,720 RFI candidates), 6,000 RFI candidates from GREENBURST backend and 8,000 RFI candidates from Skynet backend. We used 8,500 simulated FRB candidates for both GREENBURST and FLAG backend each (randomly chosen from the original 20,000). We also used 3,000 giant pulses from Crab pulsar from GBTrans backend in this dataset used to train FT models. The test set was curated independently using separate observation scans with 2,790, 2170 and 2,359 RFI examples from FLAG, GREENBURST and Skynet backends respectively. Instead of using simulated FRBs, the test set contains pulsar single pulses which are listed as follows. From the FLAG backend, we used 357 and 1,931 single pulses from PSR B2011+38 and PSR 1933+16 respectively. From the GREENBURST backend, we used 1,376 single pulses of PSR B0740-28 and lastly, we used 3,000 Crab giant pulses from GBTrans backend.

The frequency-time images are dependent on the bandpass of individual backends, we balanced the number of candidates from each back-end as well. These variations can be seen from Fig. 4 in Rajwade et al. (2019) and Fig. 2 in Surnis et al. (2019). In the DM-time images, as the frequencies are scrunched, the image is independent of such effects therefore we did not opt for any such balancing for it. On the other hand, FT images depend on the frequency structure of the data. Therefore, we made sure to use an equal number of RFI and simulated FRBs from GREENBURST and FLAG backends each. This was done to balance the features present in the individual backends. Due to this, the datasets for FT and DMT were not identical. We used the FT training dataset to train the combined models.

We split the training data randomly into 85% training and 15% validation sets. The random split of the data is justified because the data were taken from different backends on different days when the telescope was looking at different parts of the sky. These backends have different numbers of beams, bandwidth, observing frequency and time resolution. The spectrogram data in the images used for training the models are of the order of 10 seconds while the observations were spread across six months. As the two time scales differ by several orders of magnitude and the telescope was pointing at different locations with different backends at different times, it is highly unlikely that any two observations would be similar or correlated. The random shuffle of data makes sure that both the training and the validation data are drawn from the same distribution of features in the images.

The test dataset was used to evaluate and compare the performance of the combined models. It consists of real data, where we have used RFI and pulsars from different back-ends (see Table 2.1). The dataset was sampled independently i.e the observation scans were different from those for training and validation data. Due to the limited number of pulsar candidates, we use a small number of those in training/validation set while keeping most of them for the test set. Furthermore, in subsection 2.4.2 we detail a real-world test data set which includes data from the FRB searches from three telescopes: ASKAP, PARKES and GBT.

## 2.2.4 Data Augmentation

To expand on smaller data sets, and make the networks more robust, training data can be augmented in several ways to increase the number of candidates in your training data set. In the example of training images to recognize cats, one would expect a cat to be identified as such if it were facing rightward or leftward. Thus, the same image can be used twice in the training data (once as is and once inverted horizontally). Depending on the data and nature of the candidates (in particular its uniquely identifying features), this technique needs to be used with caution. For instance, one cannot typically horizontally invert FRB candidates because dispersion and scattering are not symmetric effects in time. However, we discuss here several aspects of this technique which can be applied to the radio transient data in the realm of RFI. We used both the techniques listed below to double the number of RFI candidates in each dataset. The number of candidates mentioned in Table 2.1 include augmented candidates.

### 2.2.4.1 Frequency-Time Flip

In de-dispersed data, the frequency-time image can be flipped along the time axis. This is because de-dispersion removes the dispersion asymmetry from the data. However, due to the presence of scattering, flipping along the frequency axis would not be advisable.

### 2.2.4.2 DM-Time Flip

DM-time data can be flipped along both time and DM axis. This would preserve the orientation of the bow-tie. Although, a DM-time flip is not physically meaningful, it is a useful technique from a computer vision point of view.

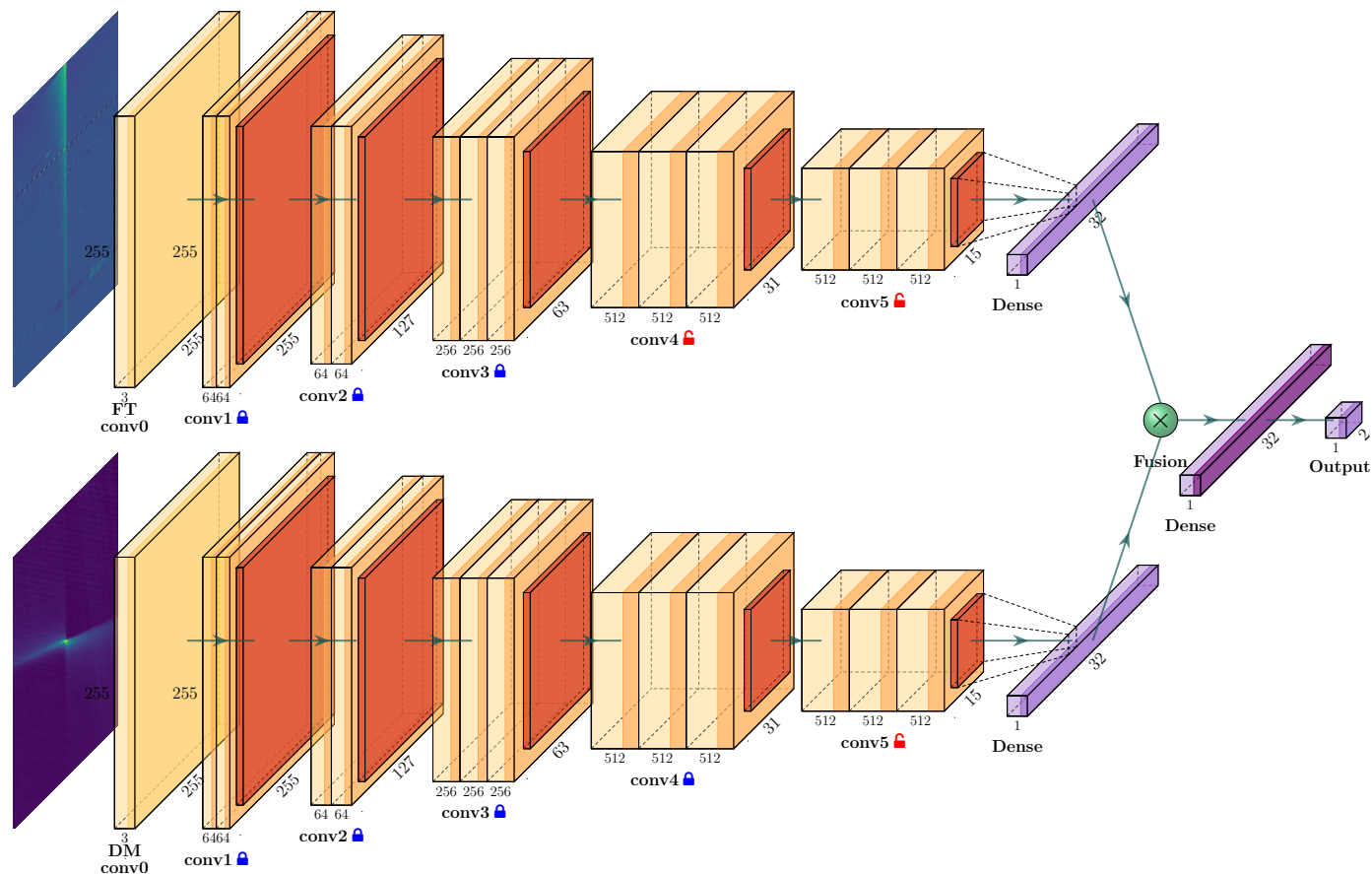


Figure 2.7: The figure shows a sample network architecture. The two inputs are the frequency-time and DM-time images. For simplicity, we have used the VGG16 (Simonyan & Zisserman, 2014) model to describe the architecture. The yellow boxes show the convolutional outputs and are labelled with output sizes. The brown edges represent the ReLU activation. The orange boxes depict the pooling layer. The dense layers are displayed in violet. The green ball represents the element-wise product of the two dense layers. The second last dense layer has a softmax activation function demonstrated by the darker coloured edge. The blue lock symbol represents the frozen layers while the red unlock symbol shows the unfrozen (i.e. trainable) layers. The arrows show the network connections. The figure is generated using Iqbal (2018).

## 2.3 Methods

In this section, we describe the network architectures, the data used for training and testing these networks, and a standardisation procedure. This “standardisation” refers to reshaping all input data to have the same size and shape. For instance, all spectrograms must have the same number of frequency channels and time samples to use in our trained algorithm. Following Connor & van Leeuwen (2018), we use frequency-time spectrograms and DM-time images as an input to our network. We train a different CNN for each input case and then combine the two (see §4). In contrast, we do not use time-series data, as that information is already contained in frequency-time images. We have also opted not to use sky-dependent (e.g. multi-beam) signal-to-noise as an input, because not all telescopes have this information available. Furthermore, we consider it a feasible alternative for sky-distributed RFI detections to be mitigated based on simple coincident rejection techniques, as multiple pipelines have done previously (Burke-Spolaor et al., 2011; Champion et al., 2016; Shannon et al., 2018; Amiri et al., 2019).

### 2.3.1 Input Data Standardization

We standardise our input data to make the algorithm agnostic to observing frequency and choice of the telescope. We use de-dispersed data in the frequency-time spectrogram as an input. Once de-dispersed, the data are independent of the original candidate DM and observational frequency (apart from any potential intrinsic frequency-dependent FRB properties, which may remain). We bin the time axis such that the candidate pulse profile lies between 1–4 bins of the origin. As a result, we are weakly sensitive to different sampling times on various telescope back-ends. This also maximises the S/N by condensing the pulse to a few bins. The frequency-time image is then re-sized to  $256 \times 256$  pixels (or bins) by averaging the frequency axis and trimming out the extra pixels. The choice of 256 frequency bins was made to preserve the frequency modulation of the recently reported FRBs (Shannon et al., 2018; Amiri et al., 2019; Chatterjee et al., 2017). To reduce the effects of bandpass



variation, we fit out a linear trend along the frequency axis. While a pulse with S/N of 10 spread over 256 channels might not be visible to the human eye our networks can still identify them.

DM-time images are created by scrunching (averaging along frequency axis) the frequency-time after de-dispersing it at different DMs. We chose the DM range from zero to twice the DM of the candidate, spread over 256 steps. The time axis was binned and cropped as explained above. A typical DM-time image of a real event looks like a bow-tie centered around a non-zero DM value. The edges of the bow-tie shape are bounded by the extent of the pulse profile. The angle between them is dependent on DM, the width of the candidate and the observing bandwidth. The area filled between these lines is governed by the spectra of the FRB. Fig. 2.5 shows an example of the input images.

### 2.3.2 Network Architecture

We use `KERAS` (Chollet et al., 2015) with the `TENSORFLOW` (Abadi et al., 2015) back-end to develop our models for both frequency-time and DM-time inputs separately. `KERAS` provides the following networks with weights trained on Imagenet Deng et al. (2009). For consistency with the literature, we adopt the following acronyms:

- `XCEPTION` (Chollet, 2016)
- `VGG16`, `VGG19` (Simonyan & Zisserman, 2014)
- `RESNET50` (He et al., 2016)
- `DENSENET121`, `DENSENET169`, `DENSENET201` (Huang et al., 2017)
- `INCEPTIONV3` (Szegedy et al., 2016)
- `INCEPTIONRESNETV2` (Szegedy et al., 2017)
- `MOBILENET` (Howard et al., 2017)
- `MOBILENETV2` (Sandler et al., 2018)

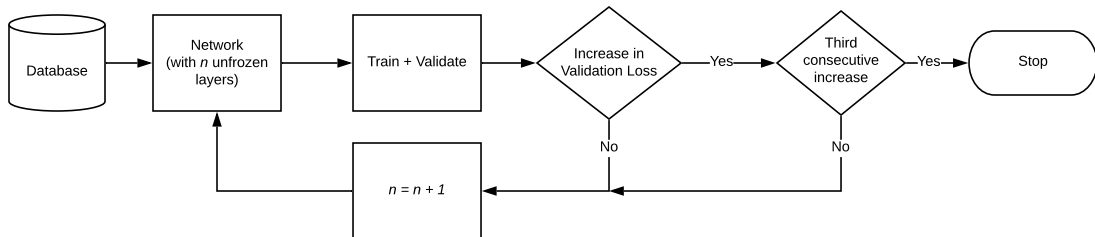


Figure 2.8: Flow chart explaining the training procedure followed for each frequency-time and DM-time model (see subsection 2.3.2.1 for details). Here,  $n$  corresponds to the number of unfrozen layers in the model, and the database corresponds to the training and validation data. We begin the training process at  $n = 0$ , and its validation loss is recorded. We then increment  $n$ , i.e. unfreeze a layer and train the model. This process continues until the validation loss increases for three consecutive values of  $n$ . The model with the least validation loss is chosen for subsequent use.

Fig. 2.7 shows a sample architecture using VGG16 for both frequency-time and DM-time models. All the above models expect three colour-channel (i.e. RGB) images. In order to make our input data compatible with these models, we apply three ( $2 \times 2$ ) convolutional filters with a Rectified Linear Unit (ReLU) activation function. This is denoted as FT conv0 and DM conv0 in Fig. 2.7, where FT corresponds to frequency-time, and DMT to DM-time. Note that both the FT and DMT images were scaled to zero median and unit standard deviation. The output is then attached to the above-stated models, and the top classification layer is replaced with a dense layer with two units and a softmax activation function. The softmax function takes an  $N$ -dimensional vector with elements  $a_j$  as the input. The corresponding element-wise operation

$$S_j = \frac{e^{a_j}}{\sum_{k=1}^N a_k} \quad \forall j \in 1 \dots N \quad (2.12)$$

makes sure that the output probabilities always sum to unity.

### 2.3.2.1 Training

For training, we use transfer learning in the following manner. The networks with Imagenet weights are frozen, and the rest of the weights are trained and validated. The frozen weights are not modified during backward propagation. This is

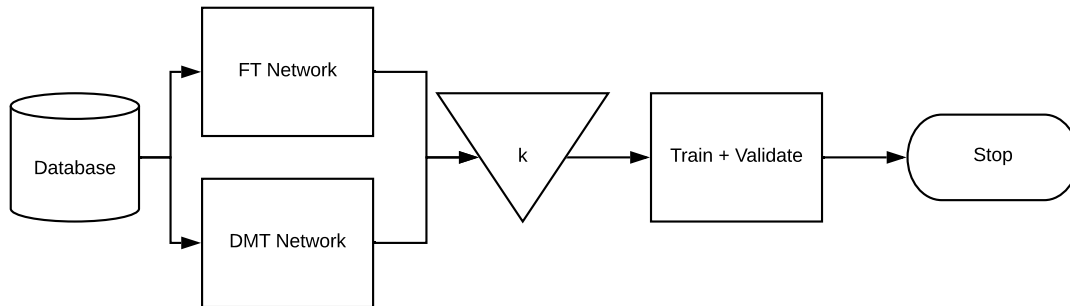


Figure 2.9: Flow chart explaining the training procedure followed after frequency-time and DM-time models were fused. Here  $k$  corresponds to the fusion parameter. As explained in subsection 2.3.2.2, each pair of FT and DMT network, was fused using a dense layer with  $k$  units. The database corresponds to the training and validation data.

done because the trained models are already good at feature extraction. The training continues until the validation loss stops decreasing for at least three consecutive epochs. At this point, the model is considered to be trained. In order to tune our models further, we start unfreezing the top layers one by one and repeat the above procedure to train the network. We denote  $n$  as the number of layers unfrozen. The unfreeze–train process continues till the validation loss stops decreasing for at least three trainable layers and the model configuration with least validation loss is selected (see Figure 2.8). To prevent the network from learning undesirable background features and overfitting, we add Gaussian noise with zero mean and unit standard deviation to the input data at each epoch. See Jiang et al. (2009) for a detailed analysis and discussion of the addition of white noise while training. The whole procedure is repeated separately for frequency-time and DM-time inputs.

For training, we use the Adaptive Moments (Adam) optimiser (Kingma & Ba, 2015) with a binary cross-entropy cost function. The learning rate for Adam is set to be the same as for the Imagenet training. The data are split randomly into train and validate sets, which encompass 85 and 15% of the data, respectively.

### 2.3.2.2 Network Fusion

Once both DM-time and frequency-time models are trained, we must combine them to get a more robust network for FRB–RFI classification. Network combination can be performed in many ways. The most common approach is to concatenate the feature extraction layer and add a classification layer. However, the layer concatenation approach did not work for us, as it over-fitted our data.

Instead, we use the multiplicative fusion approach to fuse the two networks (see Park et al. (2016) and references therein). For each DM-time and frequency-time model, the top classification layer is removed. A new dense layer with  $k$  units is attached to both the models. An element-wise product is then taken, followed by a classification layer with two units with a softmax activation function (softmax is described above in subsection 2.3.2). This method allows us to combine both models with a single hyperparameter  $k$ , and also acts as a regularizer while training. We keep the previously trained layers unfrozen, and both the models learn simultaneously while training (see Figure 2.9).

As an example, when we combined our top models for both DM-time and frequency-time, VGG16 and VGG19, respectively, using concatenation, the combined model yielded training accuracy of 99.1% while the validation accuracy was 77.6%. This is a classic case of overfitting. In contrast, combining these models using multiplicative fusion with  $k = 128$  lead to a training and validation accuracy of 99.9% and 99.8% respectively.

The training procedure detailed above is executed for all model combinations for five values of  $k = (2^5, 2^6, 2^7, 2^8, 2^9)$ . Based on the performance of the models with the above  $k$  values, some intermediate values of  $k$  were also used in some cases. We trained our models on a Tesla P100 GPU at the XSEDE Pittsburgh Supercomputing Center. Training frequency-time and DM-time models for  $\sim 10$  epochs usually completed within 1 h. Training the fused networks for  $\sim 10$  epochs took about 1.5 h.

Table 2.3: Top-5 models for frequency-time (top) and DM-time (bottom) with their respective validation accuracies (Val Acc). Number of unfrozen layers ( $n$ ) is written in parenthesis for each model

FT Model	Val Acc (%)
VGG19 (4)	99.78
VGG16 (4)	99.40
DENSENET169 (11)	95.40
DENSENET201 (7)	94.05
DENSENET121 (4)	88.23
DMT Model	Val Acc (%)
VGG16 (2)	99.92
XCEPTION (21)	99.87
VGG19 (0)	99.73
INCEPTIONV3 (31)	99.46
INCEPTIONRESNETV2 (34)	99.35

### 2.3.3 Metrics

Various metrics could be employed for evaluating the performance of the models. Our primary goal is to have these algorithms accurately identify FRBs while minimising the presentation of RFI as a good FRB candidate. We have used accuracy, precision, recall, and fscore to eliminate models, and decide what models rank highly in this regard. *Accuracy* is the ratio of the number of correct predictions (of FRBs and RFIs) to the total number of predictions. *Precision* is the number of FRBs correctly labelled divided by all the candidates labelled as FRBs. *Recall* is the fraction of FRBs correctly classified as FRBs. *Fscore* is the harmonic mean of precision and recall and is usually used to find a balance between the two. Single pulses from FRBs and pulsars are considered “real” or “positive” while RFI is considered “bogus” or “negative” for the calculation of metrics. All metrics were computed for training and validation dataset corresponding to each model iteration. This was also used to eliminate models which suffered from overfitting (e.g. ResNet) and underfitting (e.g. MobileNets).

## 2.4 Results

### 2.4.1 Model Selection

As mentioned in the previous sections, we trained many different models (see subsection 2.3.2) individually on DM-time images, and frequency-time images. For each model, a hyperparameter  $n$  (i.e., the number of trainable layers) was also found. We used *validation accuracy* to decide the top-five models each for the two inputs, as this metric fulfills the most fundamental requirement: that as few as possible candidates are wrongfully classified. The metrics for these five models are given in Table 2.3.

Twenty-five pairs of models were formed using the top-five models selected for each input. Each such pair was combined using five different values of hyperparameter  $k$ , as explained in §2.3.2.2. Additional  $k$  values between the given range were also used in some cases, if the model combination was observed to perform well. Models were then filtered by their test metrics i.e accuracy, recall and fscore  $> 99.5\%$ . Of the model combinations with different  $k$  values, only the one with highest fscore was retained. 11 models passed this filter criterion, and are henceforth referred to as top-11 models. These top-11 models are given in Table 2.4. Models in Table 2.4 have been sorted by the accuracy on test data. As can be observed, model A is the best performing model with accuracy, recall and fscore  $\sim 99.9\%$ .

#### 2.4.1.1 Two-Phase Training Approach

In this analysis, we have opted for a two-phase training approach. The first phase involved training the frequency-time and DM-time models separately. In the second phase, we combine the models using multiplicative fusion and train them. This approach was taken to reduce the number of models to be trained.

In the case of a single-phase approach, one would start with 11 model architectures for both frequency-time and DM-time models. Combining them with five values of fusion hyperparameter  $k$ , would result in 605 combined models. Then for

each model, one would unfreeze  $n_1$  and  $n_2$  number of layers in frequency-time and DM-time model respectively. If on an average, 10 layers were unfrozen for both the models (i.e.  $n_1 = n_2 = 10$ ), it would result in 60,500 models, each of which would have to be trained separately.

In contrast, the two-phase approach would consist of training 110 models for both frequency-time and DM-time each in the first phase. In the second phase, combining top-5 frequency-time and DM-time models with five values of hyperparameter  $k$  would lead to 125 models to be trained. As a result, one would train 345 models with this approach, which is much less than the number of models to be trained using single-phase approach.

Table 2.4: Top-11 models with their corresponding metrics on test data. Again, number of unfrozen layers ( $n$ ) is written in parenthesis for each model.  $k$  is the fusion hyperparameter. FT, DMT corresponds to frequency-time and DM-time.

Label	FT Model	DMT Model	$k$	Accuracy (%)	Recall (%)	Fscore (%)
a	DENSENET121 (4)	XCEPTION (21)	256	99.88	99.92	99.87
b	DENSENET121 (4)	VGG16 (2)	32	99.86	99.92	99.85
c	DENSENET169 (11)	XCEPTION (21)	112	99.86	99.78	99.85
d	DENSENET201 (7)	XCEPTION (21)	32	99.86	99.78	99.85
e	VGG19 (4)	XCEPTION (21)	128	99.85	99.75	99.84
f	DENSENET169 (11)	VGG16 (2)	512	99.81	99.7	99.79
g	VGG19 (4)	VGG16 (2)	128	99.79	99.59	99.77
h	DENSENET201 (7)	INCEPTIONRESNETV2 (34)	160	99.76	99.72	99.74
i	DENSENET201 (7)	VGG16 (2)	32	99.75	99.59	99.73
j	VGG19 (4)	INCEPTIONRESNETV2 (34)	512	99.68	99.59	99.65
k	DENSENET121 (4)	INCEPTIONV3 (31)	64	99.66	99.62	99.63



## 2.4.2 Evaluating Performance on Independent Data (and Actual FRB Detections)

We evaluated the performance of our top-11 models on independent FRB data. This serves a two-fold purpose. First, it would demonstrate how well our models perform on real FRBs, as they were trained on pulsars and simulated FRBs. Second, this would show how well the models would generalise to data from other telescopes. Given that each telescope has its unique instrumental effects and RFI environment, it is imperative to do such tests to gain confidence in the performance of the models in potentially vastly different RFI environments. This can be considered as a real world test dataset as it is representative of typical FRB-searches.

### 2.4.2.1 Data

We used the FRB data from ASKAP (Shannon et al., 2018), Parkes (5 from (Champion et al., 2016), FRB 110220 (Thornton et al., 2013), FRB 150215 (Petroff et al., 2016) and FRB 140514 (Petroff et al., 2014)) and FRB 121102 data from Breakthrough Listen (Gajjar et al., 2018; Zhang et al., 2018). We used only 8 out of 22 Parkes FRBs, as the rest of them had 96 frequency channels. These datasets were fed to the transient detection pipeline, HEIMDALL, which uses sliding boxcar filters to search for transients at various widths and S/N thresholds and is in standard use in multiple FRB search pipelines around the world. Candidates which meet the following search criterion were produced:  $S/N \geq 8$ ,  $10 < DM < 10000 \text{ pc cm}^{-3}$ , width  $< 32 \text{ ms}$ . The candidates thus produced were inspected visually.

Out of the 10,672 candidates found from ASKAP data, we selected the 33 FRB detections (20 unique FRBs, a few detected in multiple beams) reported in Shannon et al. (2018). The remainder of the 10,639 candidates were manually parsed through for verification and labelled as RFI. From Parkes data, we obtained 486 candidates (8 we marked as FRBs, 478 as RFI). From Breakthrough Listen data, we obtained 15 pulses of FRB 121102, and the remaining 652 candidates were labelled as RFI.

Table 2.5: Precision and recall values on real FRB data from ASKAP, Parkes and Breakthrough Listen (BL) backend. Here R and P correspond to recall and precision respectively.

Label	ASKAP		Parkes		BL 121102	
	R	P	R	P	R	P
a	1.00	0.94	1.00	1.00	0.93	1.00
b	0.85	0.85	1.00	0.14	1.00	0.94
c	1.00	0.67	1.00	0.57	1.00	1.00
d	1.00	0.73	1.00	0.22	1.00	1.00
e	1.00	0.67	1.00	0.53	0.93	1.00
f	1.00	0.94	1.00	0.89	0.93	1.00
g	0.88	0.97	1.00	0.44	0.60	0.38
h	1.00	0.43	1.00	0.17	0.93	0.74
i	1.00	0.69	1.00	0.13	0.93	0.93
j	1.00	0.50	1.00	0.73	0.87	0.22
k	1.00	0.82	1.00	0.10	1.00	0.94

#### 2.4.2.2 Model Performance

In table 2.6, we report the number of correct classifications of FRBs and incorrect classifications of RFI. All of the models were able to classify all the ASKAP and Parkes FRBs except model B,G. While for FRB 121102, four models were able to classify all the pulses correctly. Moreover, the rate of mislabelling RFI as FRB was relatively low, as evident in the table. The precision and recall values for the same are reported in table 2.5.

Note that these models were not trained on data from any of these back-ends, which is a testament to the instrument-agnostic capabilities of our trained algorithm, which appears to be relatively transferable despite the lack of re-training. Performance can be further improved by training the models with a few thousand candidates from any new back-end. This procedure is detailed in subsection 2.5.4.

The satisfactory performance of our models on data from these different back-ends provides reasonable confidence that they have learned features about RFI and FRBs that are sufficiently general such that they can distinguish an FRB from RFI, using only the frequency-time and DM-time images.

Table 2.6: Results of model evaluation on Real FRB data from ASKAP, Parkes and Breakthrough Listen (BL) backend. Total number of candidates in each case is written alongside the title. Numbers in the bold represent the best performing models for the corresponding cases.

Label	ASKAP FRBs (/33)	Mislabelled AKSAP RFI (/10639)	Parkes FRBs (/8)	Mislabelled Parkes RFI (/478)	BL 121102 (/15)	Mislabelled BL RFI (/652)
a	<b>33</b>	2	<b>8</b>	<b>0</b>	14	<b>0</b>
b	28	5	<b>8</b>	48	<b>15</b>	1
c	<b>33</b>	16	<b>8</b>	6	<b>15</b>	<b>0</b>
d	<b>33</b>	12	<b>8</b>	29	<b>15</b>	<b>0</b>
e	<b>33</b>	16	<b>8</b>	7	14	<b>0</b>
f	<b>33</b>	2	<b>8</b>	1	14	<b>0</b>
g	29	<b>1</b>	<b>8</b>	10	9	15
h	<b>33</b>	43	<b>8</b>	40	14	5
i	<b>33</b>	15	<b>8</b>	52	14	1
j	<b>33</b>	33	<b>8</b>	3	13	45
k	<b>33</b>	7	<b>8</b>	70	<b>15</b>	1

## 2.5 Discussion

### 2.5.1 Inference Speeds and Size

We measure the inference speed of our models on NVIDIA GTX-1070 and NVIDIA Titan-Xp using our test data set with a batch size of 64. For both of the GPUs, the mean times were  $12 \pm 1$  ms and  $6.7 \pm 0.9$  ms respectively (see Fig. 2.10). Therefore, for a conservative time of  $\sim 20$  ms per candidate, all of our top-11 models can work in real time if the candidate rate does not exceed  $\sim 10^8$  per hour. Most GPU accelerated pipelines use clustering algorithms to cluster candidates in a multi-dimensional parameter space (e.g., DM, box-car width, arrival time). As a result, the number of candidates per hour is significantly smaller. As an example, using HEIMDALL on the  $\sim 700$  hours of full scan ASKAP data from Shannon et al. (2018), we obtained  $\sim 10^4$  candidates. Therefore any of our top-11 models could be used in a commensal pipeline for real-time classification of the candidates and triggers for multi-frequency follow-ups. However, it should be noted that ASKAP is in a radio-quiet zone. Therefore the number of RFI candidates would be smaller.

Fig. 2.10 can also be used to compare the sizes of individual models. The size of a model is proportional to the number of parameters in the model. Hence larger models tend to run slower. While the above is generally true, it should be noted that the model architecture itself plays an essential role in the inference speed.

### 2.5.2 Input Shapes

For training as well as testing, we have used  $256 \times 256$  pixel images for both Frequency-Time and DM-Time. As explained in subsection 2.3.1, to achieve that size, we applied a standardisation procedure to both images. In order to test our models for various input sizes, we used high S/N pulsar candidates from GREENBURST and binned the frequency axis to different sizes (4096, 2048, 1024, 512). We also added Gaussian noise to the data to artificially reduce its S/N, such that for each size we have a uniform distribution of S/N between 8 and 40 with  $\sim 650$  candidates.

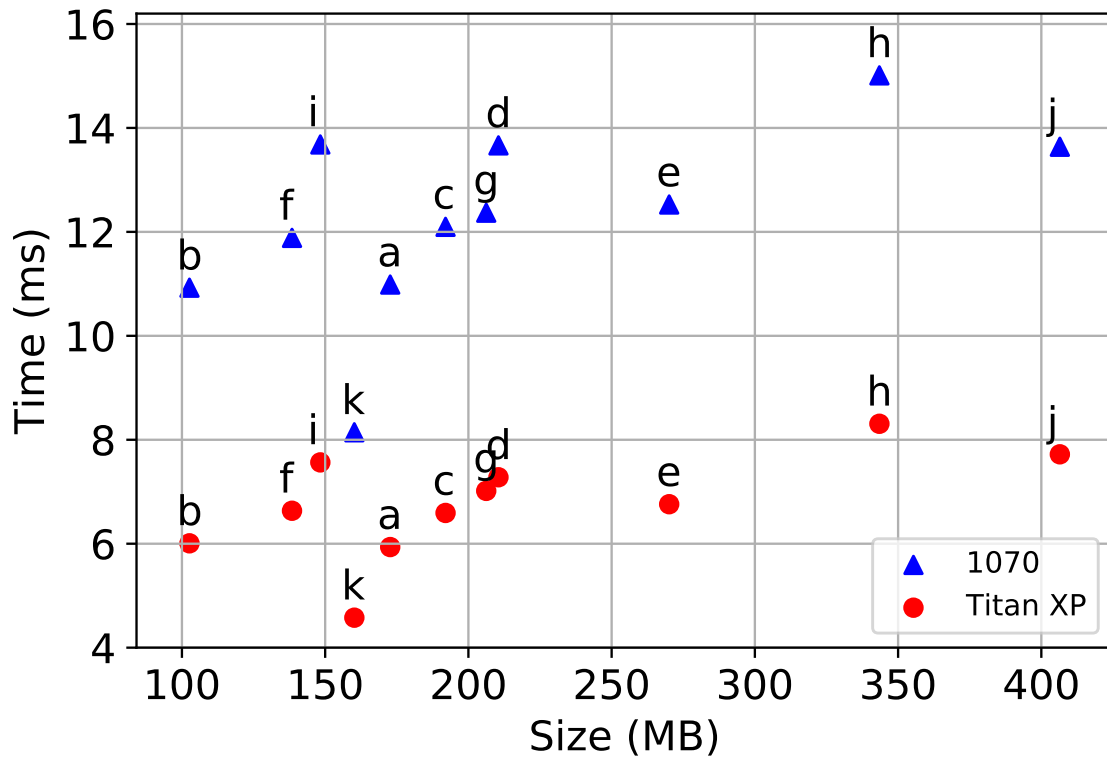


Figure 2.10: Time taken for classifying one candidate (in ms) with respect to the size of the model (in MB). Blue triangles represent evaluation times on NVIDIA GTX-1070, while red circles are for NVIDIA Titan-Xp. Labels A through K correspond to the models defined in Table 2.4

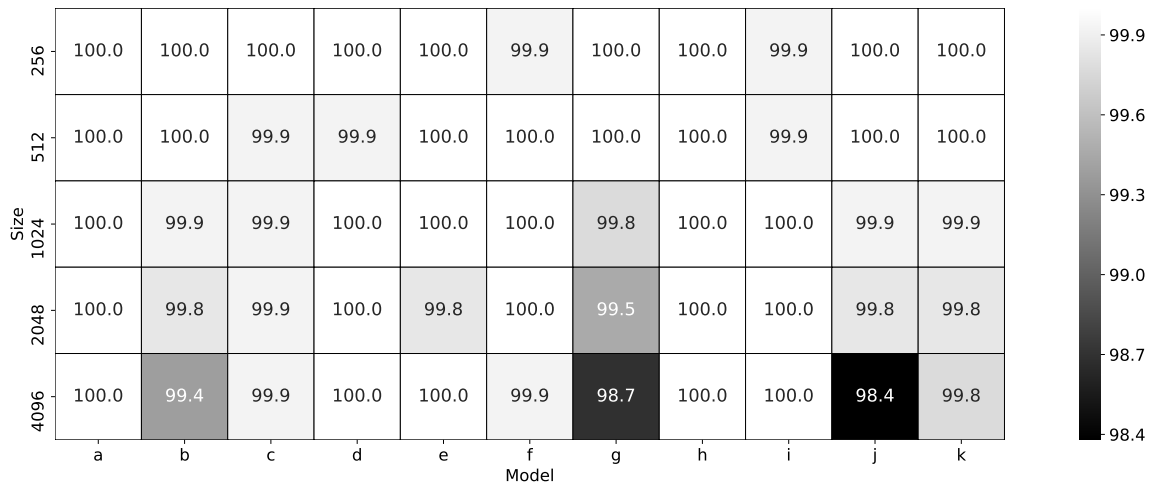


Figure 2.11: Heatmap for accuracies of differently sized frequency-time inputs. The accuracies are colour-coded and annotated. The time axis was kept to be 256 pixels. The Y-axis shows the number of pixels in the frequency axis. Labels A through K on the X-axis correspond to the models defined in Table 2.4

We also used the same number of RFI candidates for each input size. However, Gaussian noise was not added to the RFI images. We then used our top-11 models to evaluate these candidates. The results are presented as a heatmap in Fig. 2.11. This demonstrates that our models are not very sensitive to changes in image size, and only show a marginal decrease in accuracy, while the recall stayed at 100%. A larger image size could thus be used with our models to preserve the frequency modulation of FRBs. Hence, data from commensal FRB search back-ends, for example, CRAFT-ASKAP, GBTrans, UTMOST with 336, 512 and 320 frequency channels respectively, can directly be fed into the models.

### 2.5.3 Sensitivity Analysis

It is imperative to analyse the sensitivity of the models with respect to the S/N of the candidates. Although, the performance reported in Table 2.4 is useful to compare models, it is a cumulative number, i.e. how well the models performed on the complete test data. Figure 2.12 shows the recall as a function of S/N of the FRBs in the test dataset. To compute this, we used all the FRB candidates from the test dataset and binned them into 30 bins, each with an equal number of candidates. The top 11 models were used to classify these candidates, and recall per bin was calculated (refer to subsection 2.3.3 for details on recall calculation). As expected, recall improves as the S/N increases, as it is easier to classify higher S/N candidates. For most of our cases, the recall remained  $> 99\%$  above a S/N of 10 (except model G and  $\kappa$ ). We also note that, due to the limited amount of data, each bin only had a few hundred candidates, which are statistically not enough to quantify such a trend. Hence these recall values per bin should be taken with caution, and the figure should only be interpreted qualitatively. Typically, we would like to have several thousand candidates per bin in order to produce robust and reliable metrics.

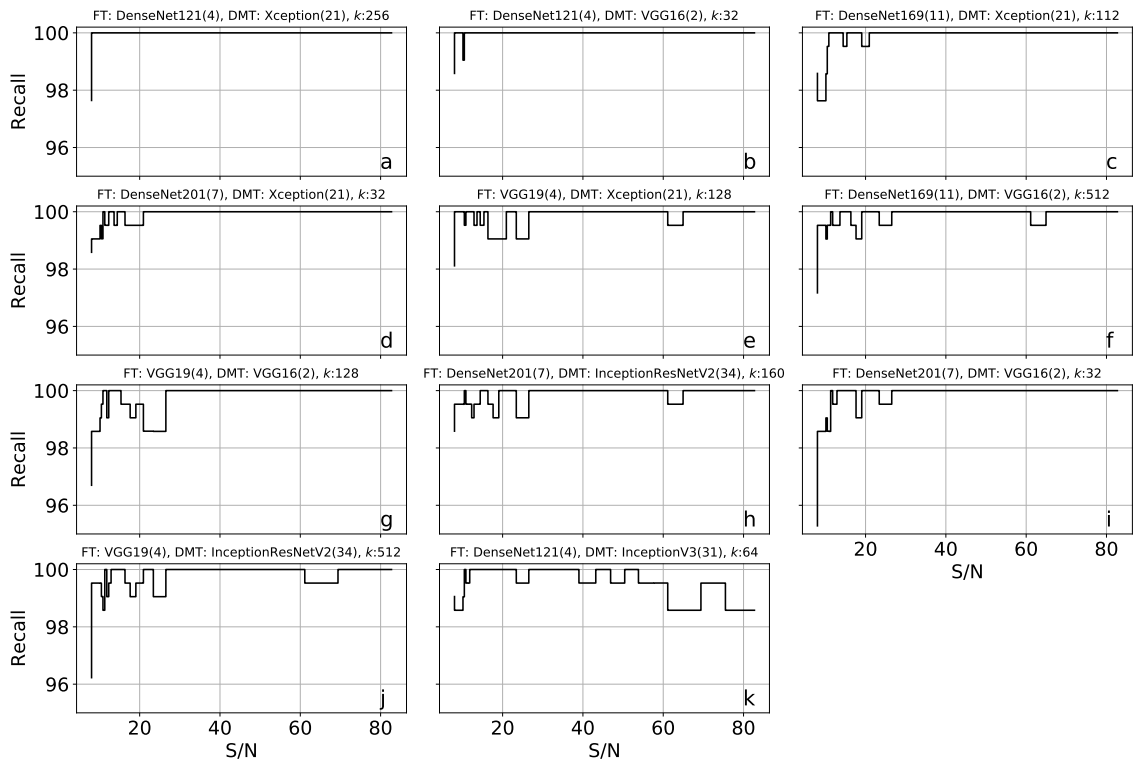


Figure 2.12: Recall vs Signal to noise (S/N) for top-11 models, evaluated on the test dataset. The FRBs from the dataset were binned into 30 S/N bins, each with an equal number of candidates. Labels A through K also correspond to the models defined in Table 2.4

### 2.5.4 Fine Tuning

While our models perform well on data from different telescopes and backends, it is still possible to further improve their performance for a specific use case. The models can be fine-tuned by re-training their final classification layer using few thousand candidates. In order to demonstrate this, we decided to use the data recorded at a frequency other than L-band, as all our models were originally trained on L-band data. For this purpose, we used the observations of FRB121102 recorded using Breakthrough Listen Digital Backend at 4–8 GHz (Gajjar et al., 2018).

We re-purpose the 652 RFI candidates as mentioned in §2.4.2. Using the procedure described in subsection 2.2.2 we generated 700 simulated FRB candidates at 4–8 GHz with the above-specified data as the background. 80% of this data was used for training, and 20% was marked for validation. The final classification layer was trained using the procedure described in subsection 2.3.2.1. To compare the performance of the fine-tuned models, we re-evaluate them on the 15 FRB 121102 pulses as shown in table 2.6. After fine tuning, all of our models (except model G) were able to correctly classify at least 14 out of 15 pulses, with six models classifying all 15 pulses correctly. This whole exercise took  $\sim 15$  min per model on an NVIDIA GTX-1070Ti GPU.

### 2.5.5 Comparison to Previous Work

In order to compare different machine learning algorithms in a fair manner, they should be evaluated on a common standard data set. As only a handful of FRBs has been detected to date, such a dataset cannot be created with real data. This has been discussed in great detail by Connor & van Leeuwen (2018). Also, machine learning algorithms like Support Vector Machines (Hearst, 1998) and Random Forest (Breiman, 2001) take advantage of the features, which are custom made to the specific telescope or survey. For example, the antenna covariance and network dropouts in the V-FASTR algorithm or relative candidate MJD information in the ALFABURST algorithm. Excluding such features would lead to performance degradation of the re-



spective classifier, thereby rendering the final comparison inconclusive. Realising the need for a standardised dataset, we provide our dataset<sup>1</sup> for testing future algorithms.

For the sake of completeness, we present a weak comparison between the Connor & van Leeuwen network by training and testing it on our data. We emphasise the fact that the authors trained their network on CHIME and LOFAR data independently, whereas our dataset contains a mixture of backends. We use the data as reported in table 2.1 and resize the images to (32, 64) pixels for frequency-time and (64, 64) for the DM-time. We omit the multi-beam S/N and pulse profile part of their network and train the merged model following the same procedure as reported by the authors. Pulse profile input wasn't included as it did not improve the test accuracy. Evaluating their model on the test data as reported in table 2.1, the accuracy, recall and fscore were 97.96%, 95.76% and 97.81% respectively. When compared on a common data set, our models show better performance. The differences in the performance elucidate two key features of our study – the importance of deeper neural networks and transfer learning. Transfer learning enabled the use of state-of-the-art neural networks for our application. These deep networks, extracted more generalised features and thus proved better at classification.

### 2.5.6 FETCH

We provide a user-friendly open-source python package FETCH (Fast Extragalactic Transient Candidate Hunter)<sup>2</sup>, for real-time classification of candidates from single pulse search pipelines, using our top-11 models. The input of FETCH is a candidate file containing the frequency-time and DM-time data. For each candidate and a choice of model, it outputs the probability of the candidate to be an FRB. These candidate files can be generated from filterbanks using PYSIGPROC<sup>3</sup>.

Using FETCH, the classification probabilities from all 11 models can be combined using simple mathematical operations like averaging, intersection, union or

---

<sup>1</sup><http://astro.phys.wvu.edu/fetch/>

<sup>2</sup><https://github.com/devanshkv/fetch>

<sup>3</sup><https://github.com/devanshkv/pysigproc>

majority voting. This would result in a more robust classification. This approach however is slower, and requires more computational resources. If only one model has to be used, the model A should be chosen, as it performs the best on our metric (see Table 2.4). FETCH also provides a framework to fine-tune the models to further improve its performance for particular backends. As demonstrated in subsection 2.5.4, this can be done with a few thousand labelled candidates. It is recommended to use a balanced dataset, wherein the number of RFI and FRB candidates are comparable.

Presently, FETCH is integrated into the GREENBURST pipeline and REALFAST for commensal FRB searches at the GBT and Very Large Array telescope respectively. For REALFAST, along with frequency-time and DM-time networks and FETCH will feature an additional third network with radio image as an input.

## 2.6 Conclusions

This chapter presented the development of a deep learning-based state-of-the-art classifier for FRB search candidates. We made the models freely available and released our training and testing datasets to provide a standard testbed for future algorithms. We demonstrated that our models are frequency and telescope agnostic and can easily be added to any FRB search pipeline. In the next chapter, we will discuss the deployment of FETCH in a real-time commensal pipeline at the Green Bank Telescope.

## Chapter 3

### Initial Results From a Realtime FRB Search With the GBT

#### 3.1 Introduction

Detection of FRBs requires data at radio frequency to be de-dispersed at many trial DM values. For each DM, all the frequencies are added to form a time series which is then searched using matched filters to find bursts above a certain threshold. With the help of Graphics Processing Units (GPUs), it is now possible to perform such searches in real time (Magro et al., 2011; Barsdell et al., 2012; Karastergiou et al., 2015; Adamek & Armour, 2019). Inspired by the capabilities of real-time processing which has been successfully implemented at Parkes (see Osłowski et al., 2019, for recent commensal discoveries), many radio telescopes around the globe are deploying commensal search backends to enable serendipitous discoveries of FRBs. A few examples include: REALFAST (Law et al., 2018) at the Very Large Array, the CRAFT survey with the Australian Square Kilometre Array Pathfinder (ASKAP) telescope (Macquart et al., 2010), ALFABURST at the Arecibo observatory (Chennamangalam et al., 2017a; Foster et al., 2017) and GBTrans using the 20 m telescope at Green Bank (Golpayegani et al., 2019). With such backends, a copy of the data from the receiver is de-dispersed and searched for FRBs. Real-time detection of FRBs is required for prompt follow-up at other wavelengths that might provide valuable insights towards understanding the underlying emission mechanisms and possible progenitors.

In this chapter we present the results from 3756 hours on sky from the commensal backend at the 110 m Robert C. Byrd Green Bank Telescope (GBT). We

---

Published as Agarwal et al. (2020b)

**Contributing authors:** D.R. Lorimer, M.P. Surnis, X. Pei, A. Karastergiou, G. Golpayegani, D. Werthimer, J. Cobb, M.A. McLaughlin, S. White, W. Armour, D.H.E. MacMahon, A.P.V. Siemion, G. Foster.

henceforth refer to this system as GREENBURST . This chapter is organised as follows. We first describe and summarise the system description and detail the FRB search pipeline in section 3.2 followed by benchmarks of our pipeline in section 3.3. In section 3.4 we present results from our commensal observations and constraints on FRB rates. In section 3.5, we discuss the consequences of our results in terms of FRB source counts and predictions for ongoing future experiments.

## 3.2 Search Pipeline

The system description is detailed in Surnis et al. (2019) and is summarised here. Using a dedicated directional coupler designed and built at the observatory, we obtain a copy of the signal from the L-band (21 cm) receiver. This signal is then digitised using a field programmable gate array on board the SETIBURST backend (Chennamangalam et al., 2017b) and sampled every  $256 \mu\text{s}$  with 8-bit precision. The resulting data stream consists of 4096 channels spanning a 960 MHz bandwidth at a central frequency of 1440 MHz. A unique property of this system is that even when the L-band receiver is not in the primary focus, it still is illuminated by a large part of the dish. The fraction of dish illuminated at each turret position can be quantified using aperture efficiency ( $\eta$ ). These values are reported in table 3.2. As a result, it can be used commensally with observations at other frequencies.

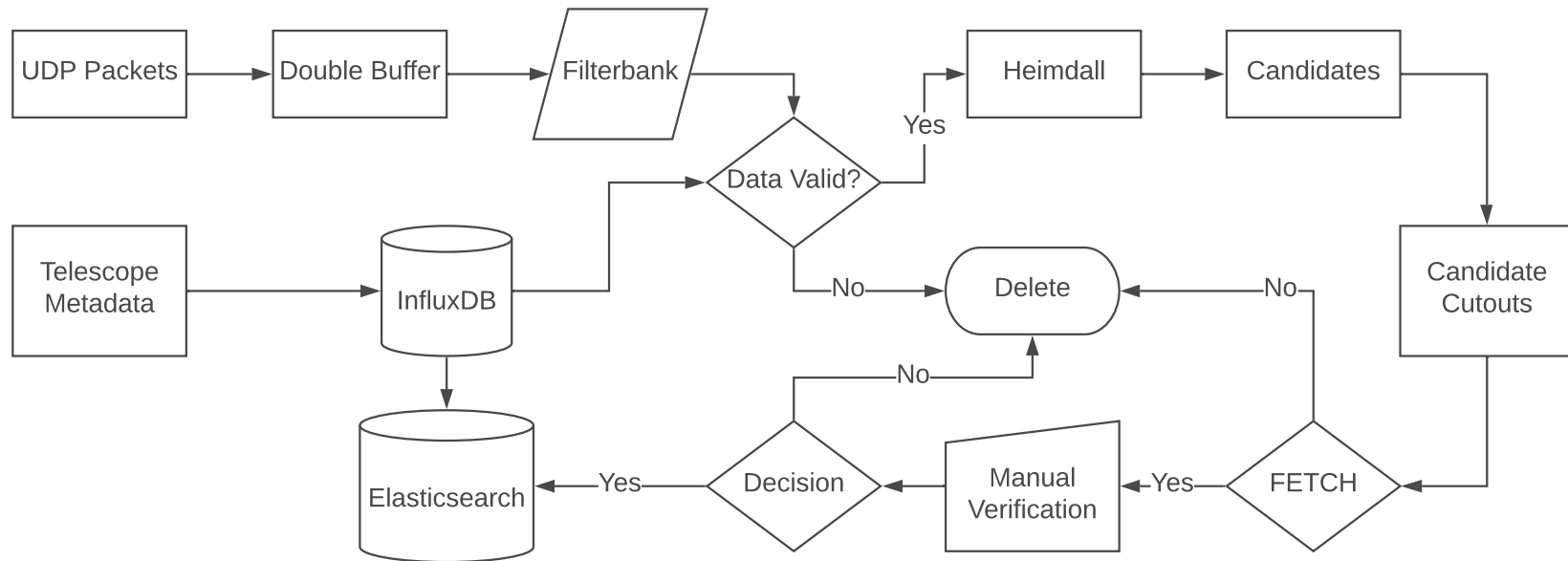


Figure 3.1: Schematic depiction of the detection pipeline. Data through ethernet arrives as user datagram protocol (UDP) packets. Using a double buffer system, data from the UDP packets are rearranged and written in filterbank format. In parallel, all the telescope metadata are saved in the influx database at 1 s intervals. Once a filterbank file is written, data validity is checked (see text for details). Valid data are searched with HEIMDALL. Candidates are then parsed through FETCH, and positively labelled candidates are sent for visual inspection. A condensed version of telescope metadata and the candidates is saved in elasticsearch for future reference.

Fig. 3.1 details our search and verification pipeline. The symbols used in the flowchart are detailed in Chapin (1970). The digitised data are transported over an ethernet connection to a dedicated computer which processes and stores the data as binary files in `filterbank` format (Lorimer et al., 2000). The filterbank files contain 16 chunks of  $2^{17}$  samples corresponding to  $10,000 \text{ pc cm}^{-3}$  DM delay along with an overlapping chunk from the last file. The overlap ensures that no transient events are missed due to data being split between two files. In parallel, the telescope metadata, which includes the receiver turret angle, telescope pointing altitude and azimuth, and observing project IDs are recorded at a cadence of one second in influxDB<sup>1</sup>. This serves as a high-resolution short term storage database, where the metadata are saved for seven days.

Once a filterbank file is written, data validity is checked using metadata from influxDB. The data are considered invalid if any of the following conditions are met.

- The receiver turret is unlocked. This typically happens when the observer changes the receiver in focus.
- The turret angle is between  $160^\circ$  and  $220^\circ$ . At these angles the GBT primary focus feed structure blocks the receiver’s field of view.
- The primary focus receiver is extended due to the same reason as above.

If the data are valid, we first excise radio frequency interference (RFI) from affected channels using the following method. All the time samples are added to form a bandpass of the data. The bandpass is smoothed using a Savitzky–Golay filter. Here we use a running window of 61 data samples and fit a second-order polynomial to obtain a smooth bandpass. The measured and smooth bandpass are subtracted from one another. Through empirical investigations with preliminary data, we found that a good RFI excision procedure is to use this subtraction result and flag any channels which differ from the smooth bandpass by more than five counts<sup>2</sup>. Both the window

---

<sup>1</sup><https://www.influxdata.com>

<sup>2</sup>Here we use the term “count” to refer to an intensity value quantized in the range 0–255. Five counts corresponds to  $\sim 6$  times the root mean square value of the data.

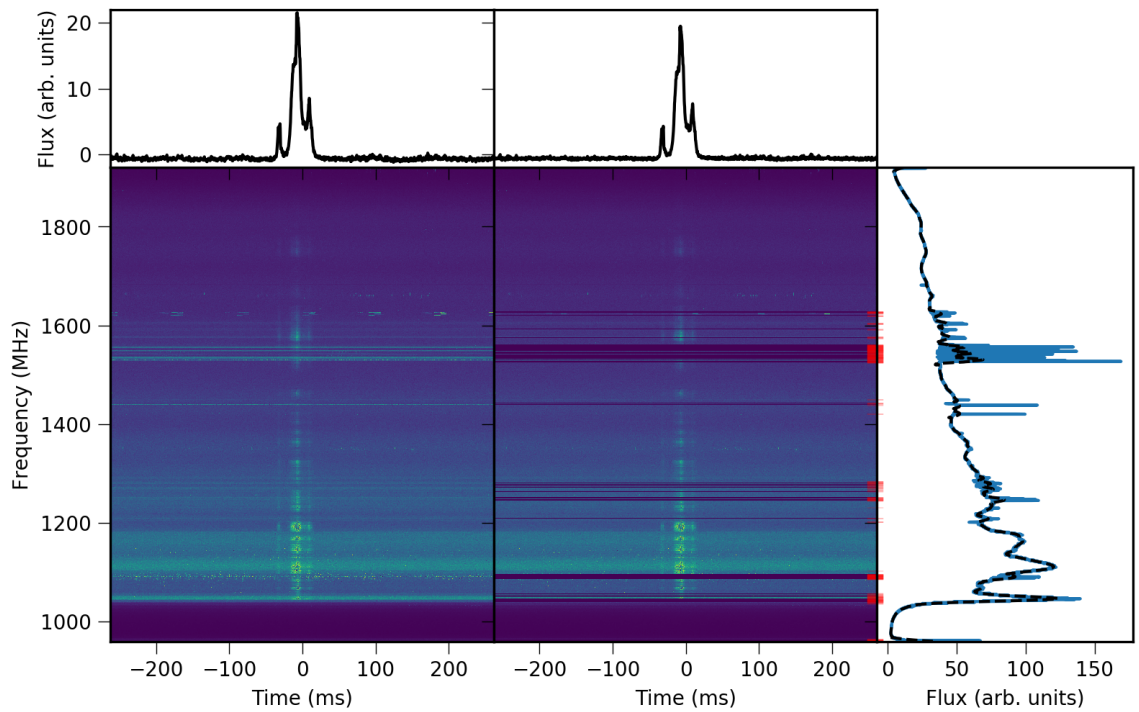


Figure 3.2: Radio frequency interference clipping using the Savitzky–Golay filter. The bottom left, and middle plots show the raw and cleaned de-dispersed spectrum of a single pulse from PSR B0329+54. In the bottom right panel, the raw bandpass is shown in blue, while the smoothed bandpass from the filter is shown by the black dashed lines. The red lines mark the flagged channels. The top left and middle plots show the frequency integrated profile of the single pulse.

size and the difference threshold were determined empirically. Fig. 3.2 shows the profile of PSR B0329+54, before and after masking bad channels. The amount of RFI excision depends strongly on the local environment at the time, typically we flag 8–10% of channels. For example in figure 3.2 this process flags 350 (out of 4096) channels. In §3.4 we account for the sensitivity loss due to RFI flagging by reducing our bandwidth by 10%. In parallel, a coarse version of the telescope metadata is computed by binning by time spent by the telescope in each  $1^\circ \times 1^\circ$  patch in the Galactic latitude-longitude grid. The metadata are subsequently used to generate sky coverage maps and rate calculations of FRBs described below.

We use HEIMDALL<sup>3</sup> along with the bad channel flags to search for pulses in the range  $10 \leq \text{DM} \leq 10,000 \text{ pc cm}^{-3}$ , and smoothing over  $[2^0, 2^1, \dots, 2^7]$  adjacent samples spanning widths in the range  $256 \mu\text{s}—32.768 \text{ ms}$  above a signal to noise ratio (S/N) of 8. The candidates above the S/N threshold are then classified as either RFI or an astronomical transient using model a of the artificial neural network FETCH (Agarwal et al., 2020a). Candidates labelled as positives are then sorted into two categories: Galactic and extragalactic. We do this by computing the expected DM contribution in the direction of observation by integrating the electron density by both NE2001 and YMW16 models out to 25 kpc. The smaller of the two DM estimates is chosen as the Galactic DM in that direction. Both DM models commonly underestimate and overestimate DMs in certain directions. For example, The CHIME/FRB Collaboration et al. (2019b) report the repeating FRB 180916.J0158+65, YMW16 places the source within the Milky Way while NE2001 predicts it to be outside. We avoid such cases by taking a conservative approach and using the minimum of the two estimates while processing. Further investigations can be dealt in the post processing on a case by case basis. In case the candidate DM is Galactic, the position and DM are matched with the ATNF pulsar catalogue (Manchester et al., 2005) to verify if the candidate is a known source. If the source is unknown or the DM is larger than the Galactic DM, the candidates are marked for manual verification. Positively marked

---

<sup>3</sup><https://sourceforge.net/projects/heimdall-astro>



Table 3.1: Distributions of FRBs injected for benchmarking the pipeline

Parameter name	Distribution
Signal-to-noise ratio	Uniform(6,100)
Pulse width	Uniform(0.5, 26) ms
Spectral index	Uniform(-3,3)
Scattering time	Uniform(0.256,6.5) ms
Number of scintillation patches	Log-Uniform(-3, 2)

candidates are stored in the elasticsearch<sup>4</sup> database.

### 3.3 Pipeline Benchmarks

To assess the completeness of our pipeline, we injected fake FRBs with various observational parameters and run the complete pipeline as detailed in §3.2. Based on the results from our pipeline we compute several metrics to quantify the pipeline’s ability to detect FRBs.

#### 3.3.1 Blind FRB injections

To inject FRBs, we first randomly select filterbank files from the observations on a single day (MJD 58728). On this date, all the data were acquired using the L-band receiver. The parameters of the injected FRB distribution are summarised in Table 3.1. For each injection, first a random start time in the file is chosen such that there is enough data to fully inject the dispersion delay. Then, Gaussian-shaped profiles are created for each channel with standard deviation

$$w = \sqrt{t_{\text{samp}}^2 + t_{\text{DM}}^2 + w_{\text{int}}^2}. \quad (3.1)$$

Here  $t_{\text{samp}} = 256 \mu\text{s}$  is the sampling interval,  $t_{\text{DM}}$  is the dispersion smearing (the delay due to dispersion across a channel bandwidth) and  $w_{\text{int}}$  is the intrinsic pulse width drawn from a uniform distribution between 0.5 and 26 ms. This profile is then convolved with an exponential function of the form  $e^{-t/\tau}/\tau$ , where  $\tau$  is randomly

<sup>4</sup><https://www.elastic.co/elasticsearch>

drawn from a uniform distribution of 0.256 and 6.5 ms, to add scattering the the profile. The lower limit is 0.256 ms and not zero because of the  $1/\tau$  normalisation factor and the upper limit of 6.5 ms such that the resultant widths of the scattered FRBs are similar to the observed population at 1 GHz. This choice is reasonable as Ravi (2019) show an observed median scattering time of  $\sim 4$  ms at 1 GHz. These profiles are then scaled with the spectral index by multiplying with  $(\nu/\nu_{\text{ref}})^\gamma$ . Here  $\nu$  is the channel frequency,  $\nu_{\text{ref}}$  is the reference frequency of 1400 MHz and  $\gamma$  is the spectral index. Scintillation is added to the data by modulating the spectra using the positive half of a cosine function. The number of such patches are drawn from a log-normal distribution of mean  $-3$  and standard deviation of  $2$ . The above parameters lead to  $\sim 10\%$  of FRBs with a patchy spectral structure. To add scintillation we create an envelope where  $N_s$  is the number of bright patches which is multiplied with the pulse. The envelope,

$$E = \cos \left[ 2\pi N_s \left( \frac{\nu}{\nu_{\text{ref}}} \right)^2 + \phi \right], \quad (3.2)$$

is generated with  $\phi$  being a random phase in the range  $0$  to  $2\pi$  drawn from a uniform distribution.  $E > 0$  values are then multiplied with  $S$  to simulate scintillation. The parameters from the above-described distributions are drawn and injected using the publicly available code `injectfrb`<sup>5</sup>. To create realistic bright FRBs, as our the data are 8-bit unsigned integers, for cases where the profile intensity exceeds the dynamic range the values are wrapped around the maximum value of 255. This is done because the FPGA wraps the numbers exceeding the dynamic range instead of clipping them at the maximum value. An instance of this can be viewed in Fig. 3.2 where dark blue patches can be seen within the dynamic spectrum of the pulsar.

### 3.3.2 Evaluation Metrics

To quantify the performance of our pipeline, we calculate what is known as “recall” (Sammut & Webb, 2017) which is simply the ratio of the number of recovered

---

<sup>5</sup><https://github.com/liamconnor/injectfrb>

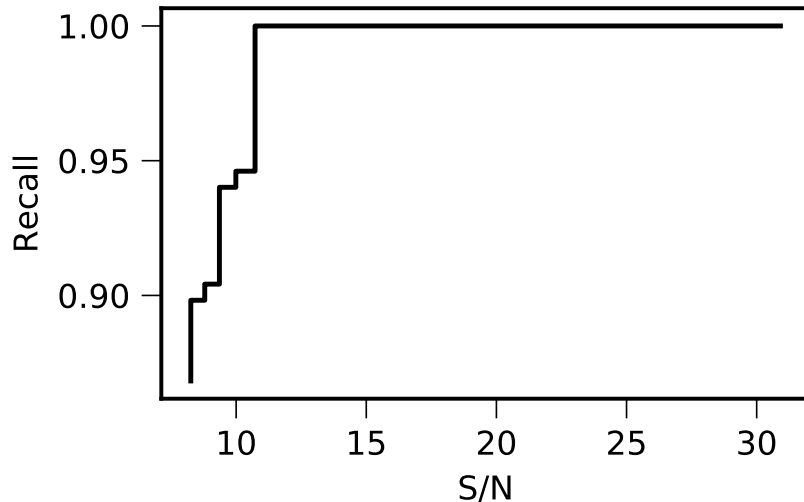


Figure 3.3: The parametric recall curve. The ordinate and abscissa correspond to the injected S/N and the recall respectively. The curve indicates that our pipeline is able to recover all the injected FRBs with  $S/N \gtrsim 12$ .

FRBs to the total number of injected FRBs. While there are other metrics like accuracy and precision, their calculation involves the number of false positives which themselves depend on the RFI environment at the time of the observations and the performance of the RFI mitigation algorithms. We restrict our evaluation to the recovery of injected FRBs, and hence, we chose to evaluate using recall. To extract deeper insights than traditional recall, we here define a parameter weighted recall which we call parametric recall (PR). For this analysis we inject  $\sim 1200$  FRBs and we chose S/N as the parameter. Then, injected data are binned with respect to the parameter such that each bin has an equal number of points and the recall is calculated for each bin. PR can also be understood as the first moment of a distribution of recall over the given parameter ( $\mathcal{P}$ ). In this framework, we have

$$\text{PR} = \frac{\sum_{i=0}^{N_{\text{bins}}} \text{Recall}_i \mathcal{P}_i}{\sum_{i=0}^{N_{\text{bins}}} \mathcal{P}_i}. \quad (3.3)$$

Here,  $\mathcal{P}_i$  and  $\text{Recall}_i$  is the mean  $\mathcal{P}$  and the recall of the  $i^{\text{th}}$  bin. The maximum value for the PR is unity, i.e. the pipeline found all FRBs at all injected S/N values. In case where the pipeline misses FRBs at high S/N the PR would be penalised more

resulting in lower overall score. Hence PR is a better measure of performance as compared to traditional recall.

To test if the number of simulated injected FRBs are enough, we run the following experiment. We start with 500 injections and compute the PR. We then add 50 simulated FRBs to the set and calculate the fractional difference between each of the PRs until this difference is below 0.1%. We find that above 900 injections, the fractional difference stays smaller than our threshold of 0.1%. As the fractional difference does not rise above over threshold for more than five such consecutive additions, we conclude that our 1200 simulated injected FRBs results in a stable PR value.

Fig. 3.3 shows the PR for the injected S/N as parameter ( $\mathcal{P}$ ). As can be seen from the plot, the pipeline is able to recover all events above a S/N  $\sim 12$ . The PR from the above stated curve is 0.95. We inspected the candidates missed by the pipeline injected between a S/N of 8 to 12. All the candidates missed are due to the presence of strong RFI near the signal. In future, we plan to implement more sophisticated RFI mitigation algorithms to prevent achieve a lower S/N threshold with 100% reliability.

### 3.4 Results

GREENBURST started commensal observations on MJD 58587 (2019-03-14) and, as of MJD 58917 (2020-03-09), has observed for 156.5 days. While the backend has been operational for 330 days, only  $\sim 50\%$  of the available time has been spent on sky. This because of several factors that govern the validity of the data such as the telescope down time for maintenance, availability and observer’s choice of the receiver (see §3.2 for details).

Fig. 3.4 shows the sky coverage during this time in equatorial coordinates. The hexagons show  $6^\circ \times 6^\circ$  area with colour bar representing the hours spent in the region.

Table 3.2 shows the time spent, solid angle, sensitivity (for S/N = 12) and aperture efficiency at each turret position . The sensitivity shown here is slightly different when compared to the numbers we reported earlier (Surnis et al., 2019) where we assumed a bandwidth of 960 MHz for the calculation and a S/N threshold

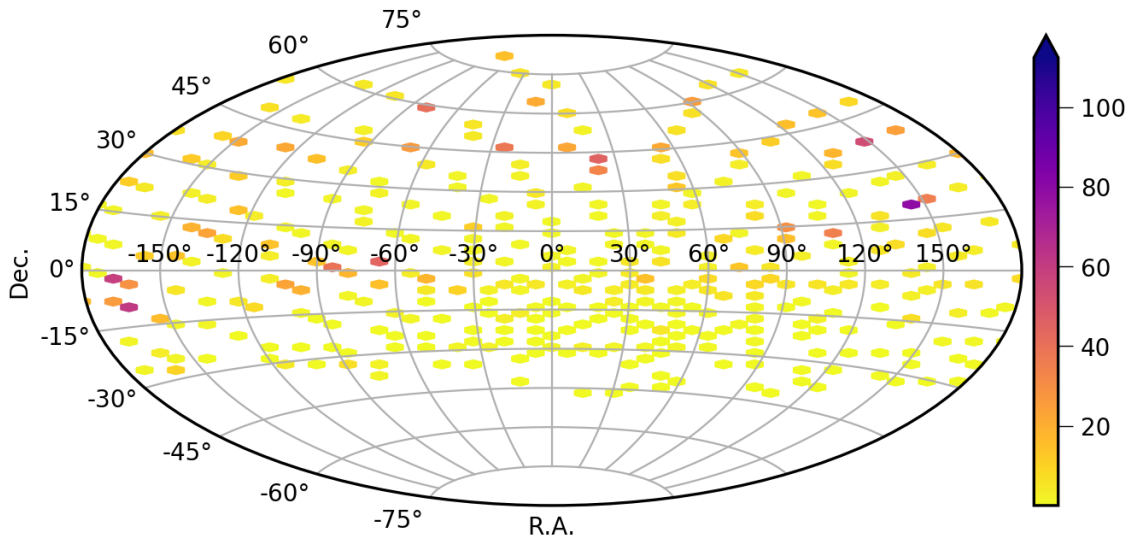


Figure 3.4: Sky coverage during commensal observations. The figure shows the coverage as  $36 \text{ deg}^2$  hexagonal bins in the sky as an equatorial projection. as the respective axes. The color bar denotes the total hours spent in each bin by all turret positions.

Table 3.2: GREENBURST observational summary to date. From left to right, we list the receiver in prime focus, the turret angle relative to the L-band receiver, the time spent on sky with that receiver, the instantaneous solid angle covered ( $\Omega$ ), the sensitivity as evaluated from the blind injection analysis (see §3.1) and aperture efficiency ( $\eta$ )

Receiver	Turret Angle ( $^\circ$ )	Observation Time (hr)	$\Omega$ $\times 10^{-2}$ (sr)	Sensitivity (Jy)	$\eta$
L-band	0	2194	3.12	0.14	0.70
X-band	260	615	3.33	0.89	0.26
C-band	60	556	3.19	0.25	0.54
Ku-band	100	210	3.40	0.80	0.28
MUSTANG	300	181	3.26	0.26	0.52

Table 3.3: Known pulsars detected by GREENBURST during commensal observations.  $N_{\text{pulses}}$  is the number of single pulses detected,  $S/N_{\text{max}}$  is the max S/N detected for the corresponding pulsar. DM and the  $S_{1400}$  is the dispersion measure and the mean flux density at 1400 MHz respectively from the ATNF pulsar catalogue.

Pulsar	DM (pc cm <sup>-3</sup> )	$N_{\text{pulses}}$	$S/N_{\text{max}}$	$S_{1400}$ (mJy)
B0329+54	26.76	113	195	203
J0426+4933	85.00	1	17	0.19
B0450-18	39.90	423	77	16.8
B0818-13	40.94	258	115	6
B0919+06	27.29	2	14	10
B1508+55	19.62	49	29	8
B1702-19	22.91	316	80	9.3
B1718-35	496.00	4	11	16.8
B1745-20A	219.40	21	13	0.37
B1804-08	112.38	102	30	18.2
B1822-09	19.38	71	137	10.2
B1933+16	158.52	408	262	57.8
B1937+21	71.02	14	17	15.2
B1946+35	129.37	125	133	8.3
B2021+51	22.55	26	51	27
B2035+36	93.56	2	42	0.8
B2111+46	141.26	28	99	19
B2154+40	71.12	58	75	17
B2217+47	43.50	90	73	3
B2310+42	17.28	43	43	15

of 12. Soon after the backend became functional, due to the presence of RFI, it was decided to always have the notch filter which blocks frequencies in the range 1.25–1.35 GHz in place. This filter is only taken out by the observer (primarily for pulsar/FRB observations). Along with the notch filter, we routinely flag  $\sim 10\%$  of the total band band reducing our bandwidth to 760 MHz. The beam solid angle,  $\Omega \approx 1.33 \text{ FWHM}^2$ , where FWHM is the full width at half maximum and is taken from Surnis et al. (2019).

During observations so far, we detected 2153 single pulses from 20 pulsars. Table 3.3 shows the number of single pulses observed from each pulsar. Fig. 3.5 shows the waterfall plot and frequency integrated time profile of the brightest single pulse from each pulsar. The pulsars in the figure are de-dispersed at the detection DM and at

the DM of the pulsar. The two DMs are often different because the detection DM is a sample from the coarser grid of trial DMs used for the search. The presence of RFI and zero DM subtraction also contributes towards the difference between the DMs. As a result in some cases the effects of residual dispersion can be seen. In case of PSR B1804-08 we can see three single pulses from the pulsar (the fourth pulse is narrow band RFI). For PSR B1946+35 the burst near  $\sim 300$  ms is also RFI.

## 3.5 Discussion

### 3.5.1 Time to first GREENBURST detection

So far, we have observed for 156.5 days and detected no FRBs. To check whether our non-detection is anticipated, we first use previous estimates of the all-sky rate of FRBs

$$\mathcal{R}(S) = \mathcal{R}_0 \left( \frac{S}{\text{Jy}} \right)^{-\alpha}, \quad (3.4)$$

where  $\mathcal{R}_0$  is the reference rate and  $\alpha$  is the source count index from the log  $N$ -log  $S$  relation. In their analysis, Lawrence et al. (2017) found  $\mathcal{R} = 587_{-305}^{+337}$  events per day per sky and  $\alpha = 0.91 \pm 0.34$  where the uncertainties indicate the 95% confidence interval. Using these parameters, we estimate the waiting time to discover an FRB,  $\mathcal{W} = 1/\mathcal{R}\Omega$  where  $\Omega$  is the beam solid angle. Using the rates from Lawrence et al. (2017), we find  $\mathcal{W} = 532_{-184}^{+1042}$  days for the first detection. This is significantly larger than our present observing time.

### 3.5.2 The all-sky FRB rate

We now use our null result to update the non-homogeneous Poisson process framework developed by Lawrence et al. (2017) to find revised estimates  $\mathcal{R}$  as well as the source count index  $\alpha$  of FRBs by taking into account both the detections and non-detections. We implemented the analysis described by Lawrence et al. (2017) using the information from 12 surveys which included 15 detections. We extend this analysis by adding 14 surveys (including this work) with 33 FRBs. We extend the

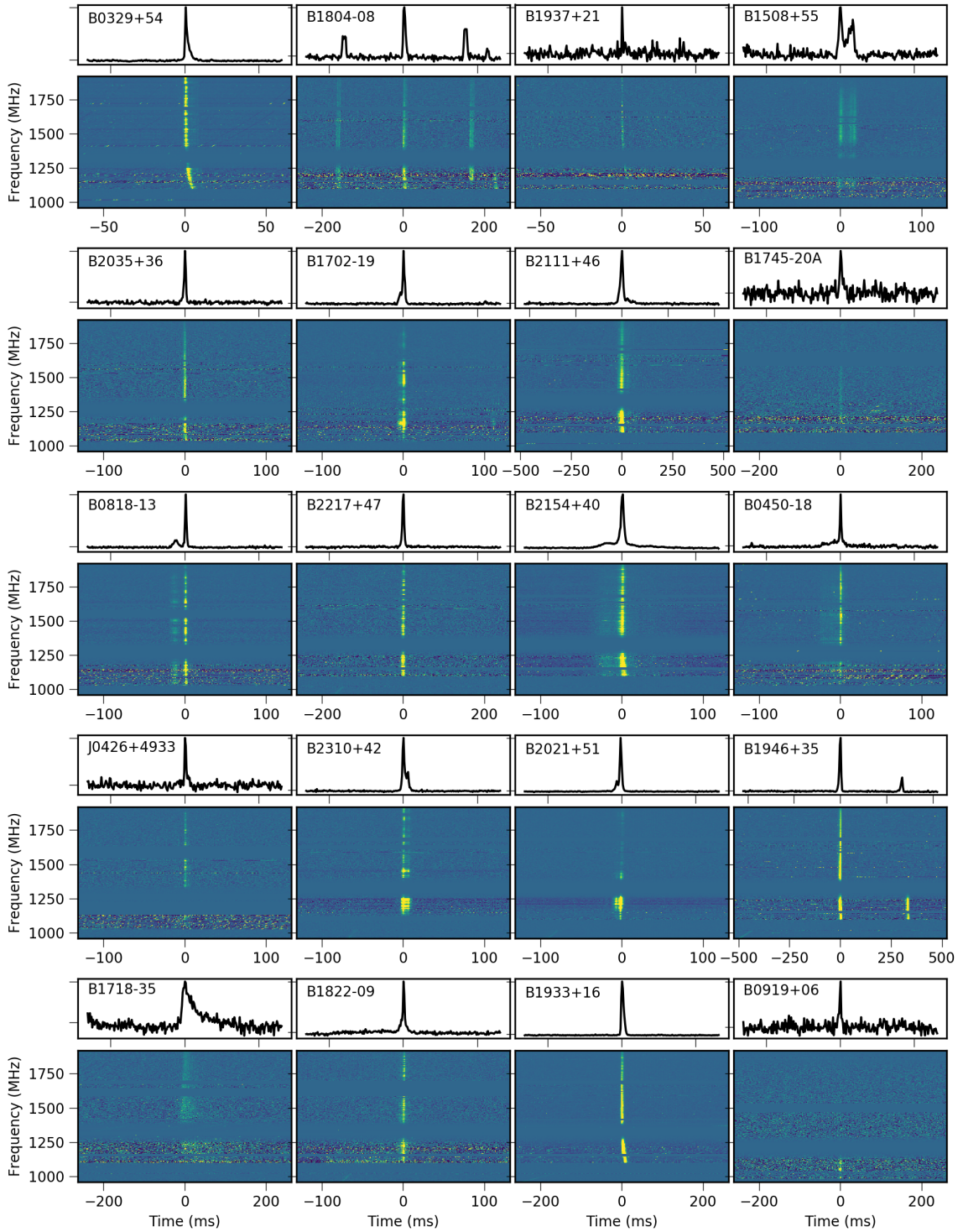


Figure 3.5: Brightest single pulses from various pulsars dedispersed at their detection DM. The figure shows the waterfall plot and frequency integrated time profile of the brightest pulses from 20 pulsars listed in Table 3.3. Pulsars are marked in the top left corner in each plot respectively.



datasets of Lorimer et al. (2007) by including FRB 010312 (Zhang et al., 2019) which is the second FRB in the original data set, and Thornton et al. (2013) by including FRB 110214 (Petroff et al., 2018) which was found by processing the remaining 0.5% of the HTRU survey. We add the recently discovered FRB 010305 from the Parkes high latitude survey (Zhang et al., 2020). We include 23 FRBs from ASKAP (Shannon et al., 2018; Qiu et al., 2019; Bhandari et al., 2019; Agarwal et al., 2019). We also include 8 FRBs from the Parkes telescope (Bhandari et al., 2017; Osłowski et al., 2019). We also incorporate various surveys reporting non-detections (Men et al., 2019; Golpayegani et al., 2019; Madison et al., 2019).

As shown in Table 3.2, each turret position has different sensitivity and observing time. In order to include these the above described framework, observations at each turret position have been added as a different survey.

For this analysis, we exclude the FRBs from CHIME and UTMOST as they were carried out at different observing frequencies and have non-Gaussian beamshapes which are currently not Incorporated into the framework. We also exclude several other surveys which have reported non-detections but were carried out in different frequency bands.

We implement the likelihood formalism of Lawrence et al. (2017) and use Markov Chain Monte Carlo (MCMC) simulation to obtain distributions of  $\mathcal{R}_0$  and  $\alpha$ . We implement the MCMC using the EMCEE<sup>6</sup> framework (Foreman-Mackey et al., 2013) with a uniform prior of  $\alpha$  and a log-uniform prior on  $\mathcal{R}_0$ . The resultant posterior distributions for  $\log(\mathcal{R}_0)$  and  $\alpha$  are shown in Fig. 3.6. From this analysis, we infer the FRB rate

$$\mathcal{R} = 1150_{-180}^{+200} \left( \frac{S}{\text{Jy}} \right)^{-0.84 \pm 0.06} \text{day}^{-1} \text{sky}^{-1}. \quad (3.5)$$

Here the quoted uncertainties corresponding to 95% confidence intervals. We find a higher rate for the FRBs above 1 Jy, as compared to the Lawrence et al. which was  $587_{-315}^{+337} \text{day}^{-1} \text{sky}^{-1}$ , however, the error regions with both the estimates overlap. Our source count index distribution is shallower than the Lawrence et al. value of

---

<sup>6</sup><https://github.com/dfm/emcee>

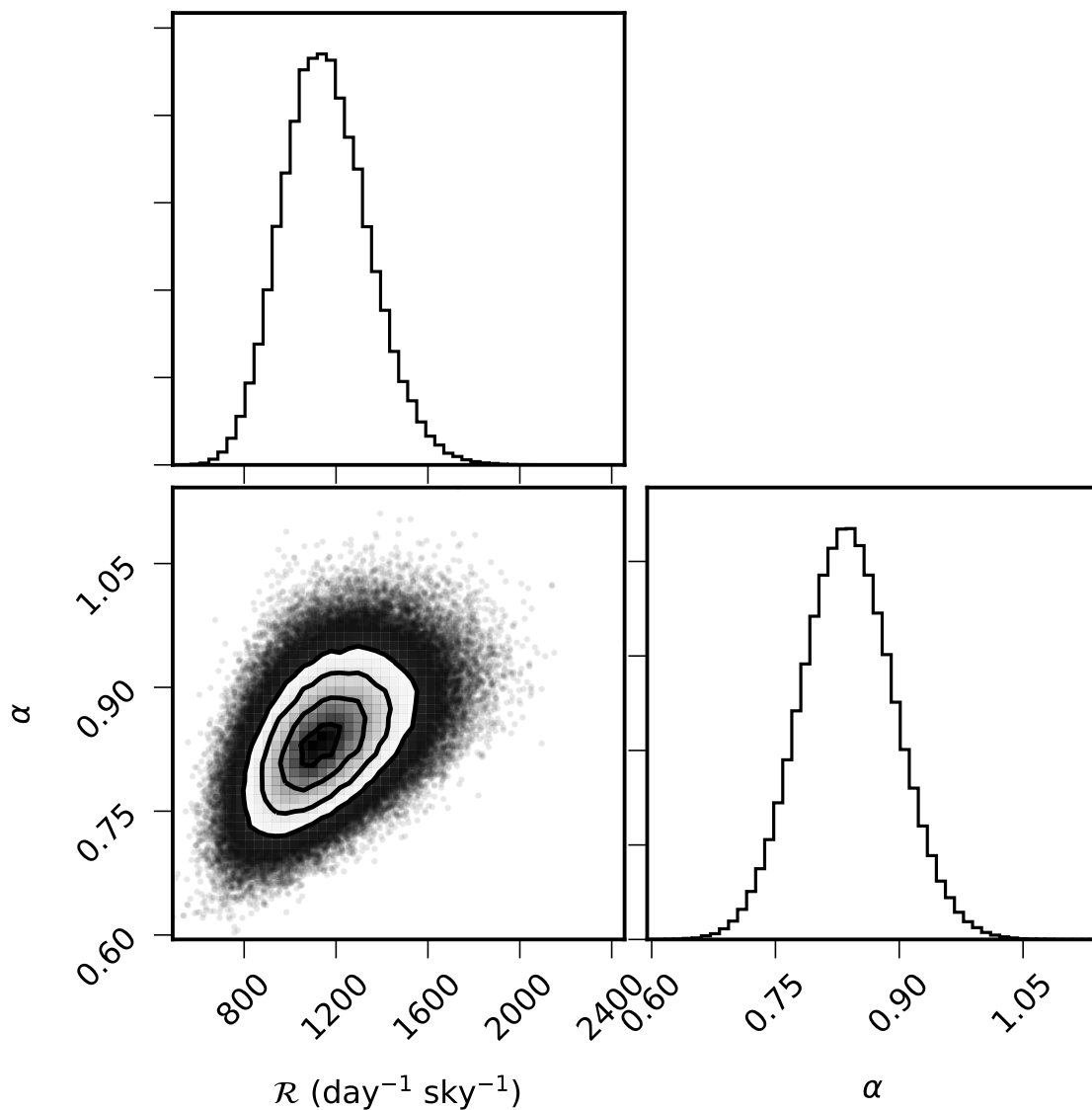


Figure 3.6: Joint and marginalized probability density functions for the FRB rate,  $\mathcal{R}$ , and source count index,  $\alpha$ , that were returned by our implementation of the Bayesian framework developed by Lawrence et al. (2017).

Table 3.4: FRB detection rate predictions for various telescopes. From left to right, for each experiment, we list the telescope’s field of view (FOV), the observing bandwidth ( $\Delta\nu$ ), the centre frequency ( $\nu_{\text{centre}}$ ) and the system equivalent flux density (SEFD) as well as the predicted rate ( $R$ ).

Telescope	FOV (deg <sup>2</sup> )	$\Delta\nu$ (MHz)	$\nu_{\text{centre}}$ (MHz)	SEFD (Jy)	$R$ (day <sup>-1</sup> )
CHIME	200	400	600	45	$9 \pm 2$
HIRAX	56	400	600	6	$10 \pm 3$
CHORD	130	1200	900	9	$4 \pm 1$
Northern Cross	350	16	408	95	$2 \pm 1$

$0.91 \pm 0.34$  but lies within their predicted ranges.

Based on this revised event rate, we predict that (for observations exclusively at L-band), GREENBURST will require a further  $264_{-87}^{+64}$  days to make its first detection. As can be seen from Table 3.2, L-Band is in focus for only  $\sim 65\%$  of the total on sky time. Hence a more realistic estimate for the time to first detection is  $356_{-117}^{+86}$  days.

### 3.5.3 Detection rate forecasts for other surveys

Using our estimates from Eq. 3.5 we compute expected FRB rates for experiments planned with four telescopes: CHIME (Amiri et al., 2018), CHORD (Vanderlinde et al., 2019), Northern Cross (Locatelli et al., 2020) and HIRAX (Newburgh et al., 2016). To estimate the rate for each survey, we compute the minimum flux density using the radiometer equation assuming a S/N threshold of 10. For experiments at frequencies outside of L-band, we assume a flat spectral index (i.e. no scaling of  $\mathcal{R}$  with frequency). For CHIME and CHORD, the system equivalent flux density

$$\text{SEFD} = \frac{T_{\text{rec}} + T_{\text{sky}}}{G}, \quad (3.6)$$

where  $T_{\text{rec}}$  and  $T_{\text{sky}}$  are the receiver and the sky temperatures, respectively, and  $G$  is the antenna gain.  $T_{\text{sky}}$  is estimated using an average sky temperature of 34 K and a spectral index of  $-2.6$  at a reference frequency of 408 MHz (Haslam et al., 1982). The results from these calculations are shown in Table 3.4. Our predictions for the

CHIME telescope of detecting  $9 \pm 2$  FRBs per day are consistent with the estimates by Chawla et al. (2017) where the authors use  $\alpha = 0.8$  and estimate 3–36 FRBs per day<sup>7</sup>.

We also cross-check our results against published detections from the UTMOST telescope, where Caleb et al. (2017) report three FRBs from a 180-day survey. Our prediction for UTMOST over that time period is slightly higher ( $5 \pm 1$  detections) but does not account for the fact that a fraction of the UTMOST survey was conducted at reduced sensitivity (Caleb et al., 2017). Our forecasted rates for the other surveys are very promising and highlight the impact that these surveys will have on future constraints of the all-sky FRB rate.

### 3.5.4 Source Count Index

Our update of the FRB event rate favors a shallower slope  $\alpha = 0.84$  compared to the expectation from a population of standard candles uniformly distributed in Euclidean space for which  $\alpha = 1.5$ . These lines are shown in the  $\log N$ – $\log S$  plane in Fig. 3.7 and are clearly inconsistent with one another. Although detailed analyses of FRB source counts can be found elsewhere (see, e.g., Macquart & Ekers, 2017, 2018; James et al., 2018), to show what can be learned from future discoveries, it is instructive to place our result in context of two different cosmological models. These are also shown in Fig. 3.7 and were computed using a simple Monte Carlo simulation in which FRBs were drawn from a population uniformly distributed in comoving volume (green line in the figure) and from a redshift distribution that follows the cosmic star formation history (see, Eq. 15 of Madau & Dickinson, 2014). From the corresponding redshift distributions, luminosity distances were computed for each Monte Carlo sample. In both these cases, the luminosities were assumed to be log-normal in form with a standard deviation (in log space) that is 2% of the mean. The mean luminosity was set somewhat arbitrarily for the purpose of these simulations to be  $10^{26}$  W. Our choice of mean luminosity is justified because the estimated mean luminosity from five localised FRBs is  $10^{27 \pm 2}$  W (for redshifts see, Table 1 of Li &

---

<sup>7</sup>Corrected for 200 deg<sup>2</sup> FOV instead of 134 deg<sup>2</sup>.

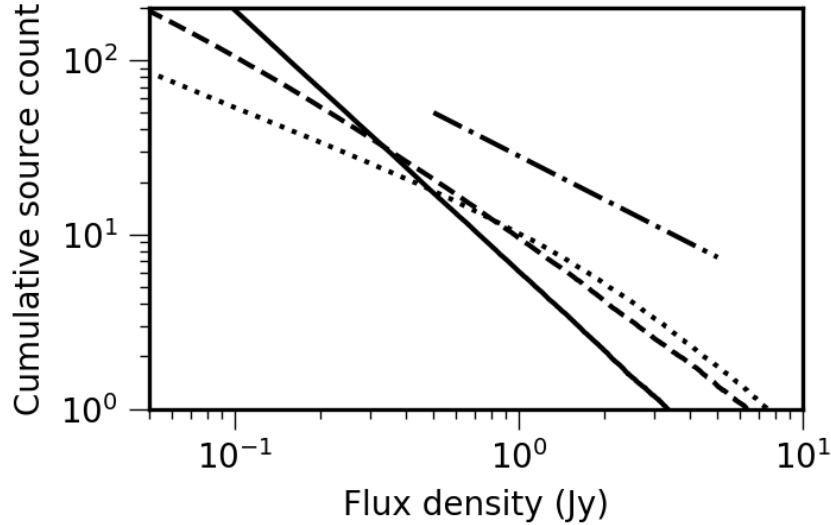


Figure 3.7: Model FRB source counts under the assumptions of: uniform distribution of standard candles in Euclidean space (solid line); a log-normal luminosity distribution uniformly distributed in comoving volume (dotted line); a log-normal luminosity function with redshift distribution following the cosmic star formation rate (Eq. 15 of Madau & Dickinson, 2014, dashed line). The isolated dash-dotted line shows the slope obtained from our analysis ( $\alpha = 0.84$ ) for comparison.

Zhang, 2020). Flux densities were then computed which resulted in the corresponding cumulative curves.

These models were chosen merely to demonstrate that the impact of these assumptions is to naturally flatten the slope of the source count function from the Euclidean value to something that more closely resembles what is observed. Also shown in these simulations is a steepening of the slopes at higher flux density values. Our analysis in section 5.2 does not account for a possible change in  $\alpha$  across the  $\log N$ - $\log S$  plane. In their analysis of Parkes and ASKAP detections, where they considered fluence rather than flux density, James et al. (2018) also found a steepening of the slope at higher fluence values which they suggested could be due to a change in the redshift distribution of the sources. Further analyses of the source count function are definitely required and likely to result in significant insights, particularly from CHIME where a sample of  $\sim 700$  FRBs are eagerly anticipated (Fonseca et al., 2020).

## 3.6 Conclusions

This chapter presented the design, deployment, and initial results from a real-time commensal FRB search pipeline at the GBT named GREENBURST . We also derived new a new FRB rate and source count index based on our null results and 25 other surveys using a sample of 48 FRBs. Using the updated rates and source count index, we forecasted the expected yields of current and upcoming surveys. In future, more detailed analyses that become possible as these surveys are carried out will yield further insights.

## Chapter 4

### A Fast Radio Burst in the Direction of the Virgo Cluster

#### 4.1 Introduction

While on-going blind large-area surveys are providing valuable insights into the population (Shannon et al., 2018; James et al., 2018; James, 2019), targeted searches can also prove fruitful. Recently, in one such attempt to optimise searches Fialkov et al. (2018) predict a possible enhancement in the FRB rate in the direction of nearby galaxy clusters if the intrinsically faint FRB population is abundant. Their study was motivated by the availability of small ( $\sim 20$  m class) radio telescopes which often have large amounts of observing time available with a modest ( $\sim 1$  deg<sup>2</sup>) field of view, but it can also be investigated by facilities with broader sky coverage. Motivated by these predictions, and the great success of the Australian Square Kilometre Array Pathfinder (ASKAP; Schinckel et al., 2012) in finding FRBs (Bannister et al., 2017; Shannon et al., 2018), we have conducted a 300 hr survey with ASKAP to look for such an excess in the direction of the Virgo galaxy cluster.

The search was successful in that we found one new FRB 180417  $\sim 3^\circ$  away from the cluster center. In this chapter, we describe the survey observations and the properties of this new FRB in section 4.2. We also summarise the follow-up observations for repeat bursts in section 4.3. In section 4.4, we comment on its possible location behind the Virgo cluster. We also employ the non-detection of the FRB from the Virgo cluster to derive constraints on the slope and the minimum luminosity cut-off of the FRB luminosity function at the faint-end.

---

Published as Agarwal et al. (2019)

**Contributing authors:** Duncan R. Lorimer, Anastasia Fialkov, Keith W. Bannister, Ryan M. Shannon, Wael Farah, Shivani Bhandari, Jean-Pierre Macquart, Chris Flynn, Giuliano Pignata, Nicolas Tejos, Benjamin Gregg, Stefan Osłowski, Kaustubh Rajwade, Mitchell B. Mickaliger, Benjamin W. Stappers, Di Li, Weiwei Zhu, Lei Qian, Youling Yue, Pei Wang, Abraham Loeb.

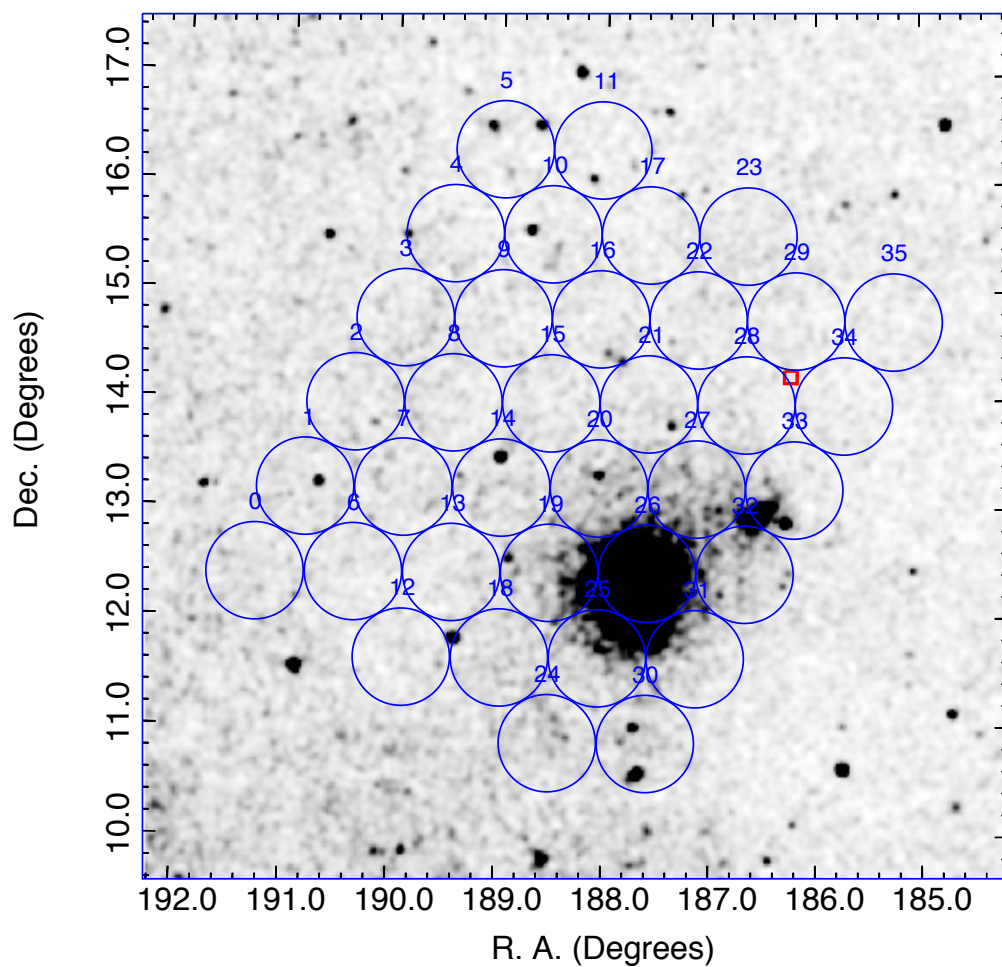


Figure 4.1: The ASKAP footprint overlaid on the ROSAT All-Sky grey scale image of the Virgo cluster of galaxies. The red box denotes the location of FRB 180417. The dark region near Beam 26 is dominated by M87, a giant elliptical galaxy the center of the Virgo cluster.



## 4.2 Observations

The observations were carried out using the commissioning array under the Commensal Real-Time ASKAP Fast-Transients (CRAFT) survey (Macquart et al., 2010). Depending on availability we used 6–8 ASKAP antennas in the incoherent summed mode. The observations were carried out from March 9, 2018, to May 9, 2018, with approximately seven hours per day. The field center is right ascension (RA) 12h33m and declination (Dec) +13d34m in the J2000 epoch. These coordinates were reported by Fialkov et al. (2018) for the maximum FRB rates from Virgo. Fig. 4.1 shows the ASKAP footprint overlaid on a ROSAT image of the cluster (Truemper, 1982). The data capturing pipeline is detailed in Bannister et al. (2017). Total intensity streams from 36 beams of each antenna were recorded on the disk and summed offline. The data were then searched for FRBs using the identical pipeline as described in Bannister et al. (2017). We use the graphics processing unit accelerated real-time search pipeline FREDDA (Bannister et al., 2019) and search for 12 different pulse widths in the range 1.26–15.12 ms over a dispersion measure (DM) interval of 20–4096  $\text{cm}^{-3}$  pc. Candidates were clustered together using the friends of friends of algorithm (Huchra & Geller, 1982) and archived along with their maximum signal to noise ratio (S/N). Clustered candidates with  $S/N > 10$  were selected for subsequent visual inspection.

## 4.3 Results

One FRB was detected as a result of these observations and data processing, FRB 180417. We detail the parameters of this source and the follow-up observations we carried out in the subsections below.

### 4.3.1 FRB 180417

FRB 180417 was strongly detected in three beams with  $S/N > 14$ , and in a further two beams with ( $S/N > 5$ ), as shown in Table 4.1.

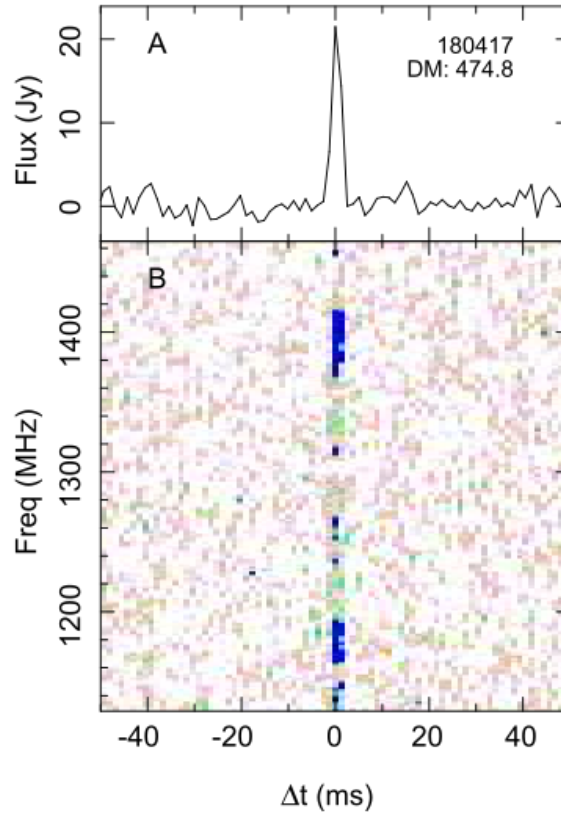


Figure 4.2: The dedispersed profile and dynamic spectrum for FRB 180417. The top panel shows the co-added profile from all three beams. The bottom panel shows the dynamic spectrum of the FRB. The frequency structure of the FRB is clumpy which is similar to previously reported FRBs from ASKAP (Macquart et al., 2019).

Table 4.1: Detection S/N of FRB 180417

Beam	RA (J2000)	DEC (J2000)	S/N
21	12:30:20	13:58:07	0.6
22	12:28:28	14:44:48	5.4
27	12:28 30	13:11:15	3.0
28	12:26:38	13:57:52	15.0
29	12:24:45	14:44:25	16.8
33	12:24:48	13:10:44	5.9
34	12:22:55	13:57:24	14.0

Table 4.2: Observed properties of FRB 180417

Parameter	Value
UTC	2018-04-17 13:18:31 (at 1297 MHz)
MJD	58225.55452546
S/N	24.2
DM	474.8 pc cm <sup>-3</sup>
RA (J2000)	12h 24m 56(28)s
Dec (J2000)	+14d 13(7)m
Boxcar Width	2.52 ms
Fluence	55(3) Jy ms

Fig. 4.2 shows the frequency versus time plot with  $S/N = 24.2$  from the co-addition of these beams. The pulse was detectable at  $S/N \sim 5$  in individual antennas with similar frequency structure.

The estimated Galactic DM contribution in the direction of the FRB using NE2001 (Cordes & Lazio, 2002, 2003) and YMW16 (Yao et al., 2017) is  $26.15 \text{ pc cm}^{-3}$  and  $20.39 \text{ pc cm}^{-3}$  respectively. We estimate the Galactic halo DM contribution to be  $\approx 30 \text{ pc cm}^{-3}$  (see Dolag et al. (2015) and section § 4.4.1 for more discussion). Properties of the FRB are summarised in Table 4.2. The multiple-beam detections of FRB 180417 allow us to constrain the burst location and fluence. To do so, we use the method described in detail in § 4.1 of Bannister et al. (2017) which we summarise here. Using a model for the responses for adjacent beams, we use the beam positions on the sky and burst  $S/N$  to infer the burst position and attenuation. The position and attenuation are inferred using Bayesian methodology, after accounting for uncertainties in beam gain, shape and position. The method has been found to be robust in bursts with the position derived for FRB 180924 using this method consistent with

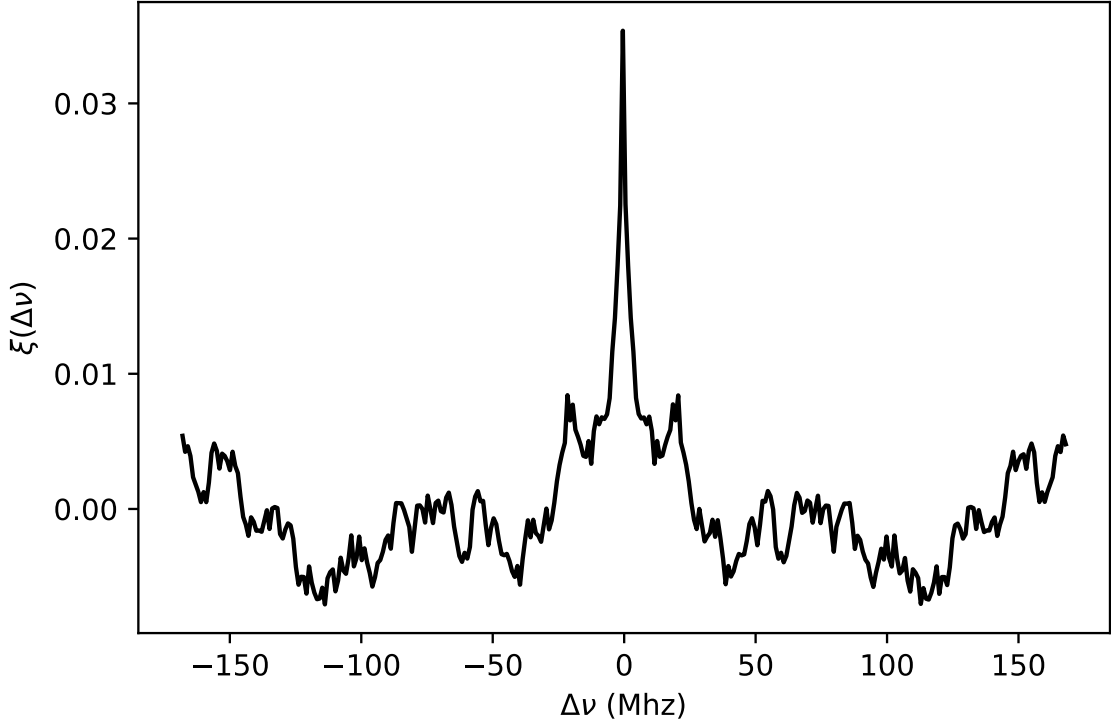


Figure 4.3: The auto-correlation function of the spectrum of FRB180417.

the interferometric position (Bannister et al., 2019), and with the detection of repeat pulses of ASKAP FRB 171019 with the Green Bank telescope (Kumar et al., 2019). Using the positions and S/N for the beams around the FRB 180417 detection (see Table 4.1), we are able to constrain the location to an error box of size  $7' \times 7'$  and the fluence as  $55 \pm 3$  Jy ms.

We characterise the spectral variations by computing the mean normalised auto-correlation function of the spectrum ( $f_\nu$ ) as

$$\xi(\Delta\nu) = \frac{\langle [f_\nu(\nu' + \Delta\nu) - \bar{f}_\nu][f_\nu(\nu') - \bar{f}_\nu] \rangle}{\bar{f}_\nu^2}. \quad (4.1)$$

Here  $\bar{f}_\nu$  is the mean spectrum amplitude. Figure 4.3 shows the auto-correlation function of the FRB spectra. We fit the above with  $\xi(\Delta\nu) = m/(f_{\text{dc}}^2 + \Delta\nu^2)$  and obtain a decorrelation bandwidth,  $f_{\text{dc}} = 4.3 \pm 0.4$  MHz and the modulation index,  $m = 0.47 \pm 0.07$  (Cordes, 1986). This is consistent with expectation for the ISM at

this location on the sky based on the NE2001 model. The NE2001 model estimates  $f_{\text{dc,NE2001}} = 6.3$  MHz at 1.4 GHz, implying the ISM is responsible for the spectral variations.

### 4.3.2 Radio Follow-up Observations

We have undertaken an extensive follow-up campaign to search for repetition from FRB 180417. Owing to the nature of our survey, we have repeatedly covered the region of FRB 180417. The FRB was discovered when 53% of our 300 hr survey was completed. We have spent a total of 27.1 hours searching at the location of the burst with other telescopes as detailed below.

Starting soon after the detection, we began following up using various other telescopes. The most rapid follow-up occurred with the Parkes and Lovell radio telescopes which were able to perform a search for repeated bursts within 24 hours of the original detection, with the The Five-hundred-meter Aperture Spherical radio Telescope (FAST) and a 20-m dish at the Green Bank Observatory joining soon after. The advantage of the follow-up using larger telescopes is the increased sensitivity which is beneficial as we expect there would be weaker bursts, in line with the observed properties of FRB 121102. Under our follow-up, FAST was the most sensitive telescope with 0.03 Jy ms fluence limit (Nan et al., 2011; Li et al., 2018). The data were searched for DM range or  $400\text{--}550$  pc  $\text{cm}^{-3}$  with 1000 trials using HEIMDALL<sup>1</sup>. Candidates with  $S/N > 6$  were inspected visually. Table 4.3 describes the follow-up details. We did not detect any repeat bursts, and we defer detailed limits and modelling to a separate publication.

### 4.3.3 Optical Follow-up

Optical imaging at the location of the FRB 180417 (red cross in Fig. 4.4) was carried out on 2018 May 11.96 UT with the 40 cm PROMPT5 telescope located at CTIO. PROMPT5 has a field of view of  $11' \times 11'$  fully covering the position uncertainty

---

<sup>1</sup><https://sourceforge.net/projects/heimdall-astro>

Table 4.3: Details of the radio follow-up of FRB 180417. Here  $F_{\min}$  is the minimum fluence detectable by the telescope.

Telescope	Observation Length (hr)	$F_{\min}$ (Jy ms)
GB 20m	16.0	4.8
FAST	0.5	0.03
Parkes	6.6	2.0
Lovell	4.0	0.5

derived by the ASKAP observations (green box in Fig. 4.4). A series of thirty 40 s  $R$ -band images were acquired for a total integration time of 20 min. Each frame was corrected for bias, dark and flat using standard routines in IRAF. A final image was obtained taking a median value for each pixel. The photometry was calibrated using the magnitude of stars present in the PROMPT field of view, reported in the Pan-STARRS photometric catalog (Magnier et al., 2016) transformed to the Johnson Kron-Cousins photometric system using the transformation reported in Smith et al. (2002).

To search for an optical counterpart FRB 180417, we searched optical archives looking for images obtained before the FRB occurrence. In the Canada France Hawaii Telescope (CFHT) archive we found an  $r$  band MegaCam image with a total integration time of 1374 s acquired on 2013 May 14th, which fully covered the PROMPT5 image. We aligned, re-scaled and convolved the MegaCam image with SWarp (Bertin et al., 2002) and HOTPANTS (Becker, 2015) in order to match the orientation, flux and PSF of the PROMPT5 frame.

In the template subtracted image, we searched for transients using algorithms developed for the CHASE survey (Pignata et al., 2009). We did not detect any source with  $S/N > 3$ . Using artificial stars placed around the FRB 180417 position, we set an upper limit of  $R = 20.1$  on the optical counterpart detection. The small blank regions in the MegaCam mosaic are covered by one of the sub-frames of a  $R$  band VMOS image acquired on 2009 February 26th, we found in the ESO archive, which has an integration time of 180 s. We use the latter image as a template in the same way we did for the MegaCam frame, however, no sources with  $S/N > 3$  were detected.

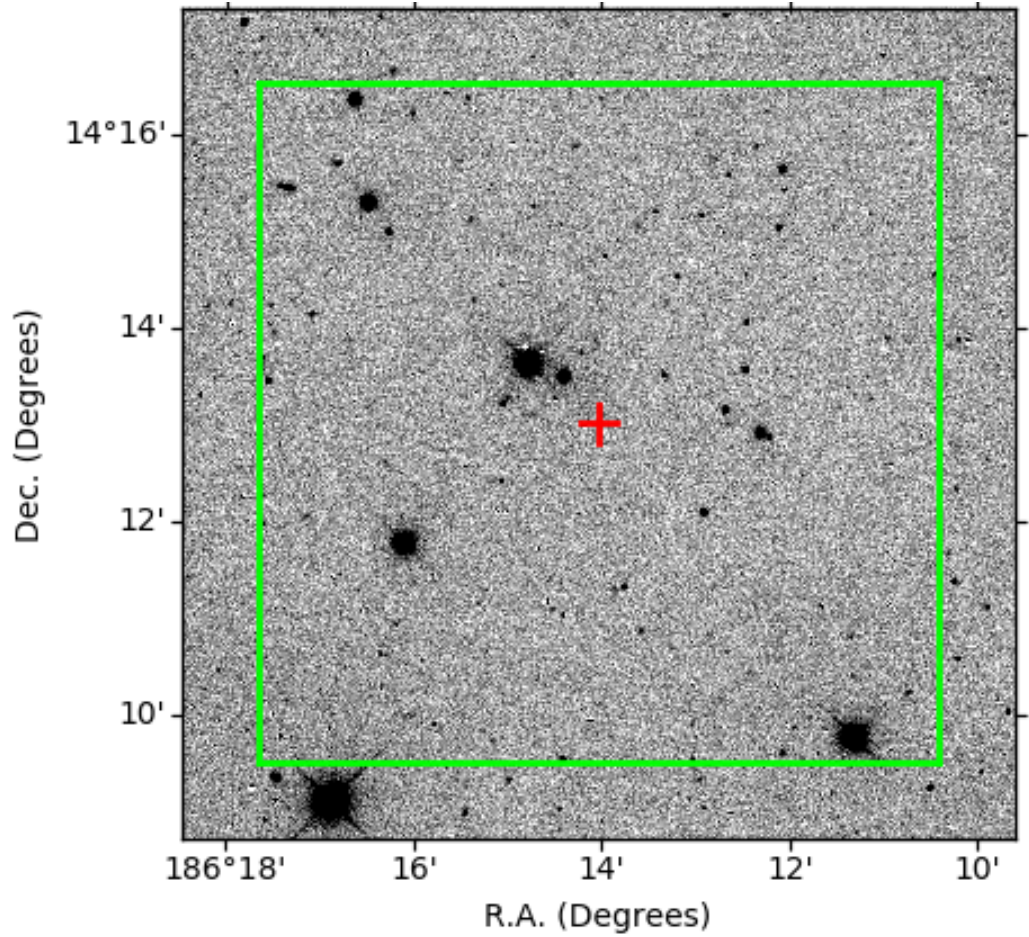


Figure 4.4: PROMPT5 image acquired on 2018 May 11.96 UT. The red cross indicates the FRB 180417 position, while the green square shows the corresponding error box.

## 4.4 Implications of FRB 180417

### 4.4.1 Is FRB 180417 in the Virgo cluster?

To estimate the distance of the FRB we perform a simple analysis in which the DM of FRB 180417,  $DM_{\text{FRB}}$ , is represented as the sum of contributions from the Milky Way (MW), intracluster medium (ICM), intergalactic medium (IGM), and the host, as follows:

$$DM_{\text{FRB}} = DM_{\text{MW}} + DM_{\text{ICM}} + DM_{\text{IGM}} + DM_{\text{host}}. \quad (4.2)$$

Using two different Galactic electron density models NE2001 (Cordes & Lazio, 2002; Yao et al., 2017) for this line of sight, and taking a Galactic halo contribution of  $30 \text{ cm}^{-3} \text{ pc}$ , we find  $DM_{\text{MW}} = 60 \text{ cm}^{-3} \text{ pc}$ . Virgo is at a redshift of  $\approx 0.004$ , and the contribution to the DM due the IGM is expected to be  $\approx 5 \text{ cm}^{-3} \text{ pc}$  (using DM redshift relation from Inoue, 2004), and is considered to be negligible. We model  $DM_{\text{ICM}}$  from the Virgo cluster as described below. Lastly, we leave the host galaxy contribution,  $DM_{\text{host}}$  as a free parameter.

Planck Collaboration et al. (2016) have used X-ray and Planck data to estimate the electron density ( $n_e$ ) out to two virial radii (2.4 Mpc) as a function of the radius. Using this model, the electron density is,

$$n_e(b, z_{\text{LOS}}) = \frac{8.5 \times 10^{-5}}{(b^2 + z_{\text{LOS}}^2)^{0.6}} \text{ cm}^{-3}. \quad (4.3)$$

Here,  $z_{\text{LOS}}$  is the depth along the line of sight (not to be confused with the redshift) and  $b$  is the impact parameter, both in Mpc.  $z_{\text{LOS}} = 0, b = 0$  corresponds to M87, the center of the cluster. FRB 180417 is located  $2.3^\circ$  from the center of the cluster which corresponds to  $b \sim 0.67 \text{ Mpc}$  corresponding to 0.55 times the virial radius. As



a result, the intracluster contribution is

$$\begin{aligned} \text{DM}_{\text{ICM}} &= 10^6 \text{ cm}^{-3} \text{ pc} \int_{-2.4}^{2.4} n_e(b = 0.67, z_{\text{LOS}}) dz_{\text{LOS}} \\ &= 332 \text{ cm}^{-3} \text{ pc}. \end{aligned} \quad (4.4)$$

If FRB 180417 is indeed in the Virgo cluster, then we can place a lower bound on the  $\text{DM}_{\text{host}}$  to be  $90 \text{ cm}^{-3} \text{ pc}$ .

The location of FRB 180417 is at the outskirts of Virgo, where galaxy crowding is low. According to the Virgo catalog (Binggeli et al., 1985; Kim et al., 2014), the closest galaxy, EVCC 0548 is a dwarf spiral (dS0) galaxy,  $6.3'$  away on the sky from the line of sight to FRB 180417 and has half-light radius of  $7.5''$ . The next nearest galaxy is EVCC 0567 which has dwarf elliptical morphology, is  $12'$  away from the FRB location and has half-light radius of  $24''$ . For both of the galaxies, there are no counterparts in the NVSS catalog. Hence, it is difficult to associate the FRB with a member galaxy of Virgo.

#### 4.4.2 Probing the Virgo Intra-cluster Medium

Assuming that the FRB occurred behind the Virgo cluster, we can probe the intracluster (ICM) medium by placing constraints on scatter broadening of the pulse profile. Turbulence in the ICM would cause the radio pulse to diffract, which, if sufficiently strong would cause the pulse to temporally smear. In the case of this observation, we assume that the pulse is emitted at a distance much further than the Virgo cluster, so that we can assume the signal has a plane parallel geometry at the Virgo cluster. Following Eq. 9 from Cordes & Lazio (2002), the pulse scattering time at the distance of the Virgo Cluster (16.5 Mpc) is,

$$\tau = 5.8 \text{ SM}^{6/5} \nu^{-22/5} \text{ s}. \quad (4.5)$$

Here SM is the scattering measure in its conventional units of  $\text{kpc m}^{-20/3}$ , and  $\nu$  is the frequency in GHz. As the pulse width is only two bins, we assume the scatter

broadening to be less than a sample i.e. 1.26 ms. Assuming pulse scattering to be less than one sample, i.e.  $\tau < 1.26$  ms, we find  $\text{SM} < 10^{-3.06} \text{ kpc m}^{-20/3}$ , which can be expressed in terms of the root mean square of the electron column along the line of sight at the outer scale of the turbulence,  $L_0$  of

$$\langle \Delta \text{DM}^2 \rangle^{1/2} = 1.95 \left( \frac{L_0}{1 \text{ pc}} \right)^{5/6} \text{ pc cm}^{-3}. \quad (4.6)$$

This limit is not strongly constraining on the scattering properties of the medium.

To place this in context, one may crudely approximate the intra-cluster medium as a uniform slab of material extending out to twice the virial radius of 1.2 Mpc. This implies a limit on the in situ “level of turbulence” of  $C_N^2 < 3.7 \times 10^{-7} \text{ m}^{-20/3}$  (noting that the scattering measure is the integral of the level of turbulence along the ray path:  $\text{SM} = \int C_N^2(z) dz$ ). One might plausibly expect the value of  $C_N^2$  to be considerably lower than the limit found here for the typical plasma densities and turbulence parameters within an intra-cluster environment. To illustrate this point, consider a medium of mean electron density  $\bar{N}_e$  which gives rise to density fluctuations with variance  $\langle \Delta n_e^2 \rangle = \alpha^2 \bar{N}_e^2$ , at some outer scale  $L_0$ , plausibly of order  $\sim 1$  kpc for the ICM. This would have a characteristic level of turbulence of

$$C_N^2 \approx 6.7 \times 10^{-9} \alpha \left( \frac{\bar{N}_e}{10^{-3} \text{ cm}^{-3}} \right)^2 \left( \frac{L_0}{1 \text{ kpc}} \right)^{-2/3} \text{ m}^{-20/3}, \quad (4.7)$$

where  $\alpha$  is likely of order unity (Anantharamaiah, 1988) and we have normalised to fiducial values for an intra-cluster environment. Thus we observe that the present upper limit on the scattering measure, and in turn  $C_N^2$ , is still a factor  $\sim 50$  above that which might be expected in intra-cluster plasma.

#### 4.4.3 The FRB Luminosity Function

Due to the small number statistics of FRBs, their luminosity function is poorly constrained. Recently, Luo et al. (2018) used 33 FRBs from the online FRB catalog to constrain parameters of the FRB luminosity function assuming the Schechter form

so that the differential number of FRBs per unit luminosity interval is

$$\frac{dN_{\text{FRB}}}{dL_\nu} \propto \left(\frac{L_\nu}{L_{\nu*}}\right)^{-\alpha} \exp\left[-\frac{L_\nu}{L_{\nu*}}\right], \quad L > L_{\text{min}}, \quad (4.8)$$

where  $\alpha$  is the faint-end slope and  $\nu L_{\nu*}$  is the characteristic luminosity of FRBs. The luminosity function is normalised to unity between the minimum intrinsic luminosity  $L_{\text{min}}$  and the maximal brightness (which we assume to be  $10L_{\nu*}$ ) and plays the role of the probability density of FRB luminosities. Luo et al. (2018) found the slope ranging between 1.2 to 1.8 with the best-fit values of  $\alpha \sim 1.5$  and  $L_* \sim 2 \times 10^{44}$  erg s $^{-1}$ . From the sample, it was impossible to measure  $L_{\text{min}}$  due to the limited number of sources. In addition, random FRB searches typically probe mean cosmological population and pick up intrinsically brighter FRBs located at intermediate cosmological distances. For example, the 20 new FRBs recently reported by Shannon et al. (2018) were detected using ASKAP in the fly’s eye mode and are probing the bright-end of the luminosity function. The survey reported here is unique in that, by surveying the nearby clustered environment of Virgo located only  $\sim 16.5$  Mpc away, ASKAP can detect faint FRBs down to  $L \sim 1.3 \times 10^{39}$  erg s $^{-1}$  which corresponds to its flux limit  $S_{\text{lim,ASKAP}} = 26/\sqrt{7}$  Jy. The factor of  $\sqrt{7}$  is due to incoherent sum of data from (on an average) 7 antennas.

The expected FRB number counts from Virgo depend on the shape of the luminosity function, cosmic FRB event rate (used for normalisation), the nature of the progenitors and the spectral energy distribution of the bursts. In Fialkov et al. (2018) we considered two types of the luminosity function for FRBs: (i) standard candles with fixed luminosity of  $\nu L_{\nu*} = 2.8 \times 10^{43}$  erg s $^{-1}$  which corresponds to the mean intrinsic luminosity of the observed FRBs (excluding the recently discovered ASKAP events); and (ii) the Schechter luminosity function. Fialkov et al. showed that if FRBs are standard candles, the contribution of the supercluster is negligible compared to the cosmological contribution within the solid angle of Virgo. However, owing to its proximity, Virgo is expected to dominate the FRB number counts in cases where the faint-end population is numerous (e.g., in the case of a Schechter

luminosity function with sufficiently low  $L_{\min}$  and steep faint-end slope). Assuming that FRB 180417 is outside Virgo, no other FRBs were found in the observed area during the 300 hr survey. Using this information, we can provide new limits on the intrinsically faint population of FRBs constraining  $L_{\min}$  for the first time.

The procedure is as follows: First, we follow the method outlined in Fialkov et al. (2018) to calculate per-galaxy FRB event rate based on a cosmological population of FRBs as a function of  $\alpha$  and  $L_{\min}$  and assuming a fixed total rate of  $\dot{N}_{\text{FRB}} = 10^3$  FRBs per sky per day above the detection threshold of 1 Jy out to redshift  $z = 1$  (e.g., Nicholl et al., 2017). Next, we apply this rate to Virgo galaxies extracted from an online Virgo catalogue (Kim et al., 2014) and calculate the expected number of FRBs within the 300 h survey with ASKAP,  $\langle N_{\text{FRB}}^{\text{Virgo}} \rangle$ . Finally, we employ Poisson statistics to assess the probability of non-detection of FRBs from Virgo and place limits on  $\alpha$  and  $L_{\min}$ .

The cosmic event rate is given by

$$\dot{N}_{\text{FRB}} = \int_V dV \int_{M_h} dM_h \frac{d}{dM_h} n(z, M_h) \frac{\dot{N}_1(z, M_h)}{(1+z)} \int_{S > S_{\min}} dL \left( \frac{L_\nu}{L_{\nu*}} \right)^{-\alpha} \exp \left[ -\frac{L_\nu}{L_{\nu*}} \right] \quad (4.9)$$

where the comoving halo abundance per unit volume ( $dn(z, M_h)/dM_h$ ) is calculated using Sheth-Tormen mass function (Sheth & Tormen, 1999), the  $(1+z)$  factor accounts for cosmological time dilation and  $\dot{N}_1(z, M_h)$  is the FRB rate per halo.  $S_{\min}$  is the larger of the telescope sensitivity and the observed flux of the dimmest intrinsic FRB from redshift  $z$ , given by  $L_{\min}(1+z)/[4\pi D_L^2(z)]$ , and  $D_L(z)$  is the luminosity distance to the FRB. As in Fialkov et al. (2018), we use two models for the FRB progenitors to relate the per-halo rates to the properties of actual galaxies. In the first case, we assume that FRBs trace star formation rate (SFR) and the FRB rate is given by:

$$\dot{N}_1(z, M_h) = R_{\text{SFR}}^{\text{int}} \left( \frac{\text{SFR}(z, M_h)}{\text{SFR}_{\text{Virgo}}} \right), \quad (4.10)$$

where  $R_{\text{SFR}}^{\text{int}}$  is the normalisation coefficient fixed to yield a total of  $\dot{N}_{\text{FRB}} = 10^3$  FRBs per sky per day above the detection threshold of 1 Jy out to redshift  $z = 1$ ,  $\text{SFR}(z, M_h)$

is the cosmic mean star formation rate in halos of mass  $M_h$  at redshift  $z$  calculated using the method of Behroozi et al. (2013) and  $\text{SFR}_{\text{Virgo}} = 776 \text{ M}_{\odot} \text{ yr}^{-1}$  is an estimate of the total SFR in Virgo (estimated following Fialkov et al., 2018). In the second scenario, the FRB rate is proportional to the stellar mass  $M_*$ :

$$\dot{N}_1(z, M_h) = R_{M_*}^{\text{int}} M_*(z, M_h) / M_{\text{Virgo}}, \quad (4.11)$$

where  $R_{M_*}^{\text{int}}$  is the normalisation coefficient,  $M_{\text{Virgo}}$  is the total stellar mass in Virgo  $M_{\text{Virgo}} \sim 6 \times 10^{12} \text{ M}_{\odot}$ , and  $M_*(z, M_h)$  is the total stellar mass in a halo of mass  $M_h$  at redshift  $z$ .  $M_*$  and  $M_h$  are related via the star formation efficiency which we also adopt from the work by Behroozi et al. (2013). Next, we identify Virgo galaxies within the observed field (as specified in Fig. 4.1) using the online Virgo catalogue (Kim et al., 2014). Following Fialkov et al. (2018), for each Virgo galaxy we calculate stellar mass using standard mass-luminosity relations (Bernardi et al., 2010) with luminosities extracted from the catalogue, and the SFR is calculated using the SFR– $M_*$  relation (e.g., Brinchmann et al., 2004). Including all the galaxies located within the field of view, we estimate the total expected number of FRBs from Virgo,  $\langle N_{\text{FRB}}^{\text{Virgo}} \rangle_{\alpha, L_{\text{min}} | \dot{N}_{\text{FRB}}}$ , for a fixed value of  $\dot{N}_{\text{FRB}}$  and as a function of  $L_{\text{min}}$  and  $\alpha$  using the pre-calculated normalisation coefficients,  $R_{\text{SFR}}^{\text{int}}$  and  $R_{M_*}^{\text{int}}$ . As discussed above, it is likely that the detected FRB is behind Virgo as none of the galaxies from the Virgo cluster is located close to the line of sight. We estimate the probability to detect zero FRBs from Virgo,  $P_0(\alpha, L_{\text{min}} | \dot{N}_{\text{FRB}})$ , as a function of the model parameters using Poisson statistics with the expectation value of  $\langle N_{\text{FRB}}^{\text{Virgo}} \rangle_{\alpha, L_{\text{min}} | \dot{N}_{\text{FRB}}}$ . Because of the high number counts of faint FRBs in the cases with steep luminosity functions and low values of  $L_{\text{min}}$ , the probability for non-detection is low in these cases. Such scenarios are ruled out by the data presented in this chapter. On the other hand, in the cases with shallow luminosity function and high values of  $L_{\text{min}}$  the population is intrinsically bright. As a result, number counts from Virgo are low compared to the yield from the cosmological volume within the field of view. In such cases, it is more likely to find an FRB originating behind Virgo than within the cluster and

$P_0(\alpha, L_{\min} | \dot{N}_{\text{FRB}})$  is high.

Marginalising over one of the parameters we compute one-dimensional PDFs for the other parameter. Following the indication from Luo et al. (2018) we assume uniform prior on  $\alpha$  within 1.2–1.8 and a uniform distribution in  $\log_{10} L_{\min}$  over the range  $[10^{-6} - 10^{-2}]L_*$ . For  $10^3$  FRBs per sky per day with flux  $> 1$  Jy and at  $z \leq 1$  we find  $\alpha \leq 1.58$  and  $L_{\min} > 4.1 \times 10^{-5}L_* = 6.5 \times 10^{39} \text{ erg s}^{-1}$  (both at 68% C.L.).

## 4.5 Conclusions

In this chapter, we presented 300 hours of targeted observations towards the core of the Virgo cluster. This led to the discovery of FRB 180417, which is argued to be behind the cluster. As the FRB traverses through the Virgo cluster, we use the pulse profile to put constraints on the intercluster medium’s turbulence. The FRB was promptly followed up in optical wavelengths using the PROMPT5 telescope, but no emission was discovered above an S/N of 3. The burst was also followed up for  $\sim 27$  hours with Parkes, FAST, and Lovell Telescopes, but no repeat bursts were detected. We placed constraints on the minimum luminosity and the FRB luminosity function’s faint end slope using our results.

## Chapter 5

### Conclusions

Here we summarize the work presented in the preceding chapters and provide some updates since this work was carried out. We also give a perspective on future directions that will lead to further progress in our understanding.

#### 5.1 FETCH

In chapter 2, we presented 11 deep learning models to classify FRB and RFI candidates. Using the transfer learning technique, we trained state-of-the-art models on frequency-time and DM-time images individually. These models were then combined using multiplicative fusion to improve performance. We used L-Band data from the GBT and 20 m telescope at the GBO to train our models. All models perform with accuracy and recall  $>99.5\%$  on our test dataset. These models are frequency and telescope agnostic, and the majority of them detected all the FRBs from ASKAP and Parkes telescope and FRB 121102 pulses above an S/N of 8. We also show that the models can be fine-tuned to a specific backend by re-training them with  $\sim 1000$  labeled examples to improve their performance.

We provide a python based open source package FETCH for the classification of candidates using our models. The average classification time of our models is  $12 \pm 1$  ms per candidate on NVIDIA GTX-1070Ti. Therefore using FETCH our models can be promptly deployed at any commensal FRB search backends and can be used to send real-time triggers for multi-frequency follow up. Presently, FETCH is deployed at GREENBURST at the Green Bank Telescope, REALFAST at the Very Large Array (Law et al., 2015) and the Lovell Telescope for commensal searches. It has aided in the discovery of FRB 190614 (Law et al., 2020) and over 100 bursts from several repeaters (Scholz et al., 2020; Kumar et al., 2020; Kirsten et al., 2020; Pearlman et al., 2020; Majid et al., 2020; Aggarwal et al., 2020; Rajwade et al.,

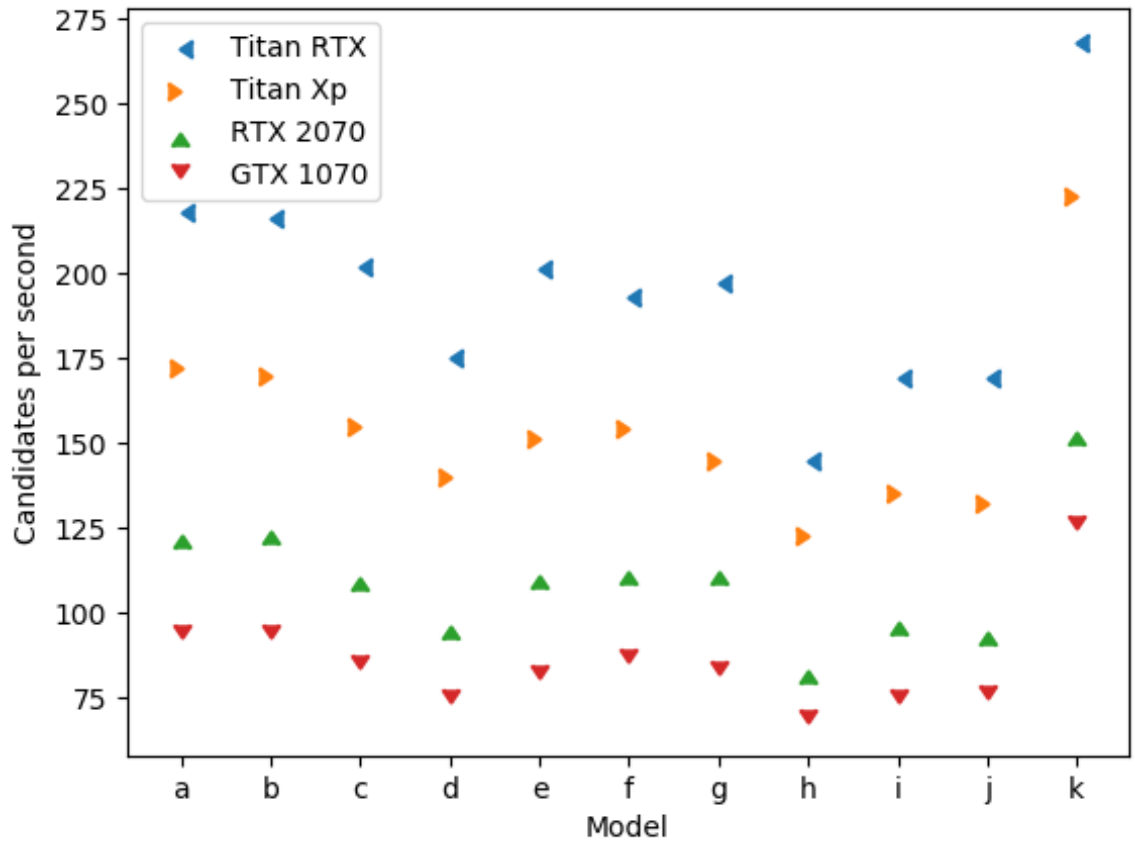


Figure 5.1: Number of candidates classified per second for various GPUs. Blue triangles represent evaluation times on NVIDIA Titan-RTX, Orange represents Titan-Xp, Green represent RTX-2070 and Red represents GTX-1070. Labels A through K correspond to the models defined in Table 2.4



2020; Kumar et al., 2019). Since the initial release, we also optimized the inference performance and can be seen in Figure 5.1.

To date, FETCH remains the state-of-the-art classifier for FRBs and RFI. However, we envision advances in deep learning like transformers (Vaswani et al., 2017) soon will find their FRB astronomy applications as end-to-end machine learning-based FRB search pipelines. Transformers are neural networks based on the attention mechanism. The attention mechanism looks at an input vector and decides at each step in which other parts of the vector are essential and make decisions based on that. For FRB searches, we predict that the transformers will take in the filterbank style data and learn to tag an astrophysical transient’s dispersion curve and distinguish it from the RFI.

## 5.2 GREENBURST

In chapter 3, we present results from the first 157 days of commensal FRB searches at the GBT. We use a GPU accelerated single-pulse search pipeline and classify candidates using a deep learning-based algorithm. Our pipeline searches and classifies candidates in real-time and logs the relevant telescope metadata using several databases. We detected over 2000 single pulses from 20 pulsars during our observations, which helped validate our pipeline. We also carried out blind injection analysis of the data and found that we could categorically detect all FRBs with S/N greater than 12.

Our null result is in line with the FRB rate estimates by Lawrence et al. (2017). We update their analysis and report a rate of  $1150_{-180}^{+200}$  day<sup>-1</sup>sky<sup>-1</sup> and a shallow source count index of  $0.84 \pm 0.06$  above a peak flux of 1 Jy. We estimate that a further year of observations is required to result in GREENBURST FRB detections. Our revised FRB rate shows that emerging and ongoing experiments have excellent prospects to discover a huge sample of FRBs in the coming years. Through a Monte Carlo simulation, we show that studies of FRBs’ source counts using this sample will provide significant insights into the luminosity and redshift distributions of FRBs.

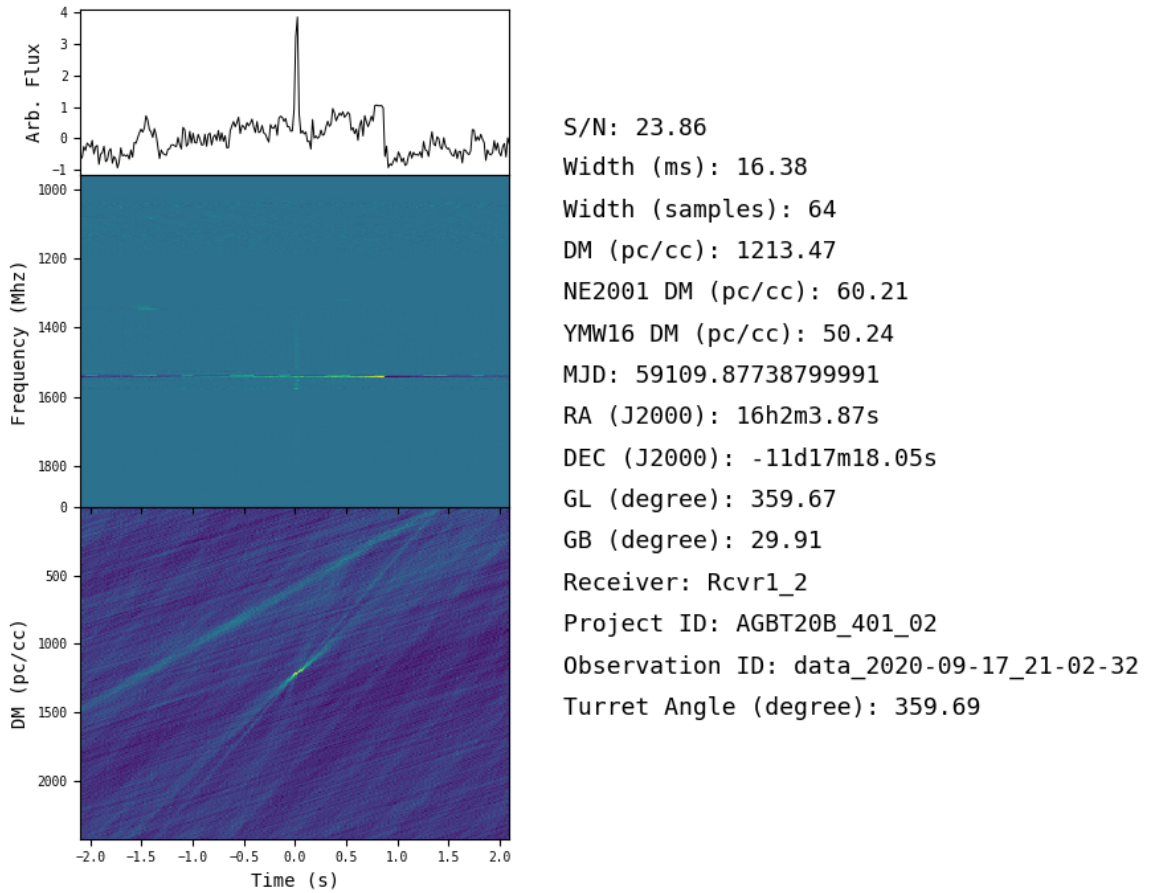
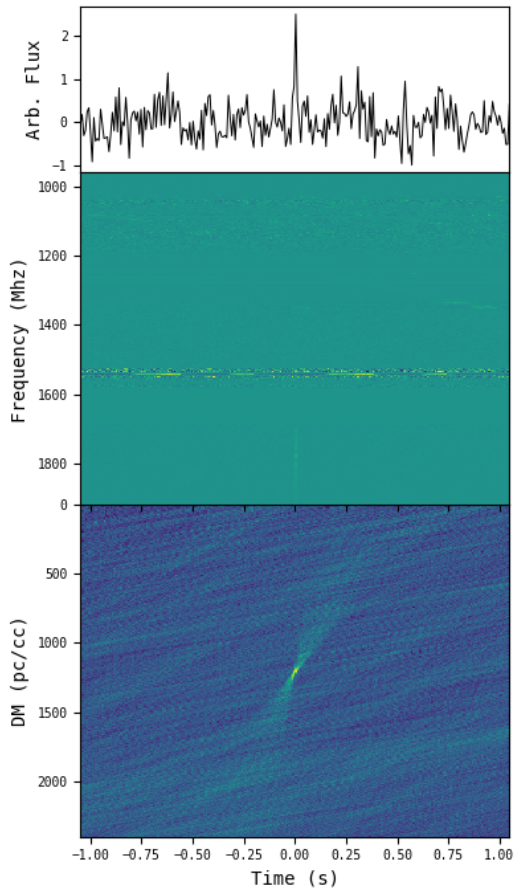


Figure 5.2: GREENBURST detection of a burst from the repeating FRB 190520D. The top plot shows the dedispersed frequency integrated profile; the middle plot shows the dedispersed dynamic spectrum, and the bottom plot shows the DM–time bow-tie shape. The right side of the plots contains various observing metadata.



S/N: 13.54  
 Width (ms): 8.19  
 Width (samples): 32  
 DM (pc/cc): 1200.46  
 NE2001 DM (pc/cc): 60.21  
 YMW16 DM (pc/cc): 50.24  
 MJD: 59109.985935053155  
 RA (J2000): 16h2m3.95s  
 DEC (J2000): -11d17m14.81s  
 GL (degree): 359.67  
 GB (degree): 29.91  
 Receiver: Rcvr1\_2  
 Project ID: AGBT20B\_401\_02  
 Observation ID: data\_2020-09-17\_23-33-32  
 Turret Angle (degree): 359.69

Figure 5.3: Detection of the second burst from the repeater FRB 190520D using GREENBURST during the same observation.

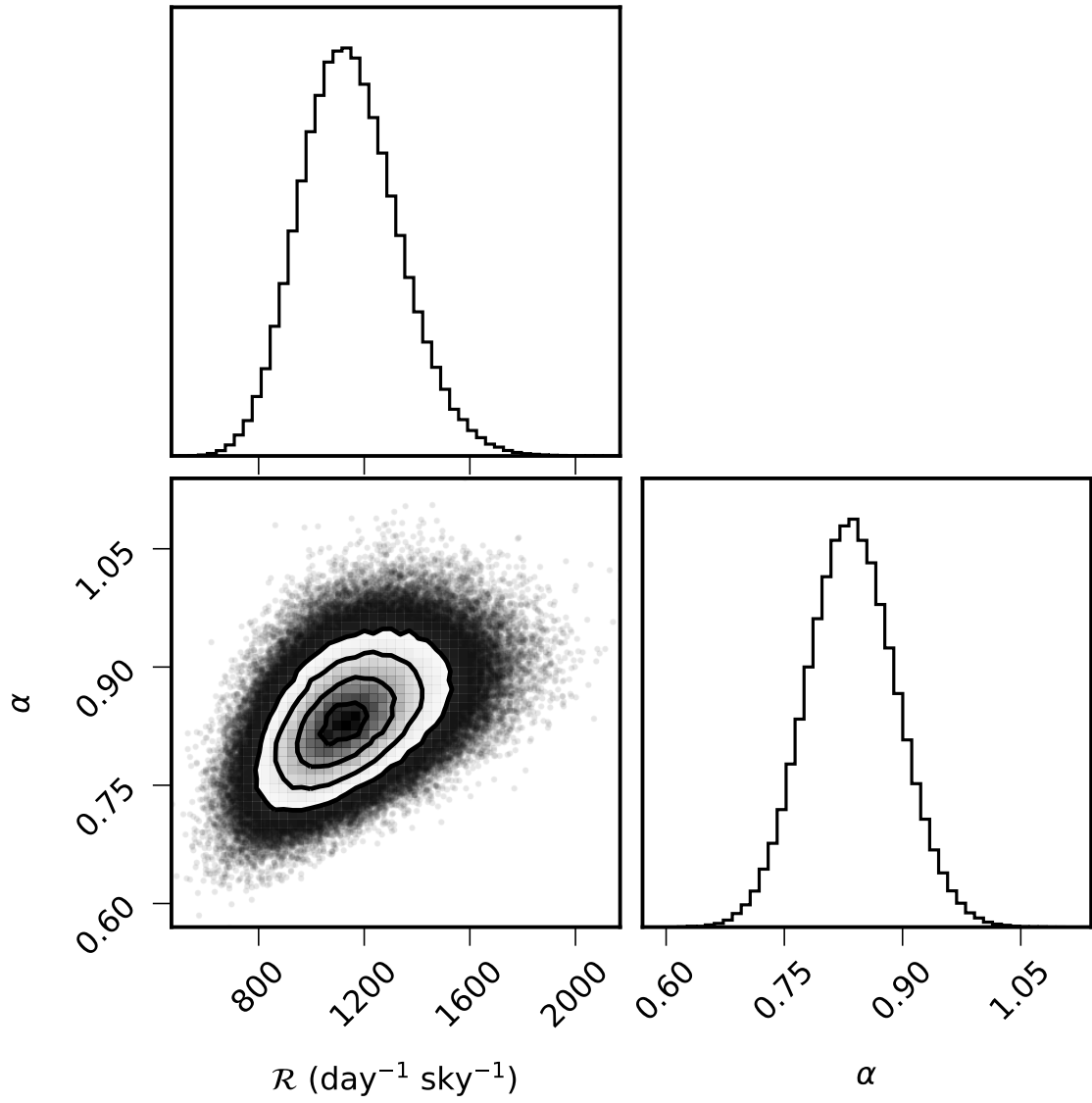


Figure 5.4: Joint and marginalized probability density functions for the updated FRB rate,  $\mathcal{R}$ , and source count index,  $\alpha$ .

Since the publication of the material presented in chapter 3 (Agarwal et al., 2020b), we have observed for 276 days in total. During our observations we detected two bursts from FRB 190520D as shown in Figure 5.2 and Figure 5.3. We revise the FRB rates and source count index using the framework described in subsection 3.5.2 for 276 days. We do not include the bursts detected from FRB 190520D, as it was a targeted observation. Our null results now yield a rate of,

$$\mathcal{R} = 1140_{-180}^{+200} \left( \frac{S}{\text{Jy}} \right)^{-0.84 \pm 0.06} \text{day}^{-1} \text{sky}^{-1}. \quad (5.1)$$

The joint and marginalized probability density functions for the updated FRB rate,  $\mathcal{R}$ , and source count index,  $\alpha$  can be seen in Figure 5.4. Our newer rate, when compare to Lawrence et al. (2017) (as mentioned in chapter 1) shows higher intrinsic FRB rate and a shallower source count index.

### 5.3 A Fast Radio Burst in the Direction of Virgo

In chapter 4, we presented the discovery and follow-up observations of FRB 180417 from a targeted search of the Virgo cluster using the Australian Square Kilometre Array Pathfinder (ASKAP). The search was motivated by the discussion by Fialkov et al. (2018), of possible enhancement in FRB rates in the direction of rich galaxy clusters. The FRB was followed up for 27 hours with four more sensitive telescopes at L-Band. No repeat bursts were detected from the target location. We also followed up the FRB in the optical band using the PROMPT5 telescope, but no sources were discovered.

We argue that FRB 180417 is likely behind the Virgo cluster as the Galactic and intracluster DM contribution was less than the DM of the FRB. Assuming FRB 180417 is beyond Virgo, we constrain intrinsically faint FRBs for the first time, ruling out scenarios with a steep faint-end slope of the luminosity function and extremely low values of the minimum intrinsic FRB luminosity. For the total of  $\dot{N}_{\text{FRB}} = 10^3$  FRBs per sky per day above a threshold of 1 Jy and out to a redshift of 1, consistent with the rate constraints from GREENBURST described above, the minimum luminosity

has to be higher than  $6.5 \times 10^{39} \text{ erg s}^{-1}$  for  $\dot{N}_{\text{FRB}} = 10^3$  FRBs per sky per day. The luminosity function has to be relatively shallow, with a slope of 1.58 or lower for the same FRB rate.

Our unique limits on the faint-end population of FRBs are enabled solely by combining the target cluster search and the large field of view and sensitivity of ASKAP. Blind searches with less sensitive instruments such as the Canadian Hydrogen Intensity Mapping Experiment (CHIME) (The CHIME/FRB Collaboration et al., 2019a,b), even though revealing a significant number of new FRBs, are detecting only very bright events. In such searches, the faint-end population remains unconstrained. Further FRB surveys of galaxy clusters with high-sensitivity instruments will shed more light on FRBs’ minimum intrinsic luminosity.

## 5.4 Looking Ahead

In terms of FRB searches, with newer algorithms, future pipelines include better algorithms like FDMT (Zackay & Ofek, 2017) and better implementations of the brute force dedispersion like *astroaccelerate* (Adamek & Armour, 2019). We are at a stage when we can dedisperse data over 1 GHz of bandwidth (with 4096 channels) 10–50× better than real-time on GPUs. Such advances will allow for much more sensitive searches, including searching for FRBs in subbands and searching over spectral indices. Combined with state-of-the-art deep learning models like *FETCH*, which can classify 100s of candidates per second, they will perform the next generation FRB searches for prompt discoveries.

In terms of FRB astronomy, we presently have a little fewer than 150 FRBs with large variations in pulse shapes and width, frequency-time structure, DM and RM values, and lastly, host galaxy associations. To answer questions like the intrinsic FRB population’s rate and source count index, we need to sample both the very faint end and the bright end of the luminosity distribution. Discoveries from surveys with the FAST telescope and ASKAP will test both ends of the distribution. Fonseca et al. (2020) hinted towards the release of a 700 FRB catalog. Combined results from these

three telescopes should help us paint a clearer picture of the FRB population.

So far, it appears that FRBs come in two flavors, one-off events, and repeaters. The question of whether all FRBs repeat or if indeed there are two populations remains open. However, as mentioned above, the 700 FRB CHIME catalog will undoubtedly help us understand what fraction of observed FRBs are repeaters.

While the origins of FRBs remain a mystery, the recent detection of MJy burst from SGR 1935+2154 and bursts spanning several orders of magnitude is a game-changer. It provides the first direct evidence towards magnetars emitting FRB-like highly energetic bursts favoring the FRB engines' magnetar-based models (Margalit et al., 2020).

We have seen a broad range of frequency–time structures in FRB dynamic spectra. The bursts tend to be either narrowband, broadband, patchy, or any combination of the above. Some repeaters bursts tend to show the sub-burst drift known as the sad trombone effect. While these morphologies are puzzling in nature, a crucial step towards understanding these would be observations from wideband systems at high time resolution. As have already been shown by several multi-wavelength observations of various repeaters, a wealth of information can be extracted with wide-frequency coverage (Gajjar et al., 2018; Kumar et al., 2020; Chawla et al., 2020; Caleb et al., 2020) and high time resolution (Farah et al., 2018; Cho et al., 2020; Day et al., 2020). With upcoming broadband systems at all 100 m class telescopes worldwide, we anticipate deeper insights towards the burst structure and hints towards physical mechanisms leading to such emission.

We are entering the era of discovering localized FRB where several telescopes like ASKAP and VLA are detecting and localizing FRBs. Upcoming telescopes like MeerKat (Camilo et al., 2018) and CHIME outriggers (Amiri et al., 2018) will soon join, revealing a sample of FRBs with known redshifts helping us probe the IGM better. While we already have the Macquart relation, a more extensive selection of localized FRBs will help us constrain the scatter in the relation (Macquart, 2018; Macquart et al., 2020). FRB astronomy's future is exceptionally bright, especially with the upcoming surveys from influential new instruments combined with powerful

search techniques that will substantially progress over the next decade.



## Bibliography

- 2016, 2016 IEEE Conference on Computer Vision and Pattern Recognition, CVPR 2016, Las Vegas, NV, USA, June 27-30, 2016 (IEEE Computer Society). <http://ieeexplore.ieee.org/xpl/mostRecentIssue.jsp?punumber=7776647>
- Abadi, M., Agarwal, A., Barham, P., et al. 2015, TensorFlow: Large-Scale Machine Learning on Heterogeneous Systems, , , software available from tensorflow.org. <https://www.tensorflow.org/>
- Ackermann, S., Schawinski, K., Zhang, C., Weigel, A. K., & Turp, M. D. 2018, MNRAS, 479, 415
- Adamek, K., & Armour, W. 2019, Single Pulse Detection Algorithms for Real-time Fast Radio Burst Searches using GPUs, , , arXiv:1910.08324
- Agarwal, D., Aggarwal, K., Burke-Spolaor, S., Lorimer, D. R., & Garver-Daniels, N. 2020a, Monthly Notices of the Royal Astronomical Society, 497, 1661. <https://doi.org/10.1093/mnras/staa1856>
- Agarwal, D., Lorimer, D. R., Fialkov, A., et al. 2019, Monthly Notices of the Royal Astronomical Society, 490, 1. <https://doi.org/10.1093/mnras/stz2574>
- Agarwal, D., Lorimer, D. R., Surnis, M. P., et al. 2020b, Monthly Notices of the Royal Astronomical Society, 497, 352. <https://doi.org/10.1093/mnras/staa1927>
- Aggarwal, K., Law, C. J., Burke-Spolaor, S., et al. 2020, Research Notes of the AAS, 4, 94. <https://doi.org/10.3847/2515-5172/ab9f33>
- Amiri, M., Bandura, K., Berger, P., et al. 2018, The Astrophysical Journal, 863, 48. <https://doi.org/10.3847/1538-4357/aad188>
- Amiri, M., Bandura, K., Bhardwaj, M., et al. 2019, Nature, doi:10.1038/s41586-018-0867-7. <https://doi.org/10.1038/s41586-018-0867-7>
- Anantharamaiah, K. R. 1988, in AIP Conference Proceedings (AIP). <https://doi.org/10.1063/1.37590>

- Aniyan, A. K., & Thorat, K. 2017, *The Astrophysical Journal Supplement Series*, 230, 20
- Bannister, K., Zackay, B., Qiu, H., James, C., & Shannon, R. 2019, FREDDA: A fast, real-time engine for de-dispersing amplitudes, , , ascl:1906.003
- Bannister, K. W., Shannon, R. M., Macquart, J.-P., et al. 2017, *The Astrophysical Journal*, 841, L12. <https://doi.org/10.3847/2041-8213/aa71ff>
- Bannister, K. W., Deller, A. T., Phillips, C., et al. 2019, *Science*, 365, 565. <https://doi.org/10.1126/science.aaw5903>
- Barsdell, B. R. 2012, PhD thesis, Swinburne University of Technology
- Barsdell, B. R., Bailes, M., Barnes, D. G., & Fluke, C. J. 2012, *Monthly Notices of the Royal Astronomical Society*, 422, 379. <https://doi.org/10.1111/j.1365-2966.2012.20622.x>
- Becker, A. 2015, HOTPANTS: High Order Transform of PSF ANd Template Subtraction, *Astrophysics Source Code Library*, , , ascl:1504.004
- Behroozi, P. S., Wechsler, R. H., & Conroy, C. 2013, *ApJ*, 770, 57
- Beloborodov, A. M. 2017, *The Astrophysical Journal*, 843, L26. <https://doi.org/10.3847/2041-8213/aa78f3>
- Bernardi, M., Shankar, F., Hyde, J. B., et al. 2010, *MNRAS*, 404, 2087
- Bertin, E., Mellier, Y., Radovich, M., et al. 2002, in *Astronomical Society of the Pacific Conference Series*, Vol. 281, *Astronomical Data Analysis Software and Systems XI*, ed. D. A. Bohlender, D. Durand, & T. H. Handley, 228
- Bethapudi, S., & Desai, S. 2018, *Astronomy and Computing*, 23, 15
- Bhandari, S., Bannister, K. W., James, C. W., et al. 2019, *Monthly Notices of the Royal Astronomical Society*, 486, 70. <https://doi.org/10.1093/mnras/stz804>

- Bhandari, S., Keane, E. F., Barr, E. D., et al. 2017, Monthly Notices of the Royal Astronomical Society, 475, 1427. <https://doi.org/10.1093/mnras/stx3074>
- Bhandari, S., Sadler, E. M., Prochaska, J. X., et al. 2020, The Astrophysical Journal, 895, L37. <https://doi.org/10.3847/2041-8213/ab672e>
- Bhat, N. D. R., Cordes, J. M., Camilo, F., Nice, D. J., & Lorimer, D. R. 2004, The Astrophysical Journal, 605, 759. <https://doi.org/10.1086/382680>
- Binggeli, B., Sandage, A., & Tammann, G. A. 1985, The Astronomical Journal, 90, 1681. <https://doi.org/10.1086/113874>
- Bishop, C. M. 2006, Pattern Recognition and Machine Learning (Information Science and Statistics) (Berlin, Heidelberg: Springer-Verlag)
- Bochenek, C. D., Ravi, V., Belov, K. V., et al. 2020, A fast radio burst associated with a Galactic magnetar, , , arXiv:2005.10828
- Breiman, L. 2001, Mach. Learn., 45, 5. <https://doi.org/10.1023/A:1010933404324>
- Brinchmann, J., Charlot, S., White, S. D. M., et al. 2004, MNRAS, 351, 1151
- Buda, M., Maki, A., & Mazurowski, M. A. 2018, Neural Networks, 106, 249. <https://doi.org/10.1016/j.neunet.2018.07.011>
- Burke-Spolaor, S., Bailes, M., Johnston, S., et al. 2011, Monthly Notices of the Royal Astronomical Society, 416, 2465. <https://doi.org/10.1111/j.1365-2966.2011.18521.x>
- Burns, W. R., & Clark, B. G. 1969, A&A, 2, 280
- Burrows, D. N. 2014, The WSPC Handbook of Astronomical Instrumentation (WORLD SCIENTIFIC), doi:10.1142/9446. <https://doi.org/10.1142/9446>
- Caleb, M., Flynn, C., Bailes, M., et al. 2017, Monthly Notices of the Royal Astronomical Society, 468, 3746. <https://doi.org/10.1093/mnras/stx638>

- Caleb, M., Stappers, B. W., Abbott, T. D., et al. 2020, Monthly Notices of the Royal Astronomical Society, 496, 4565. <https://doi.org/10.1093/mnras/staa1791>
- Camilo, F., Ransom, S. M., Halpern, J. P., et al. 2006, Nature, 442, 892. <https://doi.org/10.1038/nature04986>
- Camilo, F., Scholz, P., Serylak, M., et al. 2018, The Astrophysical Journal, 856, 180. <https://doi.org/10.3847/1538-4357/aab35a>
- Champion, D. J., Petroff, E., Kramer, M., et al. 2016, Monthly Notices of the Royal Astronomical Society: Letters, 460, L30. <https://doi.org/10.1093/mnrasl/slw069>
- Chapin, N. 1970, ACM Computing Surveys (CSUR), 2, 119. <https://doi.org/10.1145/356566.356570>
- Chatterjee, S., Law, C. J., Wharton, R. S., et al. 2017, Nature, 541, 58. <https://doi.org/10.1038/nature20797>
- Chawla, P., Kaspi, V. M., Josephy, A., et al. 2017, The Astrophysical Journal, 844, 140. <https://doi.org/10.3847/1538-4357/aa7d57>
- Chawla, P., Andersen, B. C., Bhardwaj, M., et al. 2020, The Astrophysical Journal, 896, L41. <https://doi.org/10.3847/2041-8213/ab96bf>
- Chennamangalam, J., Karastergiou, A., MacMahon, D., et al. 2017a, in The Fourteenth Marcel Grossmann Meeting (WORLD SCIENTIFIC). [https://doi.org/10.1142/9789813226609\\_0359](https://doi.org/10.1142/9789813226609_0359)
- Chennamangalam, J., MacMahon, D., Cobb, J., et al. 2017b, The Astrophysical Journal Supplement Series, 228, 21. <https://doi.org/10.3847/1538-4365/228/2/21>
- Cho, H., Macquart, J.-P., Shannon, R. M., et al. 2020, The Astrophysical Journal, 891, L38. <https://doi.org/10.3847/2041-8213/ab7824>

- Chollet, F. 2016, CoRR, abs/1610.02357, arXiv:1610.02357. <http://arxiv.org/abs/1610.02357>
- Chollet, F., et al. 2015, Keras, <https://keras.io>, ,
- Claesen, M., & Moor, B. D. 2015, Hyperparameter Search in Machine Learning, , , arXiv:1502.02127
- Connor, L., Sievers, J., & Pen, U.-L. 2016, Monthly Notices of the Royal Astronomical Society: Letters, 458, L19. <https://doi.org/10.1093/mnrasl/slv124>
- Connor, L., & van Leeuwen, J. 2018, The Astronomical Journal, 156, 256. <https://doi.org/10.3847/1538-3881/aae649>
- Connor, L., van Leeuwen, J., Oostrum, L. C., et al. 2020, Monthly Notices of the Royal Astronomical Society, 499, 4716. <https://doi.org/10.1093/mnras/staa3009>
- Cordes, J. M. 1978, ApJ, 222, 1006
- Cordes, J. M. 1986, The Astrophysical Journal, 311, 183. <https://doi.org/10.1086/164764>
- Cordes, J. M. 2002, in Astronomical Society of the Pacific Conference Series, Vol. 278, Single-Dish Radio Astronomy: Techniques and Applications, ed. S. Stanimirovic, D. Altschuler, P. Goldsmith, & C. Salter, 227–250
- Cordes, J. M., & Chatterjee, S. 2019, Annual Review of Astronomy and Astrophysics, 57, 417. <https://doi.org/10.1146/annurev-astro-091918-104501>
- Cordes, J. M., & Lazio, T. J. W. 2002, NE2001.I. A New Model for the Galactic Distribution of Free Electrons and its Fluctuations, , , arXiv:astro-ph/0207156
- . 2003, NE2001. II. Using Radio Propagation Data to Construct a Model for the Galactic Distribution of Free Electrons, , , arXiv:astro-ph/0301598
- Cordes, J. M., & Wasserman, I. 2016, Monthly Notices of the Royal Astronomical Society, 457, 232. <https://doi.org/10.1093/mnras/stv2948>

- Dai, Z. G., Wang, J. S., Wu, X. F., & Huang, Y. F. 2016, *The Astrophysical Journal*, 829, 27. <https://doi.org/10.3847/0004-637x/829/1/27>
- Day, C. K., Deller, A. T., Shannon, R. M., et al. 2020, *Monthly Notices of the Royal Astronomical Society*, 497, 3335. <https://doi.org/10.1093/mnras/staa2138>
- Deneva, J. S., Cordes, J. M., McLaughlin, M. A., et al. 2009, *The Astrophysical Journal*, 703, 2259. <https://doi.org/10.1088/0004-637x/703/2/2259>
- Deng, J., Dong, W., Socher, R., et al. 2009, in CVPR09
- Devine, T. R., Goseva-Popstojanova, K., & McLaughlin, M. 2016, *MNRAS*, 459, 1519
- Dolag, K., Gaensler, B. M., Beck, A. M., & Beck, M. C. 2015, *Monthly Notices of the Royal Astronomical Society*, 451, 4277. <http://dx.doi.org/10.1093/mnras/stv1190>
- Eatough, R. P., Keane, E. F., & Lyne, A. G. 2009, *Monthly Notices of the Royal Astronomical Society*, 395, 410. <https://doi.org/10.1111/j.1365-2966.2009.14524.x>
- Egorov, A. E., & Postnov, K. A. 2009, *Astronomy Letters*, 35, 241. <https://doi.org/10.1134/s1063773709040033>
- Falcke, H., & Rezzolla, L. 2014, *Astronomy & Astrophysics*, 562, A137. <https://doi.org/10.1051/0004-6361/201321996>
- Farah, W., Flynn, C., Bailes, M., et al. 2018, *Monthly Notices of the Royal Astronomical Society*, 478, 1209. <https://doi.org/10.1093/mnras/sty1122>
- Fialkov, A., Loeb, A., & Lorimer, D. R. 2018, *The Astrophysical Journal*, 863, 132. <https://doi.org/10.3847/1538-4357/aad196>
- Fonseca, E., Andersen, B. C., Bhardwaj, M., et al. 2020, *The Astrophysical Journal*, 891, L6. <https://doi.org/10.3847/2041-8213/ab7208>
- Foreman-Mackey, D., Hogg, D. W., Lang, D., & Goodman, J. 2013, *PASP*, 125, 306

- Fortmann-Roe, S. 2012, Understanding the Bias-Variance Tradeoff, , . <http://scott.fortmann-roe.com/docs/BiasVariance.html>
- Foster, G., Karastergiou, A., Golpayegani, G., et al. 2017, Monthly Notices of the Royal Astronomical Society, 474, 3847. <https://doi.org/10.1093/mnras/stx3038>
- Gajjar, V., Siemion, A. P. V., Price, D. C., et al. 2018, The Astrophysical Journal, 863, 2. <https://doi.org/10.3847/1538-4357/aad005>
- Geman, S., Bienenstock, E., & Doursat, R. 1992, Neural Computation, 4, 1. <https://doi.org/10.1162/neco.1992.4.1.1>
- Geng, J. J., & Huang, Y. F. 2015, The Astrophysical Journal, 809, 24. <https://doi.org/10.1088/0004-637x/809/1/24>
- Golpayegani, G., Lorimer, D. R., Ellingson, S. W., et al. 2019, Monthly Notices of the Royal Astronomical Society, 489, 4001. <https://doi.org/10.1093/mnras/stz2424>
- Goodfellow, I. J., Bengio, Y., & Courville, A. 2016, Deep Learning (Cambridge, MA, USA: MIT Press), <http://www.deeplearningbook.org>
- Gu, W.-M., Dong, Y.-Z., Liu, T., Ma, R., & Wang, J. 2016, The Astrophysical Journal, 823, L28. <https://doi.org/10.3847/2041-8205/823/2/L28>
- Gu, W.-M., Yi, T., & Liu, T. 2020, Monthly Notices of the Royal Astronomical Society, 497, 1543. <https://doi.org/10.1093/mnras/staa1914>
- Guo, P., Duan, F., Wang, P., Yao, Y., & Xin, X. 2017, ArXiv e-prints, arXiv:1711.10339
- Hankins, T. H., & Eilek, J. A. 2007, The Astrophysical Journal, 670, 693. <https://doi.org/10.1086/522362>
- Hardy, L. K., Dhillon, V. S., Spitler, L. G., et al. 2017, Monthly Notices of the Royal Astronomical Society, 472, 2800. <https://doi.org/10.1093/mnras/stx2153>

- Haslam, C. G. T., Salter, C. J., Stoffel, H., & Wilson, W. E. 1982, *A&AS*, 47, 1
- He, K., Zhang, X., Ren, S., & Sun, J. 2016, in 2016 IEEE Conference on Computer Vision and Pattern Recognition, CVPR 2016, Las Vegas, NV, USA, June 27-30, 2016 (IEEE Computer Society), 770–778. <https://doi.org/10.1109/CVPR.2016.90>
- Hearst, M. A. 1998, *IEEE Intelligent Systems*, 13, 18. <http://dx.doi.org/10.1109/5254.708428>
- Heintz, K. E., Prochaska, J. X., Simha, S., et al. 2020, Host Galaxy Properties and Offset Distributions of Fast Radio Bursts: Implications for their Progenitors, , , arXiv:2009.10747
- Hessels, J. W. T., Spitler, L. G., Seymour, A. D., et al. 2019, *The Astrophysical Journal*, 876, L23. <https://doi.org/10.3847/2041-8213/ab13ae>
- Hewish, A., Bell, S. J., Pilkington, J. D. H., Scott, P. F., & Collins, R. A. 1968, *Nature*, 217, 709. <https://doi.org/10.1038/217709a0>
- Hosmer, L., Langston, G., Heatherly, S., et al. 2013, in American Astronomical Society Meeting Abstracts, Vol. 221, American Astronomical Society Meeting Abstracts #221, 345.24
- Howard, A. G., Zhu, M., Chen, B., et al. 2017, *CoRR*, abs/1704.04861, arXiv:1704.04861. <http://arxiv.org/abs/1704.04861>
- Huang, G., Liu, Z., van der Maaten, L., & Weinberger, K. Q. 2017, in 2017 IEEE Conference on Computer Vision and Pattern Recognition, CVPR 2017, Honolulu, HI, USA, July 21-26, 2017 (IEEE Computer Society), 2261–2269. <https://doi.org/10.1109/CVPR.2017.243>
- Huchra, J. P., & Geller, M. J. 1982, *ApJ*, 257, 423
- Inoue, S. 2004, *MNRAS*, 348, 999



- Iqbal, H. 2018, HarisIqbal88/PlotNeuralNet v1.0.0, Zenodo, doi:10.5281/ZENODO.2526396. <https://zenodo.org/record/2526396>
- James, C. W. 2019, Monthly Notices of the Royal Astronomical Society, 486, 5934. <https://doi.org/10.1093/mnras/stz1224>
- James, C. W., Ekers, R. D., Macquart, J.-P., Bannister, K. W., & Shannon, R. M. 2018, Monthly Notices of the Royal Astronomical Society, 483, 1342. <https://doi.org/10.1093/mnras/sty3031>
- Jessner, A., Popov, M. V., Kondratiev, V. I., et al. 2010, Astronomy & Astrophysics, 524, A60. <https://doi.org/10.1051/0004-6361/201014806>
- Jiang, Y., Zur, R. M., Pesce, L. L., & Drukker, K. 2009, in 2009 International Joint Conference on Neural Networks, 1428–1432
- Johnston, S., & Romani, R. W. 2004, in Young Neutron Stars and Their Environments, ed. F. Camilo & B. M. Gaensler, Vol. 218, 315
- Karastergiou, A., Chennamangalam, J., Armour, W., et al. 2015, MNRAS, 452, 1254
- Kashiyama, K., Ioka, K., & Mészáros, P. 2013, The Astrophysical Journal, 776, L39. <https://doi.org/10.1088/2041-8205/776/2/139>
- Keane, E. F., & Petroff, E. 2015, Monthly Notices of the Royal Astronomical Society, 447, 2852. <https://doi.org/10.1093/mnras/stu2650>
- Keane, E. F., Stappers, B. W., Kramer, M., & Lyne, A. G. 2012, MNRAS, 425, L71
- Keane, E. F., Johnston, S., Bhandari, S., et al. 2016, Nature, 530, 453. <https://doi.org/10.1038/nature17140>
- Keith, M. J., Jameson, A., Straten, W. V., et al. 2010, Monthly Notices of the Royal Astronomical Society, 409, 619. <https://doi.org/10.1111/j.1365-2966.2010.17325.x>
- Khan, A., Huerta, E. A., Wang, S., et al. 2019, Physics Letters B, 795, 248

- Kibble, T. W. B. 1976, *Journal of Physics A: Mathematical and General*, 9, 1387. <https://doi.org/10.1088/0305-4470/9/8/029>
- Kim, S., Rey, S.-C., Jerjen, H., et al. 2014, *The Astrophysical Journal Supplement Series*, 215, 22. <https://doi.org/10.1088/0067-0049/215/2/22>
- Kingma, D. P., & Ba, J. 2015, in 3rd International Conference on Learning Representations, ICLR 2015, San Diego, CA, USA, May 7-9, 2015, Conference Track Proceedings, ed. Y. Bengio & Y. LeCun. <http://arxiv.org/abs/1412.6980>
- Kirsten, F., Snelders, M., Jenkins, M., et al. 2020, arXiv e-prints, arXiv:2007.05101
- Kocz, J., Ravi, V., Catha, M., et al. 2019, *Monthly Notices of the Royal Astronomical Society*, 489, 919. <https://doi.org/10.1093/mnras/stz2219>
- Kumar, P., Lu, W., & Bhattacharya, M. 2017, *Monthly Notices of the Royal Astronomical Society*, 468, 2726. <https://doi.org/10.1093/mnras/stx665>
- Kumar, P., Shannon, R. M., Osłowski, S., et al. 2019, *The Astrophysical Journal*, 887, L30. <https://doi.org/10.3847/2041-8213/ab5b08>
- Kumar, P., Shannon, R. M., Flynn, C., et al. 2020, arXiv e-prints, arXiv:2009.01214
- Law, C. J., Bower, G. C., Burke-Spolaor, S., et al. 2015, *The Astrophysical Journal*, 807, 16. <https://doi.org/10.1088/0004-637x/807/1/16>
- . 2018, *The Astrophysical Journal Supplement Series*, 236, 8. <https://doi.org/10.3847/1538-4365/aab77b>
- Law, C. J., Butler, B. J., Prochaska, J. X., et al. 2020, *The Astrophysical Journal*, 899, 161. <https://doi.org/10.3847/1538-4357/aba4ac>
- Lawrence, E., Wiel, S. V., Law, C., Spolaor, S. B., & Bower, G. C. 2017, *The Astronomical Journal*, 154, 117. <https://doi.org/10.3847/1538-3881/aa844e>
- Li, D., Wang, P., Qian, L., et al. 2018, *IEEE Microwave Magazine*, 19, 112. <https://doi.org/10.1109/mmm.2018.2802178>

- Li, Y., & Zhang, B. 2020, *The Astrophysical Journal*, 899, L6. <https://doi.org/10.3847/2041-8213/aba907>
- Lingam, M., & Loeb, A. 2017, *The Astrophysical Journal*, 837, L23. <https://doi.org/10.3847/2041-8213/aa633e>
- Liu, T., Romero, G. E., Liu, M.-L., & Li, A. 2016, *The Astrophysical Journal*, 826, 82. <https://doi.org/10.3847/0004-637x/826/1/82>
- Locatelli, N. T., Bernardi, G., Bianchi, G., et al. 2020, *The Northern Cross Fast Radio Burst project. I. Overview and pilot observations at 408 MHz*, , , arXiv:2003.04317
- Lorimer, D. R., Bailes, M., McLaughlin, M. A., Narkevic, D. J., & Crawford, F. 2007, *Science*, 318, 777
- Lorimer, D. R., & Kramer, M. 2004, *Handbook of Pulsar Astronomy*, Vol. 4
- Lorimer, D. R., Kramer, M., Müller, P., et al. 2000, *A&A*, 358, 169
- Luan, J., & Goldreich, P. 2014, *The Astrophysical Journal*, 785, L26. <https://doi.org/10.1088/2041-8205/785/2/126>
- Luo, R., Lee, K., Lorimer, D. R., & Zhang, B. 2018, *MNRAS*, 481, 2320
- Luo, R., Wang, B. J., Men, Y. P., et al. 2020, *Nature*, 586, 693. <https://doi.org/10.1038/s41586-020-2827-2>
- Lyubarsky, Y. 2014, *Monthly Notices of the Royal Astronomical Society: Letters*, 442, L9. <https://doi.org/10.1093/mnrasl/slu046>
- Lyutikov, M., Burzawa, L., & Popov, S. B. 2016, *Monthly Notices of the Royal Astronomical Society*, 462, 941. <https://doi.org/10.1093/mnras/stw1669>
- Maan, Y., & van Leeuwen, J. 2017, in *2017 XXXIInd General Assembly and Scientific Symposium of the International Union of Radio Science (URSI GASS) (IEEE)*. <https://doi.org/10.23919/ursigass.2017.8105320>

- Macquart, J.-P. 2018, *Nature Astronomy*, 2, 836. <https://doi.org/10.1038/s41550-018-0625-7>
- Macquart, J.-P., & Ekers, R. 2018, *Monthly Notices of the Royal Astronomical Society*, 480, 4211. <https://doi.org/10.1093/mnras/sty2083>
- Macquart, J.-P., & Ekers, R. D. 2017, *Monthly Notices of the Royal Astronomical Society*, 474, 1900. <https://doi.org/10.1093/mnras/stx2825>
- Macquart, J.-P., Shannon, R. M., Bannister, K. W., et al. 2019, *The Astrophysical Journal*, 872, L19. <https://doi.org/10.3847/2041-8213/ab03d6>
- Macquart, J.-P., Bailes, M., Bhat, N. D. R., et al. 2010, *Publications of the Astronomical Society of Australia*, 27, 272. <https://doi.org/10.1071/as09082>
- Macquart, J.-P., Prochaska, J. X., McQuinn, M., et al. 2020, *Nature*, 581, 391. <https://doi.org/10.1038/s41586-020-2300-2>
- Madau, P., & Dickinson, M. 2014, *Annual Review of Astronomy and Astrophysics*, 52, 415. <https://doi.org/10.1146/annurev-astro-081811-125615>
- Madison, D. R., Agarwal, D., Aggarwal, K., et al. 2019, *The Astrophysical Journal*, 887, 252. <https://doi.org/10.3847/2041-8213/ab58c3>
- Magnier, E. A., Chambers, K. C., Flewelling, H. A., et al. 2016, *The Pan-STARRS Data Processing System*, , , arXiv:1612.05240
- Magro, A., Karastergiou, A., Salvini, S., et al. 2011, *Monthly Notices of the Royal Astronomical Society*, 417, 2642. <https://doi.org/10.1111/j.1365-2966.2011.19426.x>
- Majid, W. A., Pearlman, A. B., Nimmo, K., et al. 2020, *The Astrophysical Journal*, 897, L4. <https://doi.org/10.3847/2041-8213/ab9a4a>
- Manchester, R. N., Hobbs, G. B., Teoh, A., & Hobbs, M. 2005, *The Astronomical Journal*, 129, 1993. <https://doi.org/10.1086/428488>

- Manchester, R. N., Lyne, A. G., Camilo, F., et al. 2001, *MNRAS*, 328, 17
- Marcote, B., Nimmo, K., Hessels, J. W. T., et al. 2020, *Nature*, 577, 190. <https://doi.org/10.1038/s41586-019-1866-z>
- Margalit, B., Beniamini, P., Sridhar, N., & Metzger, B. D. 2020, *The Astrophysical Journal*, 899, L27. <https://doi.org/10.3847/2041-8213/abac57>
- Masui, K., Lin, H.-H., Sievers, J., et al. 2015, *Nature*, 528, 523. <https://doi.org/10.1038/nature15769>
- McFadden, R., Karastergiou, A., & Roberts, S. 2018, in *IAU Symposium, Vol. 337, Pulsar Astrophysics the Next Fifty Years*, ed. P. Weltevrede, B. B. P. Perera, L. L. Preston, & S. Sanidas, 372–373
- McLaughlin, M. A., & Cordes, J. M. 2003, *The Astrophysical Journal*, 596, 982. <https://doi.org/10.1086/378232>
- McLaughlin, M. A., Lyne, A. G., Lorimer, D. R., et al. 2006, *Nature*, 439, 817. <https://doi.org/10.1038/nature04440>
- Men, Y., Aggarwal, K., Li, Y., et al. 2019, *Monthly Notices of the Royal Astronomical Society*, doi:10.1093/mnras/stz2386. <https://doi.org/10.1093/mnras/stz2386>
- Metzger, B. D., Margalit, B., & Sironi, L. 2019, *Monthly Notices of the Royal Astronomical Society*, 485, 4091. <https://doi.org/10.1093/mnras/stz700>
- Michilli, D., Seymour, A., Hessels, J. W. T., et al. 2018, *Nature*, 553, 182. <https://doi.org/10.1038/nature25149>
- Mingarelli, C. M. F., Levin, J., & Lazio, T. J. W. 2015, *The Astrophysical Journal*, 814, L20. <https://doi.org/10.1088/2041-8205/814/2/120>
- Most, E. R., Nathanail, A., & Rezzolla, L. 2018, *The Astrophysical Journal*, 864, 117. <https://doi.org/10.3847/1538-4357/aad6ef>

- Mottez, F., & Zarka, P. 2014, *Astronomy & Astrophysics*, 569, A86. <https://doi.org/10.1051/0004-6361/201424104>
- Nan, R., Li, D., Jin, C., et al. 2011, *International Journal of Modern Physics D*, 20, 989
- Newburgh, L. B., Bandura, K., Bucher, M. A., et al. 2016, in *Ground-based and Airborne Telescopes VI*, ed. H. J. Hall, R. Gilmozzi, & H. K. Marshall (SPIE). <https://doi.org/10.1117/12.2234286>
- Nicholl, M., Williams, P. K. G., Berger, E., et al. 2017, *The Astrophysical Journal*, 843, 84. <https://doi.org/10.3847/1538-4357/aa794d>
- Ośłowski, S., Shannon, R. M., Ravi, V., et al. 2019, *Monthly Notices of the Royal Astronomical Society*, 488, 868. <https://doi.org/10.1093/mnras/stz1751>
- Pang, D., Goseva-Popstojanova, K., Devine, T., & McLaughlin, M. 2018, *Monthly Notices of the Royal Astronomical Society*, 480, 3302. <https://doi.org/10.1093/mnras/sty1992>
- Park, E., Han, X., Berg, T. L., & Berg, A. C. 2016, in *2016 IEEE Winter Conference on Applications of Computer Vision (WACV) (IEEE)*. <https://doi.org/10.1109/wacv.2016.7477589>
- Patel, C., Agarwal, D., Bhardwaj, M., et al. 2018, *The Astrophysical Journal*, 869, 181. <https://doi.org/10.3847/1538-4357/aaee65>
- Pearlman, A. B., Majid, W. A., Prince, T. A., et al. 2020, arXiv e-prints, arXiv:2009.13559
- Pérez-Carrasco, M., Cabrera-Vives, G., Martínez-Marin, M., et al. 2019, *PASP*, 131, 108002
- Petroff, E., Bailes, M., Barr, E. D., et al. 2014, *Monthly Notices of the Royal Astronomical Society*, 447, 246. <https://doi.org/10.1093/mnras/stu2419>

- Petroff, E., Barr, E. D., Jameson, A., et al. 2016, Publications of the Astronomical Society of Australia, 33, doi:10.1017/pasa.2016.35. <https://doi.org/10.1017/pasa.2016.35>
- Petroff, E., Burke-Spolaor, S., Keane, E. F., et al. 2017, Monthly Notices of the Royal Astronomical Society, doi:10.1093/mnras/stx1098. <https://doi.org/10.1093/mnras/stx1098>
- Petroff, E., Oostrum, L. C., Stappers, B. W., et al. 2018, Monthly Notices of the Royal Astronomical Society, doi:10.1093/mnras/sty2909. <https://doi.org/10.1093/mnras/sty2909>
- Pignata, G., Maza, J., Antezana, R., et al. 2009, in Probing Stellar Populations Out To The Distant Universe - Cefalu 2008 - Proceedings of the International Conference, Vol. 1111, 551–554
- Planck Collaboration, Ade, P. A. R., Aghanim, N., et al. 2016, A&A, 596, A101. <https://doi.org/10.1051/0004-6361/201527743>
- Platts, E., Weltman, A., Walters, A., et al. 2019, Physics Reports, 821, 1. <https://doi.org/10.1016/j.physrep.2019.06.003>
- Prestage, R. M., Bloss, M., Brandt, J., et al. 2015, in 2015 USNC-URSI Radio Science Meeting (Joint with AP-S Symposium) (IEEE). <https://doi.org/10.1109/usnc-ursi.2015.7303578>
- Price, D. C., Foster, G., Geyer, M., et al. 2019, Monthly Notices of the Royal Astronomical Society, 486, 3636. <https://doi.org/10.1093/mnras/stz958>
- Qiu, H., Bannister, K. W., Shannon, R. M., et al. 2019, Monthly Notices of the Royal Astronomical Society, 486, 166. <https://doi.org/10.1093/mnras/stz748>
- Qiu, H., Shannon, R. M., Farah, W., et al. 2020, Monthly Notices of the Royal Astronomical Society, 497, 1382. <https://doi.org/10.1093/mnras/staa1916>
- Radhakrishnan, V., & Cooke, D. J. 1969, ApJ letters, 3, 225

- Rajwade, K. M., Agarwal, D., Lorimer, D. R., et al. 2019, Monthly Notices of the Royal Astronomical Society, 489, 1709. <https://doi.org/10.1093/mnras/stz2207>
- Rajwade, K. M., Mickaliger, M. B., Stappers, B. W., et al. 2020, Monthly Notices of the Royal Astronomical Society, 495, 3551. <https://doi.org/10.1093/mnras/staa1237>
- Ravi, V. 2019, Nature Astronomy, 3, 928. <https://doi.org/10.1038/s41550-019-0831-y>
- Ravi, V. 2019, MNRAS, 482, 1966
- Ravi, V., Shannon, R. M., Bailes, M., et al. 2016, Science, 354, 1249. <https://doi.org/10.1126/science.aaf6807>
- Roshi, D. A., Bloss, M., Brandt, P., et al. 2011, in 2011 XXXth URSI General Assembly and Scientific Symposium (IEEE). <https://doi.org/10.1109/ursigass.2011.6051280>
- Sammut, C., & Webb, G. I., eds. 2017, Encyclopedia of Machine Learning and Data Mining (Springer US), doi:10.1007/978-1-4899-7687-1. <https://doi.org/10.1007/978-1-4899-7687-1>
- Sandler, M., Howard, A. G., Zhu, M., Zhmoginov, A., & Chen, L. 2018, in 2018 IEEE Conference on Computer Vision and Pattern Recognition, CVPR 2018, Salt Lake City, UT, USA, June 18-22, 2018 (IEEE Computer Society), 4510–4520. [http://openaccess.thecvf.com/content\\_cvpr\\_2018/html/Sandler\\_MobileNetV2\\_Inverted\\_Residuals\\_CVPR\\_2018\\_paper.html](http://openaccess.thecvf.com/content_cvpr_2018/html/Sandler_MobileNetV2_Inverted_Residuals_CVPR_2018_paper.html)
- Scheuer, P. A. G. 1968, Nature, 218, 920
- Schinckel, A. E., Bunton, J. D., Cornwell, T. J., Feain, I., & Hay, S. G. 2012, in Ground-based and Airborne Telescopes IV, ed. L. M. Stepp, R. Gilmozzi, & H. J. Hall (SPIE). <https://doi.org/10.1117/12.926959>



- Scholz, P., Spitler, L. G., Hessels, J. W. T., et al. 2016, *The Astrophysical Journal*, 833, 177. <https://doi.org/10.3847/1538-4357/833/2/177>
- Scholz, P., Cook, A., Cruces, M., et al. 2020, *The Astrophysical Journal*, 901, 165. <https://doi.org/10.3847/1538-4357/abb1a8>
- Shannon, R. M., Macquart, J.-P., Bannister, K. W., et al. 2018, *Nature*, 562, 386. <https://doi.org/10.1038/s41586-018-0588-y>
- Sheth, R. K., & Tormen, G. 1999, *MNRAS*, 308, 119
- Simonyan, K., & Zisserman, A. 2014, CoRR, abs/1409.1556, arXiv:1409.1556. <http://arxiv.org/abs/1409.1556>
- Smith, A. B., Caton, D. B., & Hawkins, R. L. 2016, *Publications of the Astronomical Society of the Pacific*, 128, 055002. <https://doi.org/10.1088%2F1538-3873%2F128%2F963%2F055002>
- Smith, J. A., Tucker, D. L., Kent, S., et al. 2002, *The Astronomical Journal*, 123, 2121. <https://doi.org/10.1086/339311>
- Spitler, L. G., Cordes, J. M., Hessels, J. W. T., et al. 2014, *The Astrophysical Journal*, 790, 101. <https://doi.org/10.1088/0004-637x/790/2/101>
- Spitler, L. G., Scholz, P., Hessels, J. W. T., et al. 2016, *Nature*, 531, 202. <https://doi.org/10.1038/nature17168>
- Staelin, D. 1969, *Proceedings of the IEEE*, 57, 724. <https://doi.org/10.1109/proc.1969.7051>
- Staelin, D. H., & Reifstein, E. C. 1968, *Science*, 162, 1481. <https://doi.org/10.1126/science.162.3861.1481>
- Surnis, M. P., Agarwal, D., Lorimer, D. R., et al. 2019, *Publications of the Astronomical Society of Australia*, 36, doi:10.1017/pasa.2019.26. <https://doi.org/10.1017/pasa.2019.26>

- Szegedy, C., Ioffe, S., Vanhoucke, V., & Alemi, A. A. 2017, in Proceedings of the Thirty-First AAAI Conference on Artificial Intelligence, February 4-9, 2017, San Francisco, California, USA., ed. S. P. Singh & S. Markovitch (AAAI Press), 4278–4284. <http://aaai.org/ocs/index.php/AAAI/AAAI17/paper/view/14806>
- Szegedy, C., Vanhoucke, V., Ioffe, S., Shlens, J., & Wojna, Z. 2016, in 2016 IEEE Conference on Computer Vision and Pattern Recognition, CVPR 2016, Las Vegas, NV, USA, June 27-30, 2016 (IEEE Computer Society), 2818–2826. <https://doi.org/10.1109/CVPR.2016.308>
- Taylor, J. H. 1974, *A&AS*, 15, 367
- Tendulkar, S. P., Bassa, C. G., Cordes, J. M., et al. 2017, *The Astrophysical Journal*, 834, L7. <https://doi.org/10.3847/2041-8213/834/2/17>
- The CHIME/FRB Collaboration, :, Amiri, M., et al. 2019a, *Nature*, 566, 235. <https://doi.org/10.1038/s41586-018-0864-x>
- The CHIME/FRB Collaboration, Andersen, . B. C., Bandura, K., et al. 2019b, *The Astrophysical Journal*, 885, L24. <https://doi.org/10.3847/2041-8213/ab4a80>
- The CHIME/FRB Collaboration, :, Andersen, B. C., et al. 2020a, A bright millisecond-duration radio burst from a Galactic magnetar, , , arXiv:2005.10324
- The CHIME/FRB Collaboration, Amiri, M., Andersen, B. C., et al. 2020b, *Nature*, 582, 351. <https://doi.org/10.1038/s41586-020-2398-2>
- Thornton, D., Stappers, B., Bailes, M., et al. 2013, *Science*, 341, 53. <https://doi.org/10.1126/science.1236789>
- Truemper, J. 1982, *Advances in Space Research*, 2, 241
- Vachaspati, T. 2008, *Physical Review Letters*, 101, doi:10.1103/physrevlett.101.141301. <https://doi.org/10.1103/physrevlett.101.141301>

- Vanderlinde, K., Bandura, K., Belostotski, L., et al. 2019, LRP 2020 Whitepaper: The Canadian Hydrogen Observatory and Radio-transient Detector (CHORD), , , arXiv:1911.01777
- Vaswani, A., Shazeer, N., Parmar, N., et al. 2017, CoRR, abs/1706.03762, arXiv:1706.03762. <http://arxiv.org/abs/1706.03762>
- Vilalta, R. 2018, arXiv e-prints, arXiv:1812.10403
- Wadiasingh, Z., Beniamini, P., Timokhin, A., et al. 2020, The Astrophysical Journal, 891, 82. <https://doi.org/10.3847/1538-4357/ab6d69>
- Wadiasingh, Z., & Timokhin, A. 2019, The Astrophysical Journal, 879, 4. <https://doi.org/10.3847/1538-4357/ab2240>
- Wang, J.-S., Yang, Y.-P., Wu, X.-F., Dai, Z.-G., & Wang, F.-Y. 2016, The Astrophysical Journal, 822, L7. <https://doi.org/10.3847/2041-8205/822/1/17>
- Wang, W., Luo, R., Yue, H., et al. 2018, The Astrophysical Journal, 852, 140. <https://doi.org/10.3847/1538-4357/aaa025>
- Williams, P. K. G., & Berger, E. 2016, The Astrophysical Journal, 821, L22. <https://doi.org/10.3847/2041-8205/821/2/122>
- Williamson, I. P. 1972, Monthly Notices of the Royal Astronomical Society, 157, 55. <https://doi.org/10.1093/mnras/157.1.55>
- Yamasaki, S., Totani, T., & Kiuchi, K. 2018, Publications of the Astronomical Society of Japan, 70, doi:10.1093/pasj/psy029. <https://doi.org/10.1093/pasj/psy029>
- Yao, J. M., Manchester, R. N., & Wang, N. 2017, The Astrophysical Journal, 835, 29. <https://doi.org/10.3847/1538-4357/835/1/29>
- Ye, J., Wang, K., & Cai, Y.-F. 2017, The European Physical Journal C, 77, doi:10.1140/epjc/s10052-017-5319-2. <https://doi.org/10.1140/epjc/s10052-017-5319-2>

- Zackay, B., & Ofek, E. O. 2017, *The Astrophysical Journal*, 835, 11. <https://doi.org/10.3847/1538-4357/835/1/11>
- Zhang, B. 2016, *The Astrophysical Journal*, 827, L31. <https://doi.org/10.3847/2041-8205/827/2/131>
- Zhang, B. 2017, *The Astrophysical Journal*, 836, L32. <https://doi.org/10.3847/2F2041-8213%2Faa5ded>
- Zhang, S.-B., Hobbs, G., Dai, S., et al. 2019, *Monthly Notices of the Royal Astronomical Society: Letters*, 484, L147. <https://doi.org/10.1093/mnrasl/slz023>
- Zhang, S.-B., Hobbs, G., Russell, C. J., et al. 2020, *The Astrophysical Journal Supplement Series*, 249, 14. <https://doi.org/10.3847/1538-4365/ab95a4>
- Zhang, Y. G., Gajjar, V., Foster, G., et al. 2018, *The Astrophysical Journal*, 866, 149. <https://doi.org/10.3847/1538-4357/aadf31>
- Zhu, W. W., Berndsen, A., Madsen, E. C., et al. 2014, *ApJ*, 781, 117